THz resonances in semiconductor structures

Martijn Cornelis Schaafsma

The cover shows an artist's impression of a terahertz resonance in a semiconductor structure. Design by Ruud Mons and Martijn Schaafsma.

ISBN: 978-90-77209-90-5

Printed by Ipskamp Drukkers, Enschede

The work described in this thesis was performed at the FOM Institute AMOLF, Science Park 104, 1098 XG Amsterdam, The Netherlands.
A digital version of this thesis can be downloaded from http://www.amolf.nl
A catalogue record is available from the Eindhoven University of Technology Library.

THz resonances in semiconductor structures

PROEFSCHRIFT

ter verkrijging van de graad van doctor aan de
Technische Universiteit Eindhoven, op gezag van
de rector magnificus, prof.dr.ir. C.J. van Duijn,
voor een commissie aangewezen door het College
voor Promoties in het openbaar te verdedigen op
maandag 16 maart 2015 om 16.00 uur

door

Martijn Cornelis Schaafsma

geboren te 's-Gravenhage

Dit proefschrift is goedgekeurd door de promotoren en de samenstelling van de promotiecommissie is als volgt:

voorzitter:	prof.dr.ir. G.M.W. Kroesen
1e promotor:	prof.dr. J. Gómez Rivas
2e promotor:	prof.dr. P.M. Koenraad
leden:	prof.dr. L. Kuipers (Universiteit Utrecht)
	prof.dr. P.M. Planken (Universiteit van Amsterdam)
	prof.dr. A.F. Koenderink (Universiteit van Amsterdam)
	dr. M. Matters-Kammerer
	prof.dr.ir. O.J. Luiten

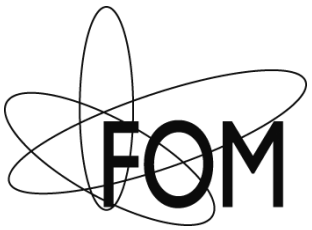

This work is part of the research program of the "Stichting voor Fundamenteel Onderzoek der Materie (FOM)", which is financially supported by the "Nederlandse organisatie voor Wetenschappelijk Onderzoek (NWO)".

Voor mijn ouders en grootouders

Science may be described as the art of systematic oversimplification.
Sir Carl Popper (1982)

Contents

Chapter 1

Introduction

In this doctoral thesis we demonstrate experimentally and discuss theoretically electrically conducting structures that are small compared to the wavelength of light. Under certain conditions the electromagnetic field of light incident on a conducting structure can hybridize with the free electrons, driving the electrons in a resonant oscillation. These conditions change when an ensemble of these scatterers is organized into a periodic lattice. Although the frequency range under consideration in this thesis is that of low optical frequencies, i.e. in the far-infrared, most of the physics applies to the full electromagnetic spectrum. Especially the range of frequencies in the visible and near-infrared. This chapter attempts to place the physics described in this thesis in historic context, and gives an overview of the development of the physics on which this thesis elaborates. A more detailed background on the history of optics can be found in literature[1].

1.1 Optics

Our understanding of the world around us is greatly influenced by how we perceive it, and the level of our understanding often hinges on the quality of the observation. Although light is almost everywhere and vision one of our primary senses, understanding the mechanism behind it required a tremendous effort throughout history. With both the scales of length and time vastly outside the human scale, the fundamentals proved to be a challenge to grasp. As time advanced the crude models became more robust, and more phenomena were understood and explained. The term optics itself originates from the Greek τα οπτικα, which translates as 'sight'. The most simplistic description of light is that of ray-optics. Around the third century BC it was Euclid who used this approach to explain the mechanism of perspective and how to handle

[1] For instance Fitzpatrick [1], Kubbinga [2], or Sengupta [3].

the reflections from mirrors. Simple ray-optics however does not manage to explain the 'bending' of light -refraction- when it passes from one interface to another. A crude version, and not accurate for all but small angles, was described by Ptolemy in the second century AD. He proposed that the angles of incidence and refraction are proportional to a some sort of constant, but did not manage to derive the full equation. It took until the seventeenth century, concurrent with the enlightenment, before the next major leaps forward. The relation that Ptolemy was looking for describes the angle of propagation θ_2 as a function of the angle of incidence angle θ_1 and the refractive indexes n_1 and n_2 of the media according to

$$\frac{\sin\theta_1}{\sin\theta_2} = \frac{n_2}{n_1} \,. \tag{1.1}$$

Although the earliest recordings of this law date back to Ibn Sahl from Baghdad in the late 10th century [4, 5], both Descartes (1596-1650) and Snell (1580-1626) are attributed credit for the sine-law of refraction stated in equation (1.1). It was Piere de Fermat who was able to explain and derive the sine-law in 1658, using the principle that light when propagating from one place to another takes the path of least time. He therefor made the -correct- assumption that light actually slows down when traveling in a dense medium, proportionally to the index of refraction. The principle of Fermat is in agreement with the theory from Huygens, who introduced the wave theory for light around that same time [6].

A corollary from the wave-like nature of light is that it has to propagate with a certain speed. This speed can be very large, but it has to be finite. One of the first successful attempts in estimating the speed of light was made by the Danish astronomer Olaf Römer in 1676 [7]. He witnessed a modulation on his timings of the eclipses of Jupiter's satellites, which he only could explain by a finite time for the light to reach the earth. Based on his data he estimated the speed of light to be 220 000 km/s, which is accurate within 30%. It took until the second half of the 19th century to have this estimate improved. Fizeau used in 1849 a rotating toothed wheel and a mirror at 8 km distance and he arrived at a speed of propagation at 314 858 km/s [8], 5% too large. Foucault replaced the toothed wheel by a rotating mirror and increased the distance to 30 miles, and arrived in 1862 at a speed of light of $298\,000 \pm 500$ km/s [9]. The discovery that light propagates in transverse polarized waves, and not longitudinal as for sound, was made by Fresnel and Young [10]. A corollary of transverse polarized waves is that they account for polarization, and as such allow for the explanation of for instance birefringence. In parallel to the studies of light by Fresnel, Young and others, James Clerc Maxwell was working on the nature of electric and magnetic fields. Building further on the works of Gauss, Ørsted, Ampère and Faraday; Maxwell managed in 1864 to produce a complete set of equations, describing the divergence and rotation of the electric and magnetic fields as functions of the charge and current distributions.

These equations can be summarized as [11]:

$$\nabla \cdot \mathbf{E} = \frac{1}{\epsilon_0}\rho \,, \tag{1.2}$$

$$\nabla \times \mathbf{E} = -\frac{\partial \mathbf{B}}{\partial t} \,, \tag{1.3}$$

$$\nabla \cdot \mathbf{B} = 0 \,, \tag{1.4}$$

$$\nabla \times \mathbf{B} = \mu_0 \mathbf{J} + \mu_0 \epsilon_0 \frac{\partial \mathbf{E}}{\partial t} \,. \tag{1.5}$$

A corollary of these equations, is that when one takes the rotation of equations (1.3) and (1.5) in the absence of any charges and currents, with proper substitution they can be rewritten as

$$\nabla^2 \mathbf{E} = \frac{1}{c^2}\frac{\partial^2 \mathbf{E}}{\partial t^2} \,, \tag{1.6}$$

$$\nabla^2 \mathbf{B} = \frac{1}{c^2}\frac{\partial^2 \mathbf{B}}{\partial t^2} \,. \tag{1.7}$$

These equations can be recognized as the differential forms of the wave-equation, where the waves propagate with a speed of $c = \sqrt{1/\mu_0\epsilon_0}$. The values for both μ_0 and ϵ_0 can be independently acquired, and the speed of propagation which Maxwell calculated based on electromagnetic measurements was $c = 314\,740$ km/s. The close proximity of this result to the speed of light made him realize that "*light and magnetism are affections of the same substance, and that light is an electromagnetic disturbance propagated through the field according to electromagnetic laws*" [12].

It was Hertz who became fascinated by the work of Maxwell, and he designed and carried out an experiment to test the support of Maxwell's theory for electromagnetic waves. He demonstrated in 1887 the wireless transmission of a spark over a distance of 4 meters using a capacitor and an early form of dipole antenna [13]. The result of his experiments was the verification of Maxwell's theory. Some years later Marconi succeeded in transmission over further distances by sending radio-waves over the transatlantic ocean. The advances made by Maxwell, Hertz, Heaviside and many others[2] ignited a broad area of research related to electromagnetism. Telecommunications using millimeter- and microwaves has left an invaluable mark on civilization. This has led to a profound knowledge of antennas for emission and detection, and also tools for wave-guiding. Manipulation of waves requires structures that scale with the wavelength of the radiation, and the recent advancements in nanolithography [14–17] pushed the resolution of fabrication below the micrometer. As light is an electromagnetic wave, most of the antenna designs will carry over and we can apply well-known techniques to new applications.

[2] More detailed information can be found in refs [1–3].

1.2 Material properties

Drude model

The optical properties of a metal are dominated by how the free conduction electrons can move through the crystal. A simple yet elegant, and surprisingly accurate description is the model proposed by Paul Drude [18]. In the Drude approximation the conduction electrons are assumed to behave as a gas of freely moving spheres. This movement however is constantly randomized by the collisions with imperfections and defects in the lattice. An externally applied field will accelerate these charges during the time between two consecutive collisions, introducing a small average drift in the movement of the electrons. This drift will lead to an electric current $\mathbf{J}$ which is proportional to the complex conductivity $\tilde{\sigma}$ and the applied field $\mathbf{E}$ as $\mathbf{J} = \tilde{\sigma}\mathbf{E}$. The conductivity is expressed in the Drude approximation as [19]

$$\tilde{\sigma} = \frac{10^6 N e \mu_e}{1 - i\omega\tau} \,. \tag{1.8}$$

The conductivity scales linearly with the concentration of the free charge carriers N (in cm^{-3}), and the mobility of the electrons μ_e. The denominator is complex and scales with the product of the angular frequency ω and the electron collision time $\tau = m_e\mu_e/e$. The effective mass m_e depends on the band-structure of the conductors and is material dependent. The electron mobility in turn is a function of carrier concentration, band structure and temperature. For most materials these parameters have to be determined experimentally. Since the free electrons are charged and delocalized, they can be described from an electromagnetic point of view as a plasma. In bulk a plasma can be driven into a coherent oscillation, where the natural resonance occurs at the plasma frequency ω_p. In the absence of any physical boundaries, i.e. bulk, this frequency is given by [19]

$$\omega_p^2 = \frac{10^6 N e^2}{\epsilon_0 m_e} \,. \tag{1.9}$$

The expression for the conductivity in the Drude model as a function of this plasma frequency is given by

$$\tilde{\sigma} = \frac{\omega_p^2 \tau \epsilon_0}{1 - i\omega\tau} \,. \tag{1.10}$$

An expression for the material permittivity as a function of the conductivity can be derived from Maxwell's equations. Assuming a monochromatic wave with an electric field given by $\mathbf{E} = \mathbf{E}_0 \exp i(kx - \omega t)$, equations (1.2)-(1.5) can be written in the form of wave-equations, but now with $c = \sqrt{1/\mu_0\epsilon_0\epsilon}$. The relative complex permittivity $\tilde{\epsilon}$ depends on the conductivity according to

$$\tilde{\epsilon}(\omega) = \epsilon_\infty + \frac{i\tilde{\sigma}}{\omega\epsilon_0} \,. \tag{1.11}$$

The frequency-dependent electromagnetic response of the Drude-metal is obtained when the conductivity in the above expression is replaced with that of equation (1.10).

Surface plasmon polaritons

Metals with a finite conductivity have a finite permittivity, with a real part which is negative. This allows for evanescent electric fields to penetrate into the material. When the metal has an interface with a dielectric -like glass or air- an electromagnetic excitation can exist that propagates along this interface. Such an excitation is known as a surface plasmon polariton (SPP). For a SPP at an interface normal to $\hat{\mathbf{z}}$ a solution of the wave equation is described as [20, 21]

$$E = E_0^{\pm} \exp[+i(k_x x \pm k_z z - \omega t)] \,, \tag{1.12}$$

where k_x is real and k_z is imaginary. This implies that the SPP propagates along the interface, and evanescently decays normal to the interface in both directions. The dispersion relation for k_x can be expressed in terms of the wavenumber of the incident field $k_0 = 2\pi/\lambda_0$ and the relative permittivities of the metal ϵ_m and dielectric ϵ_d as

$$k_x = k_0 \sqrt{\frac{\epsilon_m \epsilon_d}{\epsilon_m + \epsilon_d}} \,. \tag{1.13}$$

The associated plasmon wavelength is given by $\lambda_{\mathrm{SPP}} = 2\pi/k_x$. For most transparent media ϵ_d is real and has a value ranging from 1 (air) to a bit more than 10 for semiconductors in the infrared. For metals the permittivity is complex valued, with a negative real component. As a result, the square root term in equation (1.13) is larger than unity. The momenta of the free space radiation and the surface plasmon are mismatched, and surface plasmon cannot be excited through plane-wave illumination on a perfect smooth surface. Conversely, a SPP does not radiate to free space.

1.3 Scattering by small particles

When a wave propagates through a medium, any local perturbation will cause a disturbance in the wavefront. An example of such a perturbation is a small particle with metallic properties ($\mathrm{Re}(\epsilon) < 0$) whose dimensions are smaller than the wavelength of the wave it is illuminated by. Such a particle will absorb and scatter a fraction of the incident wave, dependent on properties like the size, shape, material and orientation. The remarkable response of small objects to light had already been described by Lord Rayleigh [22], a more complete theory of small scattering particles can be found in textbooks like Van de Hulst [23] and Bohren and Huffman [24]. Small conducting particles can sustain a localized resonance (LR). In the vicinity of such LRs the local electric field can be greatly enhanced [25–27]. Scattering particles which are separated less than a few wavelengths can couple through diffraction, which influences the macroscopic optical properties of the ensemble. Diffractive coupling in periodic lattices offers a new range of design parameters in tuning the spectral response of scattering structures. [28]

The complementary structure of a particle in a transparent medium, is a hole in a metallic surface. The theory of light transmitted through sub-wavelength holes was

introduced by Bethe [29], and later improved by Bouwkamp [30]. It was discovered by Ebbesen and co-workers in 1998 that periodic arrays of holes greatly enhanced the transmission of incident electromagnetic radiation [31, 32]. Random and periodic arrangements of holes have been studied for a range of frequencies and for a range of applications [33–43].

Isolated particles

For ellipsoidal particles smaller than the wavelength the scattering properties can be calculated analytically from its geometry and permittivity [44, 45]. The total amount of light that is either scattered from or absorbed by an object can be expressed as an extinction cross section, which represents the effective area of the incident field that is blocked. The extinction cross section of a scatterer is related to the average amount of work an incident electromagnetic wave does during an oscillation while driving the charges of the scatterer. This cross section can be expressed in terms of the wavenumber k, the polarization of the scatterer $\mathbf{p}$ and the incident electric field $\mathbf{E}^{\text{inc}}$ according to [46]

$$C_{\text{ext}} = 4\pi k \frac{\text{Im}(\mathbf{E}^{\text{inc}} \cdot \mathbf{p})}{|\mathbf{E}^{\text{inc}}|^2} \,. \tag{1.14}$$

The polarization in turn, depends on the incident field, the properties of the scatterer like material and shape. The properties of the scatterer are described by the polarizability tensor α, relating the polarization and the local field as $\mathbf{p} = \alpha \mathbf{E}^{\text{loc}}$. For an ellipsoidal particle surrounded by a homogeneous medium this polarizability tensor is given by [23]

$$\alpha_m^{\text{static}} = V \frac{\epsilon_p - \epsilon_s}{3(\epsilon_p - \epsilon_s) \cdot L_m + 3\epsilon_s} \,, \tag{1.15}$$

where $m = 1, 2, 3$ represents the principal axes of the ellipsoid with corresponding lengths d_m, and V the volume of the particle. The permittivities of the particle and of the surrounding dielectric medium are ϵ_p and ϵ_s respectively, and L_m is the shape factor taking account for the flattening of the particle. This factor consists of an integral and is given by

$$L_m = \int_0^\infty \frac{d_1 d_2 d_3 \; ds}{2(s + d_m^2)^{\frac{3}{2}} \cdot (s + d_1^2)^{\frac{1}{2}} \cdot (s + d_2^2)^{\frac{1}{2}} \cdot (s + d_3^2)^{\frac{1}{2}}} \,. \tag{1.16}$$

For spherical particles the shape factor is 1/3 for the three axes. In most of the calculations presented in this thesis, we consider disk-shaped particles that have two equal principal axes defining their diameter and a shorter one defining the height of the disk. The shape factors for the particles described in this thesis are for the long axes typically in the range $0.01 < L_m < 0.03$.

For small spheres the denominator in equation (1.15) vanishes when $2\epsilon_s = -\epsilon_p$ and the static polarizability diverges. This results in a plasmonic resonance which is limited due to losses in the metal. For a scatterer that consists out of a perfect metal,

i.e. $\mathrm{Re}(\epsilon_\mathrm{p}) \to -\infty$, the material properties drop out of equation (1.15) and the static polarizability simplifies to

$$\alpha_m^{\mathrm{static}} = \frac{V}{3L_m} \, . \tag{1.17}$$

Perfect metallic scatterers, or scatterers with a large negative permittivity, can still be resonantly driven. The resulting resonance in these particles will be referred to as a localized resonance (LR) and is dominated by radiative damping and dynamic depolarization. In the modified long wavelength approximation (MLWA), which holds for particles of subwavelength dimensions, the polarizability is approximated as [46]

$$\alpha_m = \frac{\alpha_m^{\mathrm{static}}}{1 - \frac{2}{3} ik^3 \alpha_m^{\mathrm{static}} - \frac{2k^2}{d_m} \alpha_m^{\mathrm{static}}} \, . \tag{1.18}$$

The term $\frac{2}{3} ik^3 \alpha_m^{\mathrm{static}}$ corresponds to the dynamic depolarization, and the term $\frac{2k^2}{d_m} \alpha_m^{\mathrm{static}}$ to the radiative damping. It should be noted that the correction of equation (1.18) is not restricted to metallic particles only, and in general holds for particles with any permittivity. For an isolated particle the local field is identical to the incident field, i.e. $\mathbf{E}^{\mathrm{loc}} = \mathbf{E}^{\mathrm{inc}}$, and the expression for the extinction cross section simplifies to

$$C_{\mathrm{ext}} = 4\pi k \, \mathrm{Im}(\alpha_\mathrm{m}) \, , \tag{1.19}$$

when driven by an electric field polarized along one of the axes m. Typical extinction spectra of an isolated scatterer that exhibits a LR are shown in figure 1.1(a). The extinction spectra in this figure are simulated with the finite-difference in time-domain (FDTD) method for doped Si scatterers with diameters of 35 μm (blue curve) and 65 μm (red curve) respectively, surrounded by a medium with a refractive index $n = 2$. The extinction efficiency is defined as the ratio of the extinction cross-section and the geometrical cross section of the scatterers at normal incidence. The localized resonances shown are broad due to the large losses as a result of the scattering and radiative damping. The resonance frequency for either of the particles is related to the particle diameter as a result of the radiative damping.

Periodic structures

Most of this thesis will deal with ensembles of conducting scatterers, and how the ordering of these scatterers influences the interaction with incident electromagnetic waves. The ensemble with the maximum order is a periodic lattice. The electromagnetic properties of such systems have been studied theoretically for more than half a century, mainly focusing on microwaves [47–50]. Recent developments in the physics of scattering in periodic arrangements of particles were inspired by studies of complementary structures: A periodic array of holes in a metal film exhibits extraordinary transmission of light at certain frequencies. This was experimentally demonstrated by Ebbesen and co-workers in 1998 [31], and the explanation they gave was in terms of propagating surface plasmons. This inspired further research

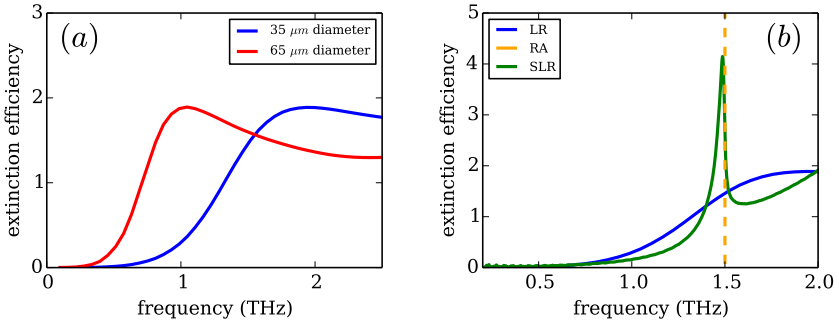

Figure 1.1: Numerical simulation of the extinction efficiency of ellipsoidal scatterers. (a) Localized resonance for isolated doped Si particles of 65 µm (red curve) and 35 µm (blue curve) in diameter surrounded by a medium with refractive index $n = 2$. (b) When a LR (blue curve) couples to a diffraction order in the plane of an array (yellow dashed line) it gives rise to a SLR (green curve). All scatterers have a height of 1 µm.

on plasmonics [51–55]. These studies were extended further using different materials and different frequency regimes [56–64]. Gómez Rivas and co-workers were the first to demonstrate experimentally the extraordinary transmission of a hole array at THz frequencies using doped semiconductors [65].

Complementary to the enhanced transmission of an array of holes, a periodic array of particles will exhibit an enhanced extinction at certain frequencies. This is illustrated in figure 1.1(b). The blue curve represents the extinction spectrum of an isolated cylindrical Si disk with a height of 1 µm and a diameter of 35 µm in a quartz environment. Since this scatterer only interacts with the incident field the extinction spectrum is that of a LR, which is characterized by a broad resonance. A periodic array of scattering particles has diffraction orders. These orders are determined by the periodicity Γ of the structure and both the frequency ν and angle of incidence θ of the illumination [66]. Of special interest are the diffraction orders that lie in the plane of the array. The frequency where such a condition occurs is called a Rayleigh anomaly (RA) and is given by

$$\nu_{\mathrm{RA}} = \frac{mc}{n\Gamma\left(1 \pm \sin(\theta)\right)} \ , \ m = 1, 2, 3 \ldots \tag{1.20}$$

where c is the speed of light in vacuum and n the refractive index of the surrounding medium. For an ensemble of scatterers with a length of 35 µm in a square lattice with $\Gamma = 100$ µm pitch that is illuminated at normal incidence, the spectrum changes to the one indicated by the green curve in figure 1.1(b). The most pronounced change in the spectrum is the enhanced extinction efficiency at the RA condition at 1.5 THz, and is indicated in figure 1.1(b) with the yellow dashed line. This reshaping of the spectrum is the result of the enhanced radiative coupling of the localized resonances in the particles due to diffractive coupling in the plane of the array. These remarkable

effects were first observed by Wood [67], and elaborated on by Lord Rayleigh [68, 69].

The optical response as described above is called a surface lattice resonance (SLR) [70], which is a hybrid plasmonic-photonic mode and can combine properties from both the individual scatterer and the diffraction grating. [70–80]. Aside from reshaping the extinction spectrum, at specific frequencies the electromagnetic fields get enhanced over large volumes. An illustration of this coupling is shown in figure 1.2.

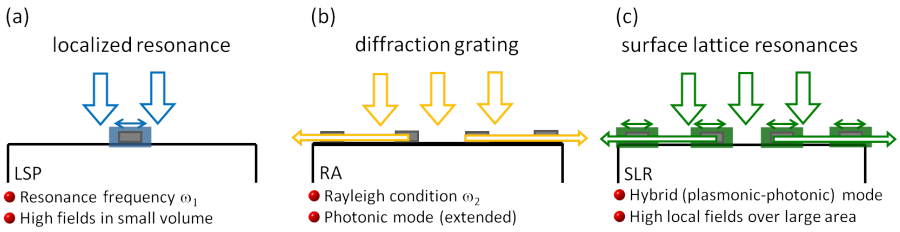

Figure 1.2: Localized resonances scatter an incident plane wave (represented by the big vertical arrows) into a Rayleigh anomaly, or diffracted order in the plane of the array (represented by the long horizontal arrows) in (b) and (c). The enhanced radiative coupling of LRs (a) through diffraction (b) can give rise to surface lattice resonances (c).

1.4 Electromagnetic spectrum and THz frequencies

The visible part of the spectrum, with wavelengths roughly in the range of 400 nm-800 nm, has been a subject of study for more than a millennium. Although it took until the late nineteenth century before the nature of light was properly understood, engineering applications using lenses were already common use in the 16^{th} century. At first mainly as spectacles, but later on also for telescopes and microscopes. Since Maxwell it is known that light is an electromagnetic wave and from the range of visible frequencies the spectrum can be extended to frequencies which are either higher or lower as is illustrated in figure 1.3. At high frequencies/short wavelengths radiation has a strong and ionizing interaction with matter, and as a result it finds applications ranging from medicine, lithography, crystallography and forensics. The near-infrared (800 nm-2500 nm) finds applications in a wide range of topics, ranging from agriculture to fiber-optics communication [81].

At low frequencies/long wavelengths one finds the radio waves, whose full spectrum ranges from 3 kHz-300 GHz. Since the earth lower atmosphere is mostly transparent for radio waves, they turned to be excellent for long-range communication purposes. Electric dipole antennas radiate the most efficient when the wavelength is twice the antenna length [82]. Since the radio-waves have typical lengths ranging from centimeters to hundred meters it is relatively straightforward to mechanically engineer antennas that radiate in this range. The efforts of Marconi early in the 20th century paved the way for implementing this technology in defense and industrial applications.

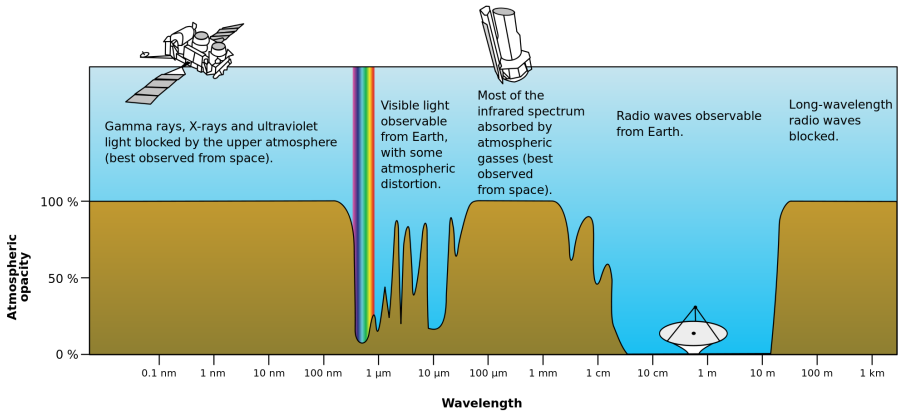

Figure 1.3: Electromagnetic transmittance, or opacity, of the Earth's atmosphere (Source: NASA).

As a result of on-going research for almost a century the field is well developed and very mature.

The spectrum of terahertz frequencies bridges the infrared and the radio frequencies, and is typically defined as ranging from 0.1 THz-10 THz with corresponding free-space wavelengths of 3 mm-30 µm. The photon-energies that can be associated with this range are 0.4 meV-40 meV. This part of the spectrum is characterized by a rich and versatile response of a variety of materials, of which a few are listed in table 1.1. Liquids have relaxation modes at THz frequencies [83], and applications lie in the domain of inspection of products, for instance in agriculture [84]. Polyatomic gases have very characteristic rotational and vibrational modes [85], and THz spectroscopy can be used for instance in tracing air pollution [86]. Modes related to local deformation and stretching in larger (bio-)molecules are addressable at THz frequencies [87, 88], and sensing applications can be used for medical screening [89]. Towards applications in solid-state physics the THz frequency range covers lattice vibrations in crystalline structures, the response from the conduction electrons in metals and semiconductors, and the bonding energy of Cooper pairs in superconductors [86, 90–94].

Material	Interaction	Application
liquid	relaxation	agriculture, inspection
gas	rotational, vibrational	pollution
biomolecules	stretching	medical
periodic structures	photonic band	sensing, integrated circuits
semiconductors	free carrier, phonon, plasmon	wafer and device inspection

Table 1.1: Materials with their responses to THz radiation, and applications. Data taken from refs. [86] and [95].

Semiconductors

In an intrinsic semiconductor there are as many free electrons as there are available states in the valence band. When all these states are occupied there exists a symmetry in the flow of charge, and as a result the material is insulating [19]. For electrons that occupy states in the conduction band this symmetry can be broken upon application of a finite electric field, which allows the semiconductor to conduct electrical charge. The ability to control the presence of charges in the conduction band is one of the key properties of semiconductors. This control can be achieved by exciting carriers from the valence band to the conduction band through thermal- [96–98] or photo-excitation [41, 99–102]. Alternatively one can simply change the concentration of charge carriers through chemical doping [103] or electrical injection of charge carriers [98]. Chemical doping can be achieved by substituting atoms for others with more (n-type) or less (p-type) free electrons. Silicon can be doped with arsenide or gallium, while GaAs is usually doped with zinc or silicon [104]. Using chemical doping concentrations of charge carriers can be reached that are in the order of 10^{19} cm^{-3}. Photo-excitation can be achieved through absorption of photons with an energy exceeding the bandgap of the semiconductor. An electron-hole pair that is created contributes to the transport of charge, until it recombines.

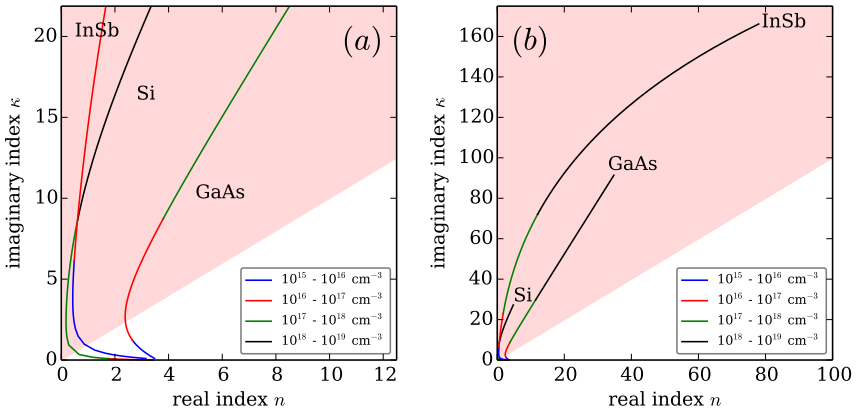

Figure 1.4: Complex refractive index $n + i\kappa$ for Si, GaAs and InSb at 1 THz as a function of the charge carrier concentration. The curves are calculated with the Drude model using the parameters as mentioned in the text. Panel (a) shows a zoom of panel (b). The shaded areas indicate the values of n and κ for which the real component of the permittivity is negative, i.e. the material has a metallic behavior.

The finite conductivity induced by the free charges in the semiconductor can be modeled with the Drude model. Using equations (1.10) and (1.11) with the proper material parameters, one can obtain the optical constants as a function of frequency and carrier concentration. Silicon (Si) has electrons with a relative large effective

mass of $0.98m_0$ [105] and a low mobility of 0.1 $m^2V^{-1}s^{-1}$ [106]. As a result one needs to go to relatively large doping concentrations for inducing a metallic behavior in Si. Nevertheless, Si is relevant due to the well-developed infrastructure for industrial applications. Indium antimony (InSb) is a semiconductor in which the electrons have a very large mobility in the order of 5 $m^2V^{-1}s^{-1}$ and a low effective mass of $0.0153m_0$ [107]. The small bandgap of 0.16 eV results in metallic behavior at room temperature, and for semi-insulating properties at THz frequencies one needs to cool the sample down in order to condense the majority of the electrons to the valence band. Gallium arsenide (GaAs) is very well suited for photo-excitation. The bandgap of 1.424 eV corresponds to 871 nm and allows for absorption of pulses from a Ti:Sapphire oscillator. In addition the mobility of 0.5 $m^2V^{-1}s^{-1}$ [108] is sufficiently large and the effective electron mass relatively low with $0.063m_0$.

The complex refractive index of a medium is given by the square root of the relative permittivity as $n + i\kappa = \sqrt{\tilde{\epsilon}}$. The carrier dependence of this refractive index at 1 THz for the semiconductors mentioned above is shown in figure 1.4. When $n < \kappa$ a material has a negative real part of the dielectric constant, and consequently behaves as a metal. This region is indicated by the shaded red background in figure 1.4. For the lowest carrier concentrations the conductivity is practically zero, and the refractive index is real and positive as can be seen in figure 1.4(a). The real part of $i\tilde{\sigma}$ in equation (1.11) is negative, and when the carrier concentration is further increased it will reach a point where $\mathrm{Re}(\tilde{\epsilon}) = 0$. Around this condition the real index n has a minimum. A further increase in the carrier concentration will make the semiconductors metallic. The differences between the responses of the semiconductors shown in the figures can be directly related to the respective electron mobilities and effective masses.

THz plasmonics

With the ability to induce a metallic behavior in semiconductors, we can investigate their plasmonic behavior. Using the respective effective electron masses as mentioned above with equation (1.9), the plasma frequencies can be calculated as a function of the charge carrier concentration N. This is shown in figure 1.5(a) for Si, GaAs and InSb. In silicon the electrons have the largest effective mass, and hence the plasma frequency is the lowest. For carrier concentrations in the range of 10^{16} cm^{-3} to 10^{19} cm^{-3} the plasma frequency ranges from 1 THz to roughly 100 THz.

The corresponding wavelengths of the SPP for all three semiconductors are shown in figure 1.5(b), as calculated with equation (1.13). The interface along which the SPP propagates has one of the semiconductors on one side and quartz (with $n = 2$) on the other side. The frequency under consideration is 1 THz. The horizontal dashed line in the figure indicates 150 µm, which is the wavelength of a wave with a frequency of 1 THz in a dielectric of refractive index $n = 2$ far away from the interface. All three semiconductors discussed here asymptotically approach the wavelength of a wave propagating only in the dielectric for the largest carrier concentrations. At these conditions the permittivities are such that only a small fraction of the SPP is penetrating into the metal and most of the mode exists mainly in the dielectric.

As the carrier concentration is decreased the SPP is allowed to penetrate further into the semiconductor and as a result the plasmon wavelength decreases. When the carrier concentration is lowered even further the semiconductor eventually stops being metallic and becomes a normal dielectric. When this occurs the plasmon wavelength increases again, which is outside the range of figure 1.5(b) for Si and InSb.

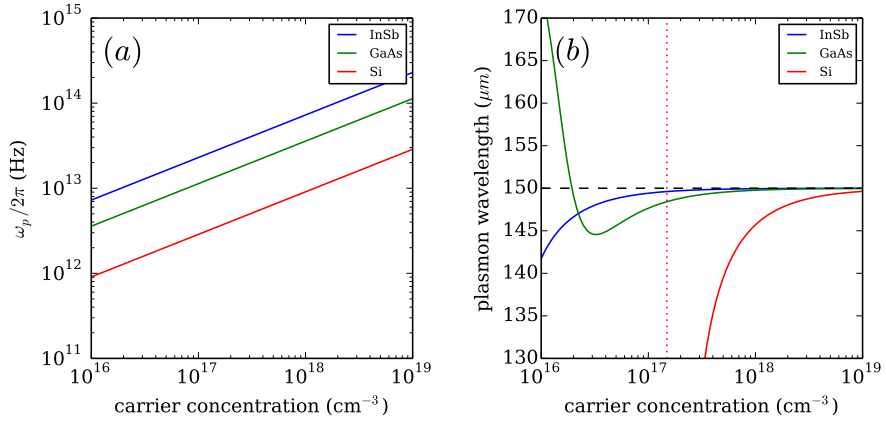

Figure 1.5: Plasma frequency (a) and the plasmon wavelength λ_{SPP} at the semiconductor-quartz interface for 1 THz (b) as a function of the charge carrier concentration for InSb, GaAs and Si. The dashed line in (b) indicates the free-space wavelength in the quartz medium.

The vertical dotted line indicates a carrier concentration of $N = 1.45 \times 10^{17}$ cm^{-3}, which is where equation for Si (1.13) diverges. For the lowest carrier concentrations shown in figure 1.5(b) the plasmon wavelength exceeds the wavelength of a wave that propagates only in the dielectric. This is a result from $\mathrm{Re}(\epsilon_{\mathrm{d}}) > \mathrm{Re}(\epsilon_{\mathrm{m}}) > 0$. The range of carrier concentrations in Si where the plasmon wavelength is significantly reduced has limited experimental use for the content described this thesis. Due to the low electron mobility in Si, the extinction cross sections of Si scatterers at moderate carrier concentrations are too low to be properly resolved in a standard THz-spectrometer. For carrier concentrations that are sufficiently large for the extinction cross sections of the scatterers to be resolved experimentally, the plasmon wavelength is reduced by less than a percent. In GaAs the plasmon wavelength is reduced by a few percent in the range of carrier concentrations discussed in this thesis. Although the direct plasmonic contributions can be small in scatterers that are made from these semiconductor materials, the scatterers will sustain a localized resonance as a result of the radiative damping. This opens up possibilities to study the scattering behavior of such semiconductor structures in more detail.

1.5 Terahertz generation and detection

Due to the absence of practical sources emitting in the spectral region of THz frequencies, this range became known as the 'THz gap' [86] during the former century. The energies of typical THz radiation are too low for sources related to light emitting diodes (LEDs), and the frequencies are too high for electronics. A number of breaktroughs was seeded by the arrival of powerful titanium doped sapphire (Ti:Sapph) oscillators in the 1980s. The ultrashort and intense pulses from these oscillators in the near infrared proved very useful for the generation and detection of single-cycle THz pulses. This section explains two common techniques used for generating and detecting these pulses, namely photoconductive antennas and optical rectification in non-linear crystals. For a more in-depth treatment one is referred to Ulbricht et al. [109] and Dexheimer [91].

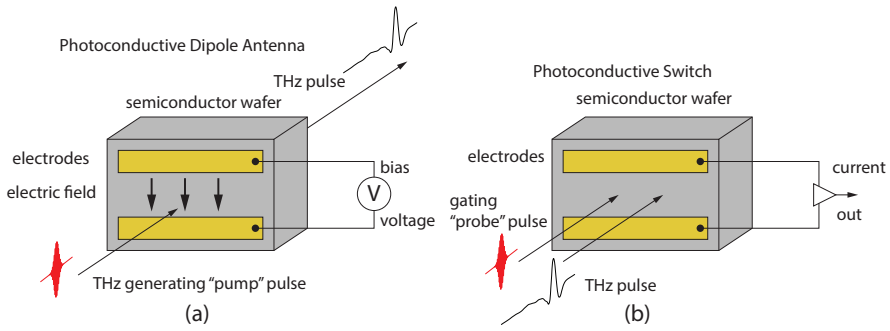

Figure 1.6: Schematic drawing of a photoconductive dipole antenna and switch, used for THz generation (a) and detection (b). Image after photonicswiki.org.

Photo-conductive antennas and switches

A photo-conductive antenna for THz generation usually consists out of a semiconductor wafer on which a thin layer of low-temperature grown GaAs is deposited, on top of which a pair of biased electrodes are placed. A schematic representation of a typical antenna is shown in figure 1.6(a). The GaAs can absorp the laser pump pulse from the Ti:Sapph oscillator, after which the induced charge carriers are accelerated towards the anode until they recombine. As a result of this acceleration and de-acceleration the electrons emit a single-cycle pulse centered around THz frequencies. The same antennas can be used as photo-conductive switches for THz detection. A NIR laser pulse will induce charges in the GaAs thin layer. When a THz pulse passes at the same time, the electric field of the THz pulse will drive the electrons to one of the electrodes and a small current will flow. The strength of this current is proportional to the amplitude of the THz electric field, and can be detected using a current amplifier. Since the lifetime of the carriers is in the order of sub-picoseconds, only a fraction of

the THz pulse is sampled. By using a delay-line for controlling the relative arrival of the two pulses on the switch a full THz transient can be acquired.

Nonlinear crystals

Optical rectification is a phenomenon which can occur in certain nonlinear crystals [110]. One of these crystals is ZnTe, which emits a single-cycle electromagnetic pulse centered around 0.5 THz when hit with an intense and short (< 100 fs) optical pulse centered at a wavelength of 800 nm. This is sketched in figure 1.7(a). Following the description of Dexheimer [91], this can be explained as follows: A series expansion of the relation between the polarization and the electric field in a material $P = \chi(E)E$ can be written as

$$P = \left(\chi_1 + \chi_2 E + \chi_3 E^2 + \chi_4 E^3 ...\right) E \ . \tag{1.21}$$

For optical rectification the crystal needs to have a nonzero second order nonlinear coefficient such that

$$P_2 = \chi_2 E^2 \ . \tag{1.22}$$

When driven by a superposition of two fields of different frequency $E = E_0 \cos \omega_1 t + E_0 \cos \omega_2 t$ this polarization can be expressed as

$$P_2 = \chi_2 \frac{E_0^2}{2} \left[\cos\left(\omega_1 - \omega_2\right)t + \cos\left(\omega_1 + \omega_2\right)t\right] \ . \tag{1.23}$$

The term of interest here is the frequency difference term $\cos\left(\omega_1 - \omega_2\right)t$. An 800 nm pulse with a duration of 100 fs has a bandwidth of 10 THz centered around 375 THz. Although THz frequencies are generated over the full bandwith of 10 THz, absorption and dispersion limit the effective bandwidth to the order of a few THz [91].

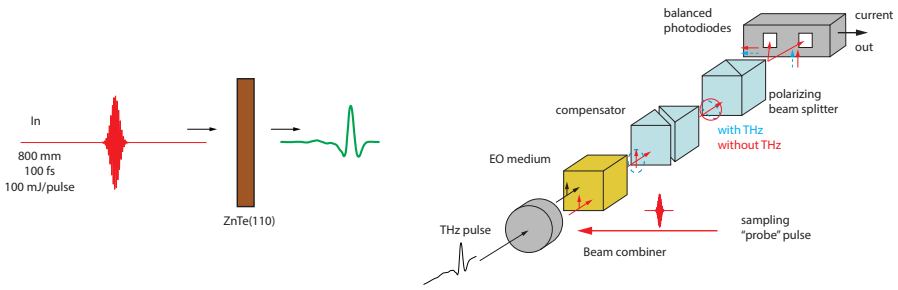

(a) **(b)**

Figure 1.7: (a) THz generation using optical rectification, and (b) detection using electro-optic sampling. Images after photonicswiki.org.

electro-optic (EO) sampling is based on the same non-linearity as optical rectification regarding the non-linear polarization term in equation (1.21). The refractive index of a second order non-linear material can be expressed as

$$n = \sqrt{\epsilon} = \sqrt{1 + \chi(E)} \approx \sqrt{1 + \chi_1 + \chi_2 E} \,. \tag{1.24}$$

For moderate non-linear coefficients χ_2 and low field strengths this approximates as an offset index of $n_0 = \sqrt{(1 + \chi_1)}$ and a small perturbation:

$$n \approx n_0 + \frac{\chi_2 E}{2 n_0} \,. \tag{1.25}$$

In zincblende crystals like ZnTe the χ_2 coefficients are only present for certain polarizations and propagation along specific crystallographic axes. When a THz pulse co-propagates together with a sub-ps NIR 'probe' laser pulse through one of these crystals, and at 45° from both axes, the probe pulse will experience birefringence. As a function of the THz amplitude the polarization of the NIR probe will change from linear to elliptical. When a quarter-waveplate changes the polarization state from (nearly) linear to (nearly) circular, the intensity difference between the two primary polarization axes will be proportional to the THz amplitude. This difference can be measured using a polarizing beam-splitter and a pair of balanced photo-diodes. By changing the temporal delay between the THz and NIR pulses the full THz transient can be acquired.

1.6 Outline of this thesis

This thesis discusses the resonant behavior of semiconductor microstructures, as individual scatterers or as a part of an ensemble in a periodic lattice. In this introduction chapter the historical background and scientific context has been provided, as well as an explanation of the generation and detection of THz radiation. *Chapter 2* elaborates in more detail on the experimental methods, and introduces how the transfer-matrix method can be applied for the characterization of doped semiconductor thin films. In *Chapter 3* we demonstrate how a conically tapered waveguide allows for far-field detection of single THz antennas. By placing the antenna in front of a conically tapered waveguide the detection limit of the THz spectrometer was enhanced by an order of magnitude. As explained in *Chapter 4*, a theoretical study has been done on how the radiative coupling of localized resonances is enhanced by diffraction, when the diffraction order is in the plane of the array. The resulting mode is a surface lattice resonance (SLR). An algorithm based on the Drude model and a coupled dipole model (CDM) gives an insight in how a SLR is formed both as function of the structure dimensions and the free electron concentration in the semiconductor, and demonstrates how the extinction spectrum can be tuned. An experimental study has been performed on semiconductor structures in a periodic array, as presented in *Chapter 5*. Structures that are etched out of As-doped Si are studied, as well as periodic arrays that are projected on a continuous GaAs layer. For a fixed pitch the localized resonance is varied over a broad spectral range by changing the particle size. The experimental results are compared with finite-difference in time-domain simulations, and CDM calculations. This allows us to explain the results in terms of diffractive coupling, and give insight in the delocalization of the near field. In *Chapter 6* we explore the physics of a lattice of displaced and detuned dipoles. In such a periodic lattice the interference of SLRs reshapes the collective extinction spectrum as a function of the displacement between the dipoles. When the dipoles are detuned the two SLRs form a hybrid mode, which results in an additional maximum in the far-field extinction and an induced transparency window. The CDM calculations are verified with numerical simulations.

Chapter 2

THz-TDS and material characterization

Terahertz time-domain spectroscopy is a powerful technique for contact-free and non-destructive analysis of the optical and electronic properties of materials. In this chapter the experimental setups which are used later in this thesis are introduced and explained. The time-domain property of the experimental technique is used for retrieving the optical constants of thick substrates, and the electronic properties of thin films of doped semiconductors. This retrieval is done with an analysis based on the transfer matrix method. For photo-excited carriers in a thin GaAs film this method is used to estimate the effect on the terahertz transmission due to ambipolar carrier diffusion.

2.1 Experimental setups

As the name already indicates, THz time-domain spectroscopy (THz-TDS) allows for the detection of THz pulses as a function of time. Chapter 1 introduced two commonly used mechanisms for the generation and detection of THz pulses. This section introduces the 2 experimental setups that were used for acquiring the experimental results presented in this thesis. Both setups are based on the same principle: A short near-infrared laser pulse is split into multiple beams. One beam is used for THz generation, another for THz detection and an optional third beam for optical pumping of the sample. The setups differ mainly on the type of laser which is used, and the mechanism of generating the THz pulses.

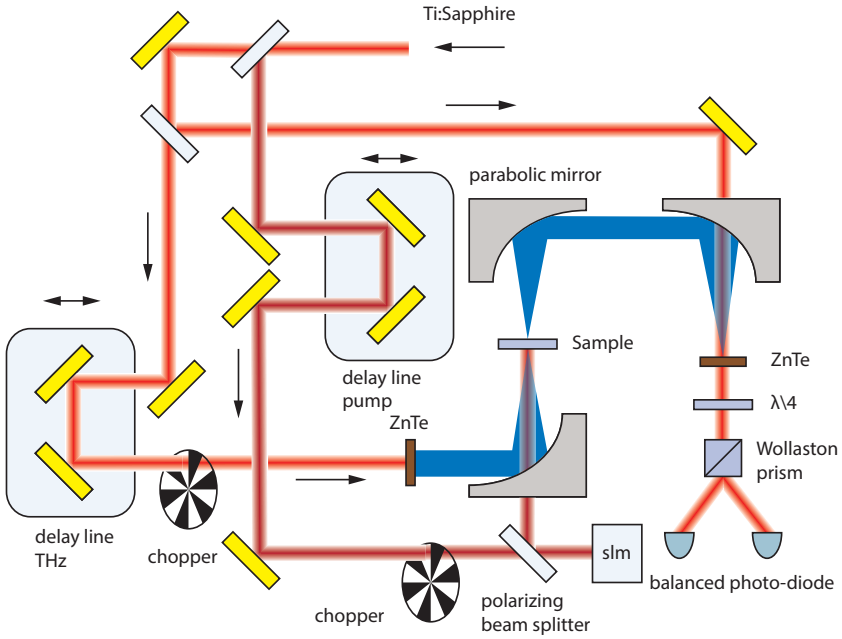

Figure 2.1: Schematic representation of THz-TDS setup 1, driven by an amplified laser. A 1 kHz pulse train of amplified NIR pulses is split into three arms. 19% travels over the THz delay line and is used for the generation of THz pulses through optical rectification in a ZnTe crystal, 1% of the intensity is used for electro-optic sampling, and the remaining 80% of the intensity can be used for optically pumping the sample. Off-axis parabolic mirrors are used for redirecting the THz beam, indicated by the blue beam, from the source via the sample towards the detector. Either the THz signal or the optical pump can be mechanically chopped to enable lock-in detection, and both arms contain a delay-line for controlling the relative timing of the pulses. The projection of the optical pump on a sample is done via a polarizing beam splitter and a spatial light modulator.

2.1.1 Setup 1

A typical layout of an experimental setup based on optical rectification for THz generation and electro-optic (EO) sampling for detection is shown in figure 2.1. The setup is driven by an amplified titanium doped sapphire (Ti:Sapph) laser for which a more detailed description can be found in refs [91, 109]. The pulse train emitted by this laser has pulses centered at a wavelength of 800 nm and a duration of 100 fs. The repetition rate is 1 kHz, and the energy per pulse is ~ 5.8 mJ. Out of this intensity 19% is used for the generation of THz pulses in a 0.5 mm ZnTe crystal. 1% of the intensity is used for electro-optic sampling in another 0.5 mm ZnTe crystal. The remaining 80% of the intensity can be used for band-to-band carrier excitation in a semiconducting sample. These three pulses propagate in three optical paths, as can be seen in figure 2.1, and will be explained one after another. From the laser beam that enters at the top from the right the pump arm is split off first using a beam splitter. It travels over a delay line, and passes a chopper and a polarizing beam splitter. This beam splitter is aligned such that the transmission axis is parallel to the incident polarization. The spatial light modulator (SLM) is a pixellated nematic LCD, in which per pixel the polarization state of the reflected light can be controlled. As a result it controls the spatial intensity profile of the beam that is reflected onto the sample through a hole in one of the parabolic mirrors. The second arm is the THz generation arm and is the one that is transmitted by the second beam splitter. As for the pump the NIR pulse travels over a delay line and a chopper. Once it hits a ZnTe crystal a single-cycle THz pulse is generated, which is focused with an off-axis parabolic mirror onto the sample. The THz signal which is transmitted by the

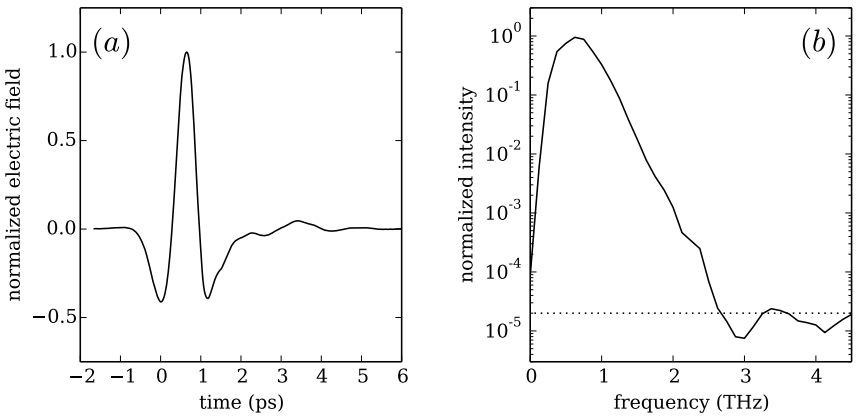

Figure 2.2: Transient (a) and intensity spectrum (b) of the THz pulses generated by optical rectification and detected with electro-optic sampling. In both figures the signals are normalized to the maximum value. The noise level in figure (b) is around 2×10^{-5}, as indicated by the black dotted line.

sample is focused on a ZnTe crystal via another pair parabolic mirrors for electro-optic detection. In the ZnTe crystal the THz pulse co-propagates in space and time with the third pulse, the probe pulse. As described in section 1.5 of this thesis, the polarization state of the probe pulse changes in the ZnTe crystal under the influence of the THz amplitude. This polarization state is measured by sending the probe pulse through a quarter-waveplate and a Wollaston prism, where the intensity difference between the two orthogonal polarizations is detected with a pair of balanced photo-diodes (BPD). The output voltage of the BPD is connected to a lock-in amplifier to retrieve a signal, which is proportional to the amplitude of the THz electric field. By scanning the time delay between the generation and detection pulses with the delay line, the full time domain signal of the THz transient can be acquired. In the focus-point at the sample position the THz pulse has a full width at half maximum (FWHM) of 1.7 mm. The experimental results presented in the remainder of this chapter and chapter 5 are acquired using a setup based on this configuration. A typical transient measured in this configuration is shown in figure 2.2(a), where the amplitude of the electric field is normalized to the maximum of the pulse. The chamber containing the THz radiation has been flushed with nitrogen in order to suppress unwanted absorption due to the presence of water vapor in the ambient air. The complex spectrum of this pulse is acquired by Fourier transforming the transient according to

$$\tilde{E}(\nu) \equiv F\{E(t)\} = \int E(t) e^{i2\pi\nu t} dt \; . \tag{2.1}$$

The spectrum of the transmitted intensity, which is the absolute square of equation (2.1), is shown in figure 2.2(b). As for the transient the spectrum is normalized to the maximum value. The intensity is maximum at 0.5 THz, and has a noise level around 2×10^{-5}. The bandwidth with at least an order of magnitude signal-to-noise in the intensity ranges from 0.1 THz to 2.0 THz.

2.1.2 Setup 2

A typical layout of an experimental setup based on a photo-conductive antenna (PCA) for THz generation and electro-optic (EO) sampling for detection is shown in figure 2.3. The setup is driven by a Ti:Sapph oscillator which is not amplified. This oscillator delivers a pulse train of 20 fs pulses centered at a wavelength of 800 nm and with a repetition rate of 75 MHz. The average optical output power is in the order of 1 W. Each pulse in the Ti:Sapph pulse train is split into two beams using a beam splitter. One pulse, the generation pulse, is used to generate a broadband and linearly polarized single-cycle THz pulse in the PCA. For noise reduction the bias of 20 V on the PCA is modulated with a duty cycle of 50% at $\sim$ 10 kHz for lock-in detection. The THz pulse is focused on a sample by a pair of off-axis parabolic mirrors. The transmission of the THz pulse through the sample is directed by another pair of parabolic mirrors onto a ZnTe crystal for detection. This detection is similar to the one explained in section 2.1.1 for setup 1. The configuration of setup 2 is used for the experimental results presented in chapter 3.

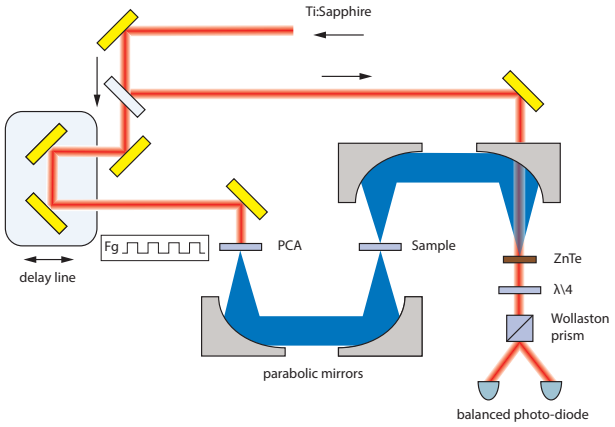

Figure 2.3: Schematic representation of THz time-domain spectrometer 2, driven by a femtosecond Ti:Sapph laser. A photo-conductive antenna (PCA) is used for THz generation and electro-optic sampling in a ZnTe crystal is used for detection. Off-axis parabolic mirrors are used for redirecting the THz from the source via the sample towards the detector. A delay-line controls the timing between the generation and detection pulses. The 20 V bias of the PCA is modulated around 10 kHz for suppression of background noise, and the signal from the balanced photo-diodes is sent to a lock-in amplifier.

2.2 Sample characterization

This section describes how THz-TDS can be used for the characterization of materials. The complex permittivity of the substrates and semiconductor thin films used in this thesis are obtained as explained in appendix A in more detail, using an analysis based on the transfer-matrix (T-matrix) method.

Substrates and bonding layers

Conducting thin films are interesting for the excitation of surface plasmon polaritons. However, for mechanical stability these films are often attached to a supporting substrate. The optical properties of these substrates deviate from those of air, and reduce and delay the transmission of the THz pulse. For a careful design of the plasmonic structures, and an accurate analysis of the results it is important to know the optical constants of the different materials forming the sample.

The determination of the optical constants of the materials used as substrates can be done with THz-TDS by comparing the transmission of a THz pulse through the substrate with a reference. When the thickness of the substrate is known one can use the T-matrix method to extract the frequency-dependent complex refractive index. Figure 2.4(a) shows the time-domain response of the THz-TDS spectrometer with the black curve, and the transmission through a 1 mm amorphous quartz substrate (blue curve), and a 2 mm crystalline quartz substrate (red curve). The reduction in

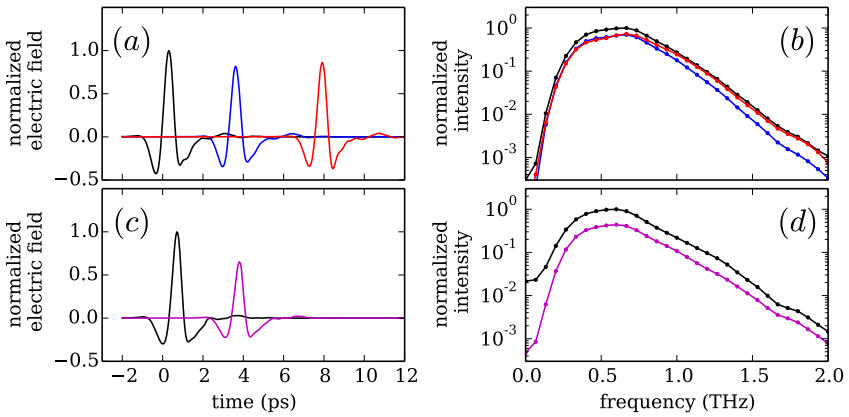

Figure 2.4: Time domain transients of the transmission through amorphous (blue curves) and crystalline (red curves) quartz substrates (a), and a GaAs wafer (magenta curves) (c). The corresponding intensity spectra are shown in (b) and (d). The impulse response of the experimental setup without sample in each measurement session is represented by the black curves.

amplitude is caused by Fresnel reflections and absorption, while the delay in time is due to the reduced propagation velocity as result of the refractive index of the quartz being larger than 1. The fast fourier transform (FFT) is more efficiently implemented when the signal contains 2^n datapoints, with n an integer. For this purpose additional zeros are added to the THz transients when the length of the experimental data deviates from these numbers. The Fourier transform results in an amplitude transmission spectrum. These spectra are in principle complex. The absolute square of these transforms represents the intensity spectrum of the transient. For the quartz substrates and reference the intensity spectra are shown in figure 2.4(b). Figure 2.4(c) shows the transmission transient (magenta curve) for a 363 µm thick single crystalline semi-insulating (SI) GaAs wafer, and the reference transient (black curve) without any wafer. Although the thickness of this wafer is significantly less than the 1 mm of the amorphous quartz, the delay in the transmitted pulse is almost as large. This is an indication of a larger refractive index. As for the quartz substrates the transients are Fourier transformed, and the resulting intensity spectra are shown in figure 2.4(d). The intensity spectra for the substrates shown in figure 2.4 are the result of both the characteristic response of the experimental setup and the substrate transmission. This dependence on the setup can be removed through normalization. Dividing the complex amplitude measured through a sample by the complex amplitude measured through a reference results in the complex amplitude impulse response of only the sample:

$$\tilde{t}_{\text{sample}}(\nu) = \frac{\tilde{E}_{\text{sample}}(\nu)}{\tilde{E}_{\text{reference}}(\nu)} \,. \tag{2.2}$$

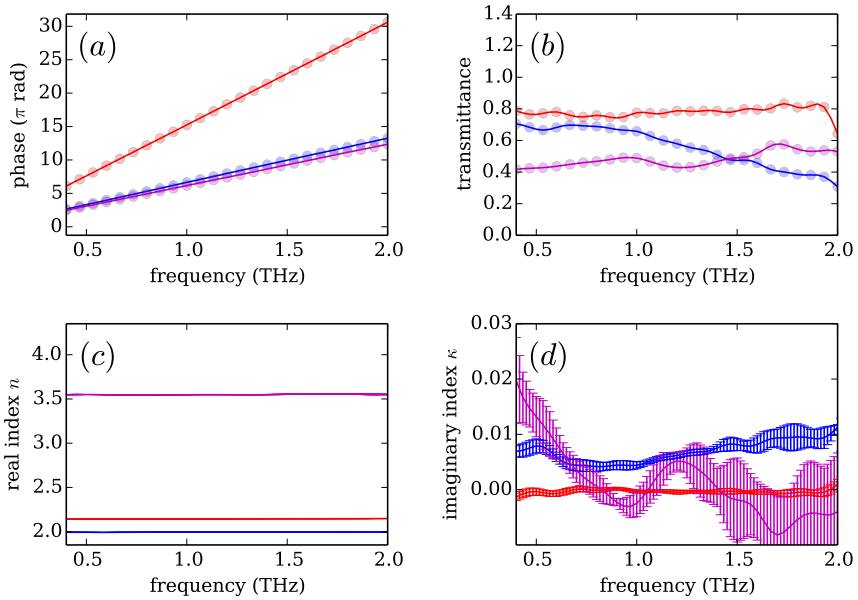

Figure 2.5: Phase delay (a) and intensity transmission spectra (b) for 1 mm thick amorphous (blue) and 2 mm thick crystalline (red) quartz substrates, and a 363 µm thick GaAs wafer (magenta). The circles represent the normalized Fourier transforms of the time domain transients shown in figure 2.4. The solid curves are the reproduced spectra using the transfer matrix method. The corresponding refractive indexes are shown in figures (c) and (d).

The two relevant properties of this response are the phase $\theta(\nu) = \arg(\tilde{t}(\nu))$ and the transmittance $T = |\tilde{t}|^2$. The phase and transmittance of the substrates, calculated from the transients in figure 2.4 are shown in figure 2.5(a) and (b) and indicated with the circles for the amorphous (blue) and crystalline (red) quartz substrates, and the GaAs wafer (magenta). The error in the transmittance spectra for these substrates due to noise in the experiment, falls within the thickness of the dots. In good approximation the relation between the phase and the frequency in figure 2.5(a) are straight lines for all substrates, where the slope is determined by the product of the substrate thickness and the refractive index. The straight lines indicate that the substrates are free of dispersion. The transmittance spectrum of the crystalline quartz substrate in figure 2.5(b) is practically flat, while for the amorphous quartz substrate the transmittance decreases somewhat for larger frequencies. The reduction in transmittance of the GaAs wafer can be attributed to a finite absorption, and possible roughness of the non-polished backside of the wafer.

With the thickness of the substrates known, we can use the T-matrix method as

described in appendix A to extract the refractive index spectra. The solid curves in figure 2.5 are the spectra calculated with the transfer matrix method, reproducing the experiments. The complex refractive indexes of the substrate were used as fitting parameters, and varied within the stochastic error of the transmittance and phase. The real and imaginary parts of the obtained complex refractive indexes are shown in figure 2.5(c) and 2.5(d), respectively. At both the front- and the backside of the substrates there will be a reflection. Since the substrates are very thick these reflections are separated in time further than the length of the acquired transient. As a consequence these reflections are not present in the spectra either. In principle the T-matrix assumes monochromatic light and includes all these reflections. The Fresnel reflection coefficients of equation (A.6) in the T-matrix model are suppressed at the interfaces to correct for this difference.

The spectra are indeed free of dispersion, and in agreement with literature [111]. For the amorphous quartz (blue) substrate the value of $n = 1.99 \pm 0.02$ is found with minor losses of $\kappa = 0.01$, and for the crystalline quartz we obtain $n = 2.14 \pm 0.02$. The crystalline quartz is practically lossless, $\kappa \approx 0$. The GaAs wafer has an index of $n = 3.55 \pm 0.02$, which is as well in agreement with value reported in the literature [112].

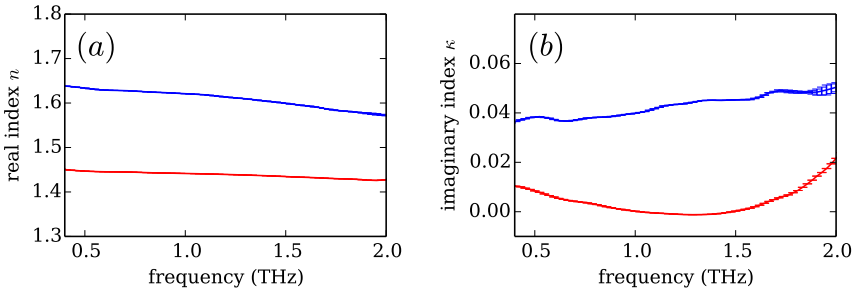

Figure 2.6: (a) and (b) refractive index spectra n and κ respectively for the mercapto-ester glue (blue curves) and BCB (red curves) bonding polymers as obtained with the transfer matrix method.

A similar analysis as for the substrates has been carried out for two polymers which are used for the bonding of thin layers of semiconductor to the carrier substrates. For this analysis thick layers are fabricated of benzocyclobutene (BCB) and a mercapto-ester glue. The investigated mercapto-ester sample has a thickness of 1 mm, the thickness of the BCB slab is estimated at 1.7 mm. The resulting spectra for the real and imaginary components of the refractive index are shown in figure 2.6(a) and (b). The BCB (red curves) has an index of $n = 1.45 \pm 0.02$, and losses in the same order as the quartz [113]. The mercapto-ester (blue curves) has a slightly larger index of $n = 1.62 \pm 0.04$ but also significantly larger losses.

Doped Si film

Fabrication

The Si samples studied in chapters 3 and 5 of this thesis consist out of As doped Si antennas, bonded to an amorphous quartz substrate. The samples were fabricated with standard micro-fabrication and processing techniques. This fabrication was done by dr. Audrey Berrier as described in references [114, 115]. The 1.5 µm thin Si layer from a commercial silicon-on-insulator (SOI) wafer is implanted (doped) with As atoms such that a concentration of free carriers in the order of 10^{20} cm^{-3} was reached. Subsequently the Si layer is transferred to a 1 mm thick amorphous quartz (fused silica) substrate, to which it is bonded with a BCB layer of 2 µm thickness. Optional patterning is achieved through optical lithography and reactive ion etching. As a last step in fabrication, the samples denoted as 'symmetric' are bonded with BCB to an amorphous quartz superstrate, embedding the Si layer at both sides in a homogeneous dielectric environment. Figure 2.7 shows illustrations of a continuous (a) and patterned (b) layer of Si bonded to a quartz substrate, a symmetric sample (c) and an optical microscope image (d). The latter has dimensions of 35 µm × 35 µm Si squares in a square lattice of 100 µm.

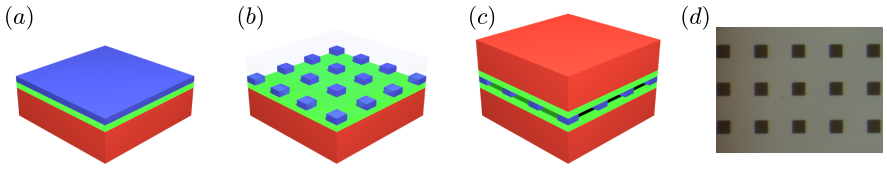

Figure 2.7: Illustration of a continuous Si film (blue) bonded with a polymer (green) to an amorphous quartz (red) substrate (a). The Si film can be etched after lithography to form a structured sample (b), and bonded to an amorphous quartz upperstrate (c) in order to embed the Si Structures in a symmetric environment. An optical microscope image of square particles with a size of 35 µm in an array of a 100 µm pitch is shown in panel (d).

Characterization

Similar to the analysis of substrates, a sample containing a doped thin Si film can be characterized to obtain its complex refractive index. For this purpose a sample is used which is symmetrically bonded to both a substrate and a superstrate, as illustrated in figure 2.7(c). Figure 2.8 shows a drawing indicating the various layers in the sample. Layers A and G represent air, layers B and F represent the 1 mm thick amorphous quartz substrates, and C and E represent the 2 µm thin BCB layers with the corresponding refractive indexes. The center layer D represents the 1.5 µm thin Si layer. In the reference measurement the Si layer is replaced by a layer of BCB with the same thickness. The T-matrix method is applied to reconstruct the experimental transmittance while solving for the complex refractive index of the thin Si film.

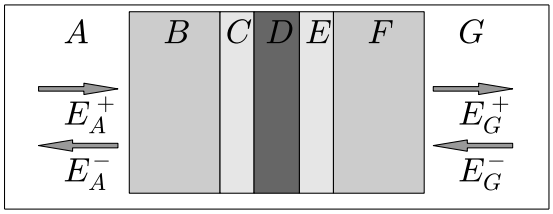

Figure 2.8: Schematic representation of the layers in a symmetric bonded sample containing the doped semiconducting thin layer. Layers A and G represent air. Layers B and F represent the 1 mm thick substrates, C and E are the polymer bonding layers and D is the semiconductor layer. The figure is not to scale.

Results are shown in figure 2.9 for the real (a) and imaginary (b) components of the complex refractive index. The circles represent the experimental results, where the error-bars are a result from the uncertainty in the measured transmission spectrum. Due to the finite bandwidth in the experimental setup and the weak absorption in the amorphous quartz, the signal-to-noise ratio in the transmission is reduced at high frequencies. This leads to larger error-bars for the extracted complex refractive index. The dependence of the refractive index on the frequency can be explained as follows: For the low frequencies, the electrons are able to follow the oscillation of the incident electric field and act like a very good metal. At higher frequencies the electrons are delayed due to their finite mobility and the interaction with the incident field decreases. In the limit of very high frequencies, which exceeds frequencies used in this work, the material is expected to behave like a normal dielectric. The refractive index values obtained with the T-matrix method are fitted to the Drude model, assuming an electron effective mass of $m = 0.98m_0$ [19]. The least square error fit is represented in figure 2.9 by the black dashed curve, resulting in a charge carrier concentration of $N = 3.6 \times 10^{19}$ cm^{-3} and an electron mobility $\mu_e = 0.012$ m^{2}V^{-1}s^{-1}. The agreement between the experimental data and the fit to the Drude model is excellent, and the resulting carrier concentration is within the range used for the dopant implantation method. The electron mobility agrees with values reported in literature for similar doping concentrations [106].

Photo-excited GaAs

The silicon thin film characterized above has its metallic properties as a result of implantation with As atoms. This doping is fixed and for a given sample cannot be changed. As mentioned in section 1.4 of this thesis, a metallic behavior can also be introduced to semiconductors by photo-excitation. For this purpose GaAs is the material of choice. Its bandgap of 1.42 eV, or 871 nm, is sufficiently large to prevent thermal excitation of free charge-carriers at room temperature, but still allows for the photo-excitation of charge carriers with the pulses from an amplified Ti:Sapph

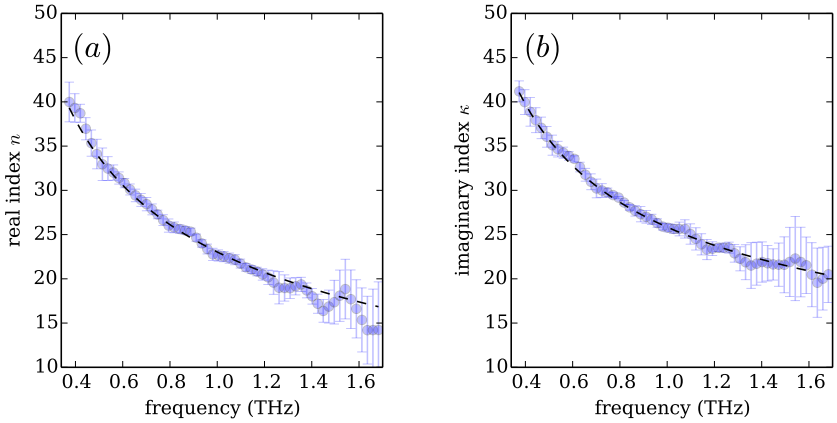

Figure 2.9: Experimental values of n and κ as a function of frequency for the intrinsically As doped Si layer as extracted from experimental data using a T-matrix model (blue circles), and the corresponding least square error fit to the Drude model (black dashed curves). The fitting parameters for the Drude model are $N = 3.6 \times 10^{19}$ cm^{-3} and $\mu_e = 0.012$ m^{2}V^{-1}s^{-1}.

oscillator. Additionally, the mobility of the photo-excited carriers is large enough to induce a metallic behavior.

Sample and fabrication

The sample used for photo-excitation contains a 1 µm thin layer of single-crystalline GaAs which is symmetrically bonded on both sides to a 1 mm amorphous quartz substrate. The fabrication of this sample has been done by Mulder, Bauhuis and Schermer as described in refs. [116, 117]. On top of a standard 2-inch diameter (001) GaAs wafer, a 1 µm thick undoped GaAs layer was grown, using metal organic chemical vapor deposition (MOCVD) separated by a 10 nm thin AlAs sacrificial etch stop layer. In a next step the GaAs thin-film is transferred from the wafer and bonded to a 1 mm thick amorphous quartz substrate using a mercapto-ester based polymer, leaving the 1 µm single crystalline GaAs layer on top of the substrate. As a last step, an amorphous quartz superstrate is bonded to the upper side of the sample, symmetrically embedding the GaAs layer in a higher index environment. The thickness of the bonding layers at both sides of the thin GaAs layer is ~ 40 µm. The schematic representation of this sample is given in figure 2.8, where layers C and E are the ~ 40 µm bonding layers and D the GaAs thin film.

Characterization

This sample is measured in transmission with the THz time-domain spectrometer as illustrated in figure 2.1. In the absence of any photo-excitation the transient is as

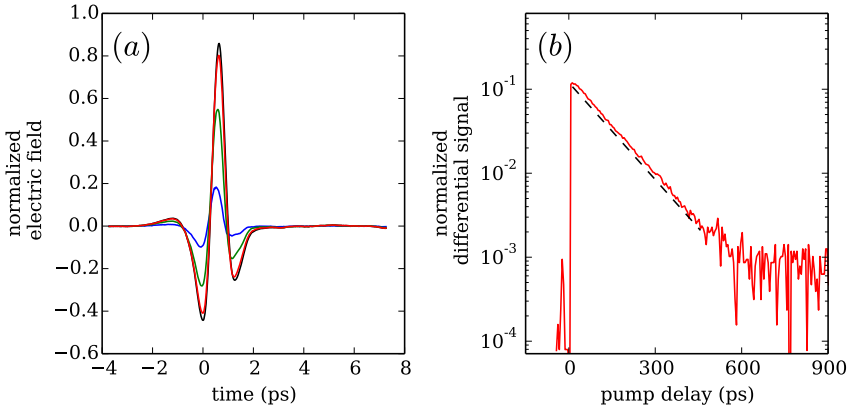

Figure 2.10: Transients (a) and a pump scan (b) for the 1 µm thin GaAs layer symmetrically embedded in amorphous quartz. The transients are for fluencies of 1.4 mJcm^{-2} (red curves), 14 mJcm^{-2} (green curve) and 140 mJcm^{-2} (blue curve) at a pump delay of 100 ps. The solid black curve represents a transient in the absence of optical excitation. The pump scan was taken at the maximum THz position, 0.64 ps, for a fluence of 1.4 mJcm^{-2}. The black dashed line represents an exponential fit to the measurements with an estimated carrier lifetime of 110 ps. For clarity this fit is slightly displaced vertically.

indicated by the black curve in figure 2.10(a). This transient decreases in amplitude when the sample is photo-excited. The colored curves in figure 2.10(a) show transients for fluencies of 1.4 mJcm^{-2} (red curve), 14 mJcm^{-2} (green curve) and 140 mJcm^{-2} (blue curve) and for a fixed delay of $\tau = 100$ ps between the optical pump and the THz probe. The general trend can be explained as follows: A larger fluence creates more electron-hole pairs, which increases the metallic behavior of the GaAs layer. As a result the amplitude of the transmitted THz signal gets reduced.

Figure 2.10(b) shows the dynamic behavior of the photo-excited charge carriers. At the apex of the transient, 0.64 ps in figure 2.10(a), and a fluence of 1.4 mJcm^{-2} the delay between the optical pump and the THz probe is varied. The vertical axis shows the differential signal, which is the difference between the transmitted THz signal through the sample with and without photo-excitation. This differential signal has been acquired by using the chopper in the pump arm as indicated in figure 2.1. For negative pump delays the pump pulse arrives at he sample after the THz pulse, and as a result the differential signal is at the noise level. For $\tau > 0$ the carriers need a short time to thermalize and reach the maximum differential signal, after which they exponentially decay. The black dashed line in the figure is a single exponential fit with a carrier lifetime of 110 ps.

Similar to the analysis for the intrinsically doped Si, the transients of the photo-excited GaAs thin film (figure 2.10(a)) are Fourier transformed and the complex refractive indexes are calculated with the T-matrix method. For the bonding layers

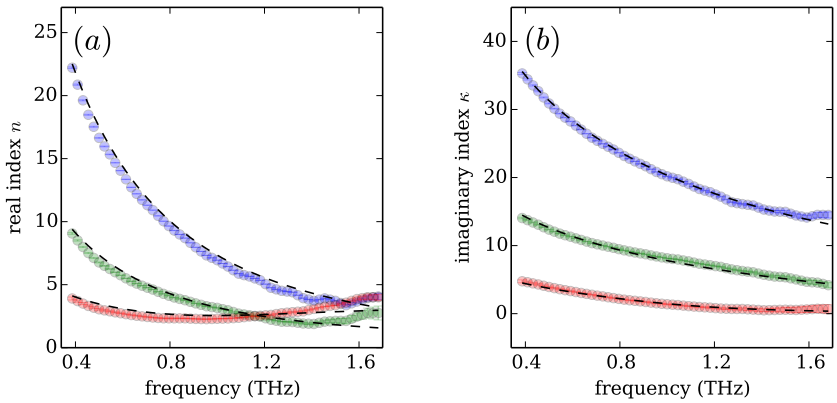

Figure 2.11: Real (a) and imaginary (b) components of the complex refractive index of the photo-excited GaAs thin film for fluencies of 1.4 mJcm^{-2} (red curves), 14 mJcm^{-2} (green curves) and 140 mJcm^{-2} (blue curves) at a pump-probe delay of 100 ps. The values are calculated from experimental data using the T-matrix method as indicated by the circles, while the black dashed curves represent least square error fits to the Drude model.

an index of $\tilde{n} = 1.62 + 0.04i$ is used. The resulting spectra for the complex refractive indexes of the photo-excited GaAs for the different fluences are shown in figure 2.11 and indicated by the circles. The colors match those of the corresponding transients of figure 2.10(a). The curves are highly dispersive, and the index increases as a function of the pump fluence. Using an effective mass for the electrons in GaAs of $m = 0.063m_0$, a least square error fit to the Drude model can be performed. These fits are represented in figure 2.11 by the dashed black curves. The carrier concentrations resulting from these fits are $N = 1.2 \times 10^{16}$ cm^{-3}, $N = 8.0 \times 10^{16}$ cm^{-3} and $N = 4.8 \times 10^{17}$ cm^{-3}. The carrier mobility obtained from the fit is $\mu_e = 0.53 \pm 0.03$ m^{2}V^{-1}s^{-1} and is in agreement with values reported in literature [118].

2.3 Carrier distribution

In the analysis of the photo-excited thin film it is assumed that the carriers are homogeneously distributed over the layer, i.e. independent of the depth. However, the actual distribution will show a depth dependence. Due to absorption of the NIR pulse, the initial profile of the induced carriers is a decaying exponential, which changes over time due to carrier diffusion and both bulk and surface recombination.

As a check of the influence of this distribution on the measurements, a numerical analysis is performed to verify whether or not a standard THz-TDS spectrometer is able to discriminate between different carrier distributions. This is done as follows: The 1 µm GaAs layer is subdivided into 100 sub-layers. The initial carrier con-

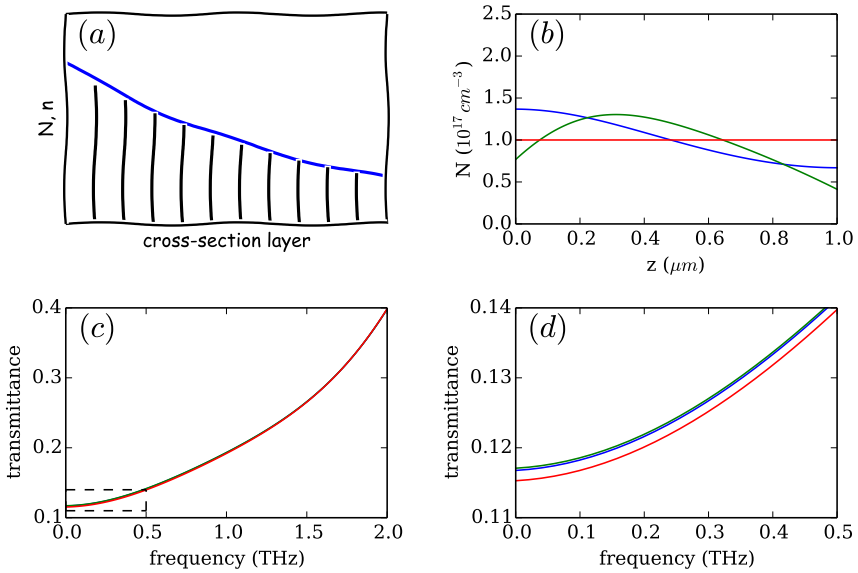

Figure 2.12: (a) Sketch of the subdivision of the GaAs thin film in multiple slices for the T-matrix method. (b) Normalized carrier distributions for a homogeneous distribution (red curves), and distributions with (green curves) and without (blue curves) surface recombination. These distributions correspond to 100 ps after photo-excitation. (c) Transmission calculated with the T-matrix method for a distribution of the carriers as those of panel (b). (d) A zoom of the curves as marked by the dashed lines in panel (c).

centration assigned to each of these sub-layers is given by the decaying exponential $N = N_0 e^{-z/L_{\text{abs}}}$, with $L_{\text{abs}} = 0.8$ µm the absorption length of GaAs at a wavelength of 800 nm. This is illustrated in figure 2.12(a). Subsequently, the carriers are allowed to diffuse and recombine according to the 1D diffusion equation

$$\frac{\partial N}{\partial t} = D\frac{\partial^2 N}{\partial x^2} - \alpha N \ , \tag{2.3}$$

where α is the carrier recombination rate, and $D = 2k_B T\mu/e$ the diffusion constant. The mobility for ambipolar diffusion depends on both the electron and hole mobilities according to $\mu^{-1} = \mu_e^{-1} + \mu_h^{-1}$. However, since $\mu_h << \mu_e$ the holes are dominant in the mobility, which can be approximated as $\mu \approx \mu_h = 0.036\ \text{m}^2\text{V}^{-1}\text{s}^{-1}$. The boundary conditions are determined by the surface recombination velocity σ as

$$\left.\frac{\partial N}{\partial t}\right|_{\text{boundary}} = -\sigma N \ . \tag{2.4}$$

Equation 2.3 is solved numerically, both with and without a surface recombination velocity of $\sigma = 8.5 \times 10^5$ ms^{-1}. The carriers are allowed in both cases to diffuse over a period of 100 ps after the initial photo-excitation. The resulting depth-dependent concentrations of carriers are normalized such that both have an average concentration of carriers of $N = 10^{17}$ cm^{-3}. These distributions are shown in figure 2.12(b), as well as a homogeneous distribution of carriers of $N = 10^{17}$ cm^{-3}. These distributions are used, together with the Drude model to calculate a depth-dependent permittivity, which in turn is used in the T-matrix method to calculate the transmittance spectra. These spectra are shown in figure 2.12(c), with a zoom shown in figure 2.12(d). Although the transmittance spectra differ on details these differences are small, in the order of 10^{-3}. The differences approach the dynamic range of our experimental setups, especially at the lower frequencies, and are therefor too small to resolve experimentally.

2.4 Conclusions

The concept of terahertz time-domain spectroscopy is introduced and the mechanisms of generation and detection of terahertz pulses used in this thesis are discussed. Transmission measurements are analyzed with the T-matrix method for the characterization of substrates and bonding layers. Refractive index spectra for the doped Si and photo-excited GaAs thin films are fitted to the Drude model and show excellent agreement with literature values. Lastly, the influence of the carrier diffusion on the transmittance is studied for photo-excited GaAs and found to approach the resolution of our experimental setups.

Chapter 3

Enhanced extinction of single bowtie antennas using conical waveguides

We demonstrate experimentally the resonant extinction of THz radiation from a single metallic bowtie antenna, formed by two n-doped Si monomers with a triangular shape and facing apexes. This demonstration is achieved by placing the antenna at the output aperture of a conically tapered waveguide, which enhances the intensity of the incident THz field at the antenna position by a factor 10. The waveguide also suppresses the background radiation that otherwise is transmitted without being scattered by the antenna. Bowtie antennas, supporting localized resonances, are relevant due to their ability of resonantly enhancing the field intensity at the gap separating the two triangular elements. This gap has subwavelength dimensions, which allows the concentration of THz radiation beyond the diffraction limit. The combination of a bowtie antenna and a conical waveguide may serve as a platform for far-field THz time-domain spectroscopy of single nanostructures placed in the gap.

This chapter is based on M.C. Schaafsma, H. Starmans, A. Berrier and J. Gómez Rivas, *Enhanced terahertz extinction of single plasmonic antennas with conically tapered waveguides*, New J. Phys. 15, 015006 1-14 (2013).

3.1 Introduction

When the conduction electrons in an antenna are driven around their localized resonance (LR) frequency the local fields in the vicinity of the antenna can be greatly enhanced. Metallic bowtie antennas can locally enhance the field intensity at the LR frequency by several orders of magnitude in the gap between the individual monomers [119]. This gap has typically a volume of $\sim 10^{-6}\lambda^3$. The large intensity enhancement in deep subwavelength volumes opens the possibility for THz spectroscopy of single nanostructures or at very low concentrations of material. However, the scattering and extinction cross sections of such a plasmonic antenna can be still small compared to the beam size of the THz pulse in standard THz-TDS setups. To make the detection of a single antenna possible we use a conically tapered waveguide. Tapered waveguides have been proposed to guide and enhance THz radiation into a confined region [120–122]. Zhang et al. investigated the adiabatic compression of tapered parallel-plate waveguides [123], Zhan et al. showed superfocussing of THz radiation using tapered parallel-plate waveguides [124] and Wächter et al. used photoconductive THz field probes for subwavelength imaging [125]. Enhanced THz transmission through conically tapered waveguides was recently reported by Nguyen et al. [126].

In this chapter we extend the application domain of conically tapered waveguides. We demonstrate that it is possible to detect and measure the extinction of a single bowtie antenna in a standard THz time-domain spectrometer, when placed at the waveguide output where the intensity of the THz field is enhanced. The antenna is formed by two triangular monomers with facing apexes, separated by a 5 µm gap. The monomers are made of intrinsically doped Si, which has a metallic behavior at THz frequencies [127]. The investigated antenna exhibits a localized resonance at around 0.35 THz when excited by a plane wave polarized along its long axis. This resonance is the result of the coherent oscillation of the free charge carriers, harmonically driven by the incident THz electric field.

This chapter is organized as follows: The design of the experiments and the fabrication of the waveguides and bowtie antenna are described in section 3.2. Section 3.3 shows results of simulations of the near field intensity enhancement of single bowtie antennas and the conical waveguide, as well as the enhanced intensity transmission of the latter. The experimental characterization of the waveguides, and extinction measurements of single THz antennas at the output of the conical waveguide are compared with the extinction of a random array of similar antennas in section 3.4. These measurements demonstrate the enhanced extinction of single antennas mediated by the enhanced intensity at the output of the waveguide. The chapter is ended with the conclusions.

3.2 Design of experiments and fabrication

Figure 3.1 illustrates the mechanism for combining the single bowtie antenna with a conically tapered waveguide. A standard experiment conducted on a single antenna

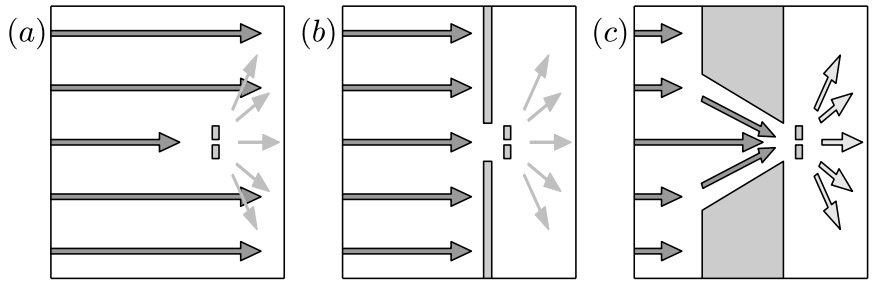

Figure 3.1: Schematic representation of experiments conducted on a single antenna. (a) A bow-tie antenna with a small cross section is illuminated by a spatially extended beam. Only a small fraction of the field is scattered and absorbed by the antenna. In a transmission experiment, there is a large background of unscattered radiation. (b) A cylindrical waveguide or a metallic screen will block this background. However, the scattered intensity is still low. (c) The enhancement of this intensity is possible by concentrating the incident field on the antenna with a conically tapered waveguide.

is shown in figure 3.1(a), where a linearly polarized THz beam is used to illuminate a single bowtie antenna. Since the antenna has an extinction cross section much smaller than the size of the beam, only a small fraction of the incident field is extinct by scattering and absorption in the antenna. The majority of the field is transmitted as unperturbed by the antenna, leading to a large background in the measurements. In order to reduce this background, a thin metallic screen can be used to only transmit the relevant part of the THz beam that interacts with the antenna (figure 3.1(b)). Although the signal-to-background ratio is improved in this configuration, only a small fraction of the incident beam is used and the signal-to-noise is not increased. This signal-to-noise is increased when the cylindrical waveguide is replaced by a tapered waveguide (figure 3.1(c)). The conical design guides the off-center parts of the field towards the antenna, resulting in an enhanced THz electromagnetic intensity at the waveguide's output aperture. This intensity enhancement leads also to the enhanced response of the antenna, allowing a more sensitive spectroscopy.

Two waveguides have been fabricated for the experiments. A conical shape waveguide is used to enhance the field at its output aperture and a cylindrical waveguide with the same output dimensions is used to reference the transmittance. The waveguides have been fabricated using electrical discharge machining: A conically tapered electrode with a half-angle of 15^o is lowered through an aluminum plate of 1 cm thickness, eroding a conical hole. The electrode is lowered until the exit aperture has a diameter of 0.6 mm, leaving an input aperture of 6 mm. A schematic representation of the conical waveguide is shown in figure 3.2(a). A cylindrical waveguide is obtained by lowering an electrode with a diameter of 0.6 mm through a 0.5 mm thick aluminum sheet. These dimensions are chosen such that the intensity enhancement produced by the conically tapered waveguide at its exit aperture is maximum in the frequency

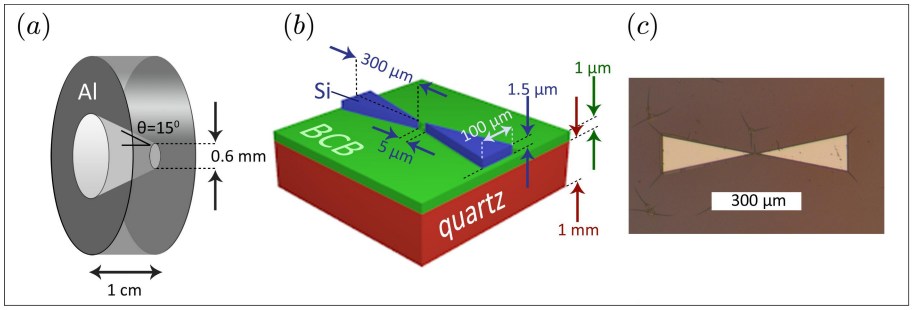

Figure 3.2: Schematic representation of the conical waveguide (a) and the bowtie antenna (b). Optical microscope image of the bowtie antenna (c). The antenna is formed by two triangular monomers of n-doped Si, bonded onto an amorphous quartz substrate with BCB. The cracks in the microscope image are in the supporting BCB layer.

range of the localized resonance of the bowtie antennas.

The semiconductor bowtie antennas have been fabricated using the conventional micro-fabrication techniques described in chapter 2. The Si layer has a thickness of 1.5 µm, and is implanted with arsenic atoms introducing a free carrier concentration of $(6\pm3)\times10^{19}$ cm^{-3}. After the thin layer has been transfered to an amorphous quartz substrate, the antenna structures are defined using optical lithography and reactive ion etching. The bowtie antenna is formed by two monomers with a triangular shape with a base of 100 µm, a triangle height of 300 µm. The triangles have facing apexes, separated by a gap of 5 µm. This structure has a LR around 0.35 THz. A schematic representation of the bowtie antenna and an optical microscope image are shown in figures 3.2(b) and 3.2(c), respectively. The small cracks observed in the image are cracks in the benzocyclobutene (BCB) bonding layer. These cracks have a typical width of a micron, which is much smaller than the wavelength of THz radiation, and do not influence the measurements.

3.3 Simulations

Bowtie antenna

The local field enhancement of the bowtie antenna and the transmission properties of the conical waveguide are studied using a 3D finite element method (FEM) in the frequency domain (COMSOL Multiphysics). For the simulations we use the antenna dimensions determined from the optical image (figure 3.2(c)). The dielectric properties of the n-doped Si are approximated with the Drude model as described in chapter 1, with a free charge carrier concentration of 6×10^{19} cm^{-3}, and an electron mobility of 58 cm^{2}V^{-1}s^{-1} [128]. The resulting plasma frequency is around 70 THz. For simplicity, we ignore the presence of the substrate in the simulations, assuming that the antenna is homogeneously surrounded by air. Although this simplification

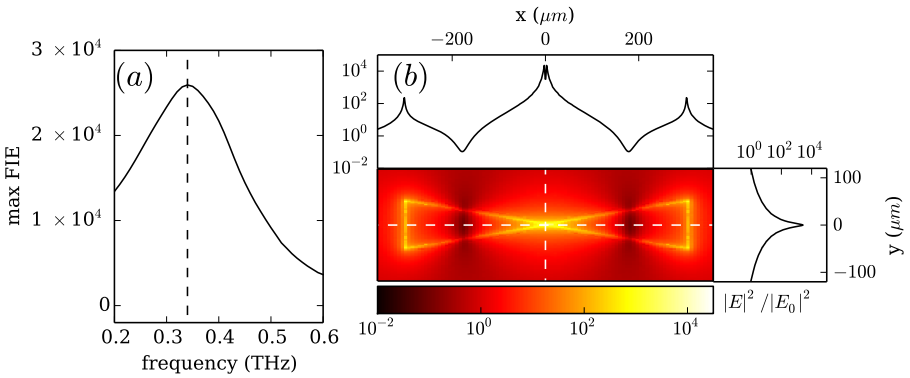

Figure 3.3: 3D Finite Element Method simulations of the local field intensity enhancement (FIE) of a doped silicon bowtie antenna. The antenna is illuminated at normal incidence, i.e., the incident wave vector is normal to the plane of the figure. The incident THz wave is polarized parallel to the **long axis** of the antenna, and the antenna dimensions are as discussed in the text. (a) shows the spectrum of the maximum FIE in the gap between the monomers, the vertical dashed line indicates the LR frequency. (b) shows the FIE in the plane at the middle height of the antenna axis at the LR frequency. The black curves are cuts along the white dashed lines.

might introduce a shift in the LR frequency, the underlying physical mechanism will not change.

The property which is calculated from the simulations is the field intensity enhancement (FIE). This is the ratio between the intensities of the simulated fields with and without antenna structure. Since the geometry of the bowtie antenna is highly anisotropic, there will be a strong dependence of this FIE on the polarization of the incident radiation. The results of the FIE calculation for a polarization along the long axis is shown in figure 3.3, while figure 3.4 shows the FIE for a polarization along the short axis of the antenna. Figures (a) show the maximum FIE along either cardinal axis as a function of frequency, while figures (b) show the spatial distribution of the FIE for a single frequency in the plane at the middle height of the antennas. This frequency is the LR frequency of the long axis of the antenna at 0.34 THz, and is indicated in figures 3.3(a) and 3.4(a) by the vertical dashed lines.

When driven along the long axis, the free electrons in the semiconductor bowtie antenna resonate around the LR frequency. Additionally, there is a capacitive coupling of the two monomers across the gap. This coupling, arising from the coulomb attraction of charges across the short distance separating the two monomers, gives rise to an intensity enhancement in the gap. The enhancement is further increased by the lighting-rod effect that results from the sharp tips forming the apex of the triangles. The simulations show in figure 3.3 an intensity enhancement in the gap over 4 orders

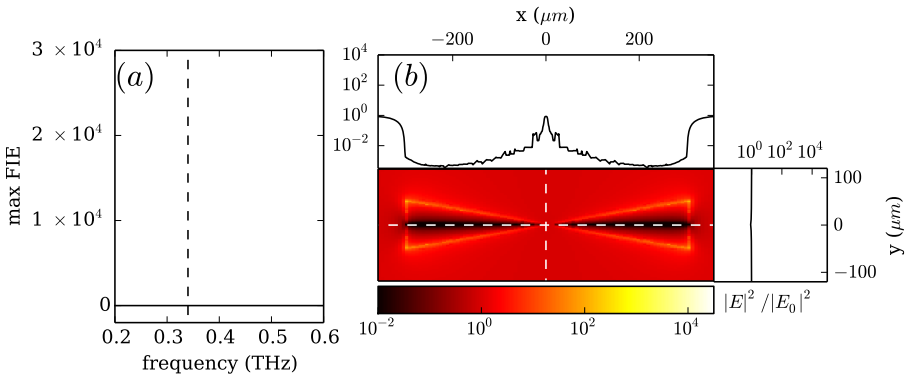

Figure 3.4: 3D Finite Element Method simulations of the local field intensity enhancement (FIE) of a doped silicon bowtie antenna, with the incident THz radiation polarized parallel to the **short axis** of the antenna. (a) shows the spectrum of the maximum FIE in the gap between the monomers, (b) shows the FIE in the plane at the middle height of the antenna axis at the LR frequency.

of magnitude under LR conditions. This maximum is reached at the apexes of the monomers defining the gap. Inside the semiconductor the FIE does not drop to zero as a result of the finite skin-depth of the material. At certain locations outside the semiconductor antenna, strong suppressions in the intensity can be observed. The origin of the reduced intensity is due to destructive interference between the incident field and the field scattered by the antenna. For an incident polarization along the short axis of the antenna there is no maximum field enhancement in the vicinity of the gap which significantly exceeds unity, and the spectrum of figure 3.4(a) is flat. The FIE at the LR frequency (figure 3.4(b)) shows some variation with position, but this is mostly a reduction of the intensity inside the semiconductor. Outside the semiconductor the FEI is insignificant. The curve representing the FIE along the long axis of the antenna diplays a steplike nature. This is a result of the finite resolution of the meshing of the simulation volume. Note that the enhancements described above might be different in a real sample due to rounding of the antenna tips and the presence of the substrate. Nevertheless, the simulations illustrate that resonant bowtie antennas are capable of focusing and enhancing locally electromagnetic fields in subwavelength volumes.

Waveguide

The transmission properties of the conically tapered and cylindrical waveguides are simulated using FEM and the finite-difference in time domain (FDTD, CST Microwave Studio) method. As sketched in figure 3.1, a linearly polarized plane wave

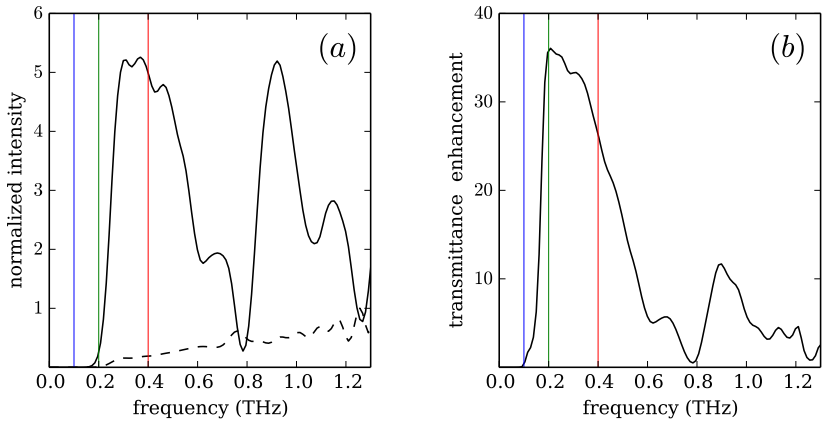

Figure 3.5: (a) Simulated intensity spectra of a conically tapered (solid) and cylindrical (dashed) waveguide at a distance of 1 mm after the output aperture, normalized to the incident intensity. (b) Transmitted intensity of the conically tapered waveguide referenced by the cylindrical waveguide. The vertical lines in both figures correspond to the frequencies at which the intensity enhancements are shown in figure 3.6.

travels from left to right through the system. The dimensions of the waveguides used for the simulations are those described in section 3.2, i.e., both waveguides having an output aperture of 0.6 mm diameter, and the conically tapered waveguide having an input aperture of 6.0 mm in diameter. The aluminum forming the waveguides is simulated as a perfect electric conductor (PEC). For the FDTD simulations a broadband Gaussian pulse is sent through the system, and the intensity of the transmitted field is monitored behind the waveguide. The simulated time domain signals are Fourier transformed and squared, resulting in the power spectrum of transmitted intensities.

Figure 3.5(a) shows the intensity spectrum, defined as the intensity at 1.0 mm after the waveguide, normalized by the intensity incident on the waveguide. It is important to note that the normalized intensity is strongly dependent on the distance to the output aperture. At short distances, evanescent field components will give larger field intensities whereas as the distance is increased the intensity decreases roughly with the inverse of the square of the distance due to diffraction. The spectrum of the conically tapered waveguide is indicated with the black-solid curve, and the cylindrical waveguide with the black-dashed curve. At low frequencies the transmittance vanishes. These frequencies are below the cutoff frequency defined by the output aperture of the waveguides. For an infinitely long cylindrical waveguide with a diameter of 0.6 mm the cutoff frequency is 0.3 THz [129].

Figure 3.5(b) shows the intensity transmittance enhancement, which is defined as the transmittance through the conically tapered waveguide normalized by the transmittance through the cylindrical waveguide. The conically tapered waveguide

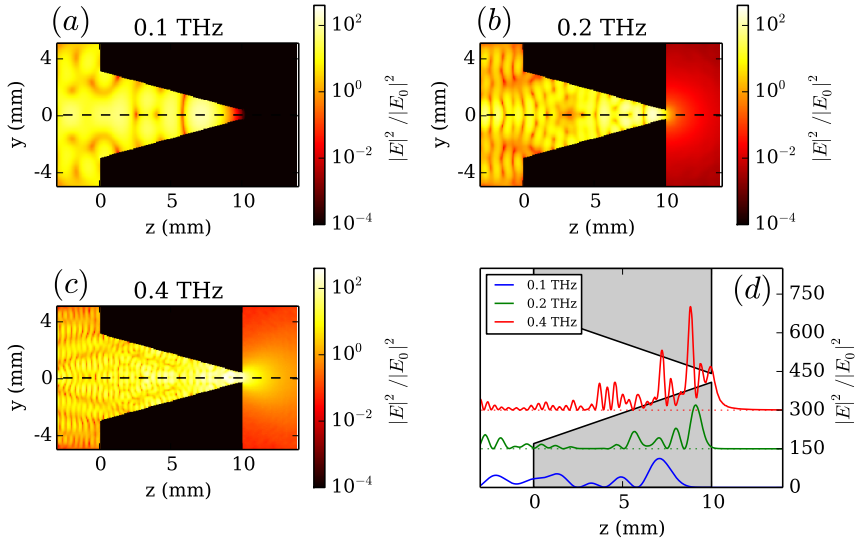

Figure 3.6: 3D FEM simulations of the intensity enhancement of the THz electromagnetic field propagating through a conically tapered waveguide at various frequencies. A linear y-polarized plane wave enters the waveguide from the left and travels to the right. 2D cuts through the center of the waveguide are shown for frequencies of 0.1 THz (a), 0.2 THz (b) and 0.4 THz (c). These frequencies correspond to frequencies below, around and above the cutoff frequency of the waveguide, respectively. Line cuts of the total field intensity enhancement through the center of the waveguide along the direction of propagation of the wave are shown in (d). For clarity, the field intensities at 0.2 THz and 0.4 THz have been vertically displaced.

enhances the transmitted field intensity, while the cylindrical waveguide only transmits a fraction of the intensity incident onto the opening, reflecting the rest. The conically tapered waveguide guides the incident field at the larger input aperture towards the smaller output aperture. These fields travel a longer distance, picking up an additional phase compared to the direct transmitted fields. For the given waveguide dimensions this results in destructive interference and a minimum in the transmitted intensity around 0.8 THz. For a perfect adiabatic transmission through a tapered waveguide, the field intensity enhancement at the output aperture is given by the ratio of the input to output aperture cross sections. This ratio is 100 for the conically tapered waveguide used here. However, the transmission is not adiabatic due to a large tapering angle and the field experiences reflections as it propagates through the waveguide. Therefore, the simulated intensity enhancement of the conically tapered waveguide over the cylindrical waveguide reaches a magnitude of around 35.

Figure 3.6 shows FEM simulations for the total field intensity enhancement in the conically tapered waveguide. A monochromatic and linearly y-polarized plane wave propagates from left to right. The total intensity enhancement in the plane through

the center of the waveguide along the polarization direction -the yz plane- is shown for frequencies below, around and above cutoff in figures 3.6(a)-(c), respectively. Cuts through these maps along the dashed white lines are shown in figure 3.6(d). For frequencies below cutoff there is an enhancement of the field inside the waveguide, but the transmitted intensity is reduced because the propagating field is fully reflected before the output aperture is reached. The interference pattern in the intensity enhancement is the result of the interference of the incident field and this reflection. For waves having frequencies close to the cutoff frequency, there is a transition from the evanescent transmitted field to propagating waves. Figure 3.6(b) shows that although most of the wave is reflected a small fraction is transmitted. For frequencies well above cutoff, as in figure 3.6(c), the field propagates through the waveguide. This condition is needed for a maximum enhancement of the transmission. We note that even for this frequency, significant reflection takes place and the interference pattern is formed. This reflection can be minimized by reducing the tapering angle of the waveguide in order to allow an adiabatic focusing of the incident THz field onto the output aperture [120].

3.4 Experimental results

Experimental setup

The experimental setup for the THz transmission experiments is based on the standard THz-TDS setup as described in section 2.1 of this thesis, with an adjustment to the detection mechanism. A 70 MHz train of 20 fs near-infrared (NIR) pulses with a wavelength centered around 800 nm is split into two arms using a beam splitter. One pulse is used to generate a broadband and linearly polarized THz pulse in a GaAs photoconductive antenna, the other pulse is used to probe this THz pulse in a ZnTe crystal utilizing the electro-optic effect. Using a knife-edge technique the spatial profile of the cross section of the focused THz beam has been verified as Gaussian, with a full width at half maximum of 1.7 mm.

The modification of the detection arm is illustrated in figure 3.7. Any collimated THz beam that has traveled through the conically tapered waveguide becomes highly divergent. In order to assure that a sufficient amount of THz amplitude is detected, the waveguide is placed close to the ZnTe crystal. Since one of the sides of the ZnTe crystal is now obstructed by the waveguide, the probe pulse is coupled from the backside, reflecting on the front face of the ZnTe crystal after which it can probe the THz electric field. This reflection is directed to the detector for analysis.

Waveguide characterization

The experimental characterization of the conically tapered and cylindrical waveguides is shown in figure 3.8. Both waveguides are measured in transmission and compared against each other and a free space reference measurement taken without any waveguide, i.e., the response function of the setup. The time domain transients

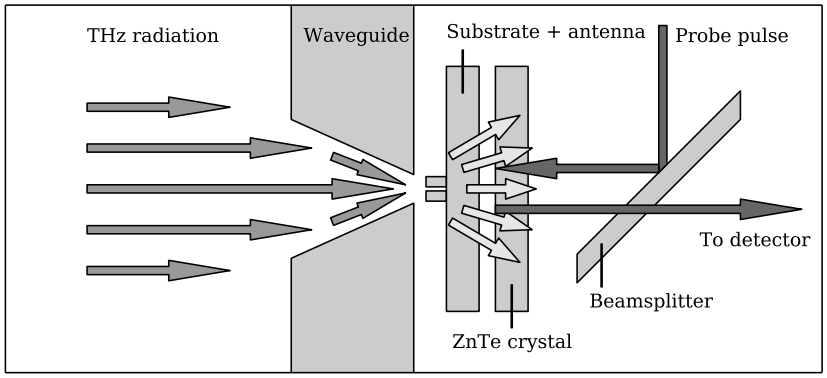

Figure 3.7: Schematic illustration of the experimental setup for detecting a single bowtie antenna. The waveguide is placed in the focus of the THz beam, in front of the ZnTe crystal. The substrate with the antenna is placed in direct contact with the waveguide. The THz radiation travels through the waveguide, passes the antenna and substrate, and propagates through the ZnTe crystal. From the opposite direction the IR probe pulse reflects on the left face of the ZnTe crystal, after which it co-propagates with the THz electric field and is directed to the detector. The illustration is not to scale.

(figure 3.8(a)) show that the presence of the cylindrical waveguide severely reduces the transmitted signal, since most of the incident amplitude is blocked by the waveguide. The enhanced amplitude transmission of the conically tapered waveguide, relative to the cylindrical waveguide, is visible in the time domain as an increased duration of the pulse. This is the contribution of the field that illuminated the entrance of the waveguide at a larger radius, and needed more time to reach the output aperture.

The intensity spectra shown in figure 3.8(b) are the square of the Fourier transform of the time domain transients. The intensity is normalized to the maximum of the setup response. For the empty setup (dotted curve) the maximum signal-to-noise spans 5 orders of magnitude. Both the conical (solid curve) and cylindrical (dashed curve) waveguides reduce the bandwidth of the transmitted intensity to about 2 THz. The enhancement of the conical waveguide over the cylindrical waveguide is clearly visible in the range 0.3 THz-0.8 THz. The intensity transmittance spectra for the conically tapered (solid curve) and cylindrical (dashed curve) waveguides in figure 3.8(c) are obtained by normalizing the spectra shown in figure 3.8(b) against the setup response, i.e., the intensity spectrum measured without any waveguide.

For both waveguides the transmittance vanishes at the lowest frequencies due to cutoff. The transmittance remains below 0.05 for the cylindrical waveguide even at higher frequencies. This reduced intensity transmittance is due to the large area of the incident beam that is blocked. In this experiment, roughly 95 % of the energy carried by the THz beam is contained in an area of 8 mm^2, while the area

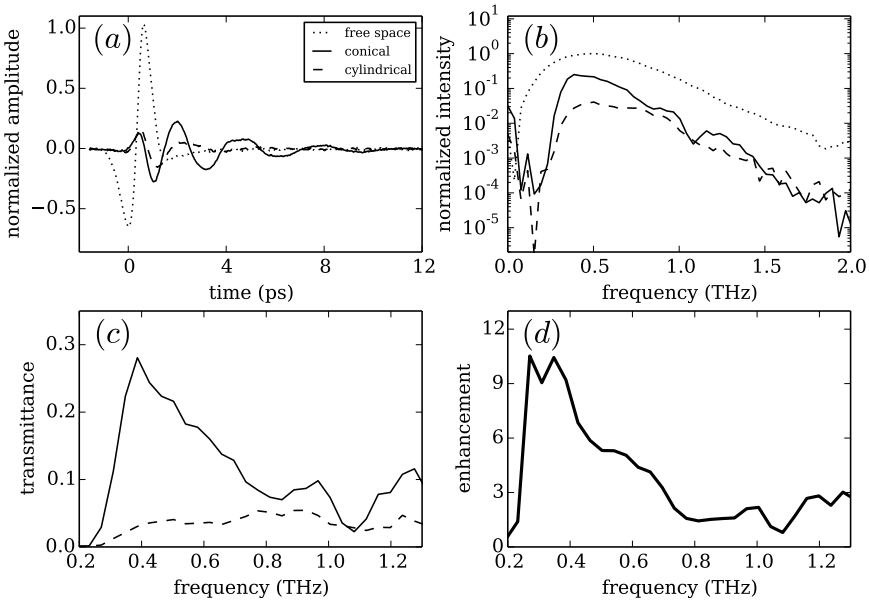

Figure 3.8: Experimental characterization of the conically tapered and cylindrical waveguides. (a) Time domain transmission measurements of the reference (dotted curves), conically tapered (solid curves) and cylindrical (dashed curves) waveguide. (b) Intensity spectra of the time domain signals shown in (a). (c) Transmitted intensity spectra of the conically tapered (solid curves) and cylindrical (dashed curves) waveguides normalized by the free space reference. (d) Transmittance enhancement of the conically tapered waveguide, defined as the transmittance through this waveguide normalized by the transmittance through the cylindrical waveguide.

of the aperture of the cylindrical waveguide is 0.3 mm^2. This ratio of 1/25 matches the experimental results. The transmittance is enhanced for the conical waveguide, compared to the cylindrical one. The same spectral dependency of the simulated intensity of figure 3.5(a) is observed in the transmittance spectra shown in figure 3.8(c), with a maximum in the intensity and transmittance of the conical waveguide at 0.4 THz. The transmittance approaches 0.3 at 0.4 THz, while the output aperture only encloses around 5 % of the area of the incident pulse. Note that the simulations in figure 3.5(a) refer to the intensity at the output aperture normalized to the incident intensity in an equivalent area at the input aperture of the waveguide, while the transmittance of figure 3.8(c) represents the total intensity incident onto the input aperture being transmitted through the waveguide. Therefore, the vertical scales of figure 3.5(a) and figure 3.8(c) should not be directly compared.

The reduced intensity transmittance around 1.0 THz is also consistent with the

simulations, and can be explained by the aforementioned destructive interference in the wavefront. The blue shift of this minimum in the measurements, compared to the simulations, can be attributed to the approximation of plane wave illumination used for the simulations. In the simulations, the full input aperture is illuminated by a plane wave, whereas in the experiments the pulse has a Gaussian profile and it is slightly smaller in diameter than the input aperture of the waveguide. This smaller size of the beam reduces the effective height of the waveguide and introduces a blueshift of the interference features. Figure 3.8(d) displays the intensity transmittance of the conically tapered waveguide normalized by the cylindrical waveguide, showing the enhancement of the transmittance of the conically tapered waveguide over the full range of 0.2 THz-1.3 THz. The maximum intensity enhancement is around one order of magnitude at 0.4 THz. As the cylindrical waveguide should not enhance the intensity, the enhancement of the conical waveguide should be the same when compared to the incident field.

Measurements single antenna

A single bowtie antenna is placed directly at the output aperture of the conically tapered waveguide, as shown in the inset of figure 3.9(a). The measured extinction, which is defined as 1 minus the intensity transmittance, of this single antenna in front of the waveguide is shown in figure 3.9(a) with the solid curve. The transmission measurements through the single antenna are referenced to the transmission of the waveguide with an empty amorphous quartz substrate at the output entrance, i.e. without the antenna. A resonance is clearly resolved in this measurement with a maximum extinction of 90 % around 0.35 THz. This enhanced extinction corresponds to the excitation of a LR in the antenna, which should lead to a large local field enhancement in the bowtie gap. The dotted curve in figure 3.9(a) corresponds to the extinction of the single antenna measured without the waveguide. The response is practically flat and the LR cannot be resolved, since the extinction is below the noise level.

To rule out any possible artifact in the measurements that could lead to an extinction peak similar to our measurements, we have confirmed the resonant response of the bowtie antenna by measuring the extinction of a random array of similar antennas without the conically tapered waveguide. An optical microscope image of the sample is shown in the inset of figure 3.9(b). In this measurement, the THz beam illuminates approximately 30 antennas. Therefore, the extinction is enhanced in this sample by increasing the density of antennas, rather than by concentrating the THz beam with the conical waveguide. A similar extinction spectrum to the single antenna is measured for the random array (figure 3.9(b)). Similar to the spectrum of the single antenna, the extinction reaches a maximum at 0.35 THz, with a resonant response that can be attributed to the excitation of LR.

Surprisingly there is an excellent agreement between the resonant frequency measured in extinction of the bowtie antennas on a quartz substrate and the simulated frequency of maximum FIE in the gap of the antenna homogeneously surrounded

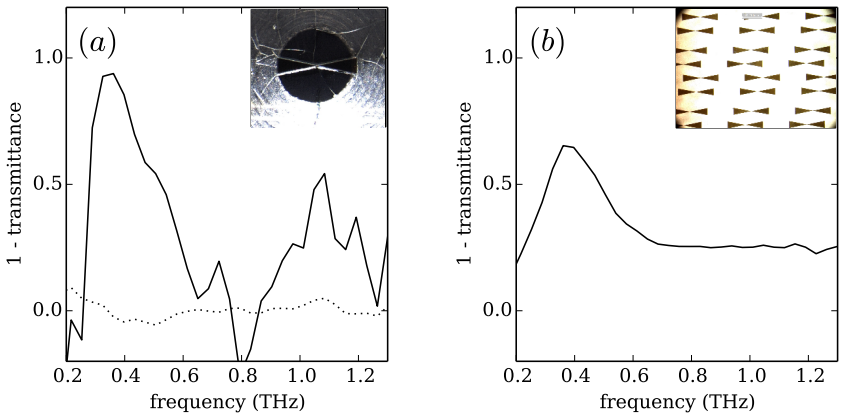

Figure 3.9: Extinction measurements of bowtie antennas, illuminated with a polarization along the long axis and referenced against an empty amorphous quartz substrate. (a) The extinction spectra of a single bowtie antenna measured with the conically tapered waveguide (solid curve) and without any waveguide (dotted curve). In the inset an optical microscope image of the antenna mounted in front of the conically tapered waveguide is shown. (b) The extinction of a random array of close packed antennas, the inset contains an optical microscope image of the array.

by air. In principle one should expect a shift of the resonance frequency due to the presence of the substrate. The reason why we do not see this shift might be attributed to the fact that the simulations refer to the near field and that the measurements probe the far field extinction [130]. Another reason might be deviations of the geometry of the real sample from the simulated structure due to e.g., rounded tips/corners and underetching of the substrate.

Since the antennas have strong polarization dependent scattering properties, experiments were carried out as well for the antennas rotated by 90^o, aligning the polarization of the incident field along the short axis of the antenna. These results are shown in figure 3.10. The spectrum for the antenna with the waveguide does not show any resonance since the LR cannot be excited. This is in agreement with the simulations shown in figure 3.4. All features in the spectra are a result of noise. The spectrum of the random array shown in figure 3.10(b) has a finite extinction at higher frequencies, but shows no sign of a LR, as expected.

The demonstration of the enhanced extinction by a single bowtie antenna opens a range of possibilities for THz spectroscopy of nanostructures or of molecules at low concentrations. For example, the positioning of a nanostructure in the subwavelength gap defined by the two monomers, in which the field is locally enhanced, will enable to increase the THz field-matter interaction to a level at which far-field spectroscopy of single nanostructures at THz frequencies might be possible.

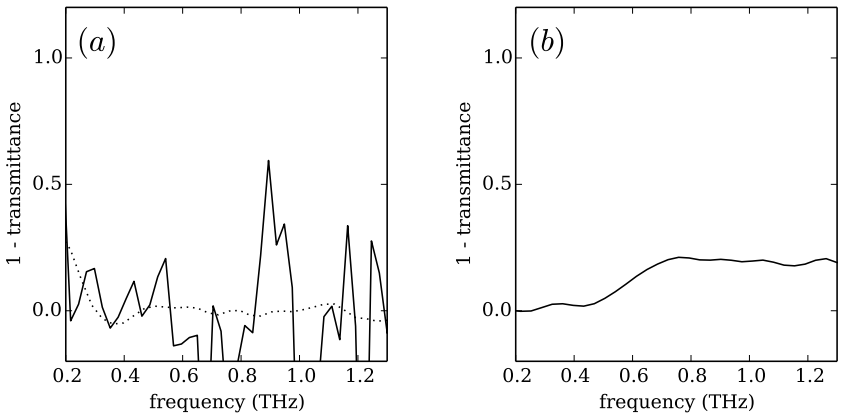

Figure 3.10: Extinction measurements of bowtie antennas, illuminated with a polarization along the short axis and referenced against an empty amorphous quartz substrate. (a) The extinction spectra of a single bowtie antenna measured with the conically tapered waveguide (solid curve) and without any waveguide (dotted curve). (b) The extinction of a random array of close packed antennas.

3.5 Conclusions

In this chapter, we have experimentally demonstrated that a conically tapered waveguide can be used to funnel and enhance the THz intensity. This intensity enhancement allows the detection of the extinction of a single THz bowtie antenna, which otherwise drowns in the large background of unscattered radiation. The transmittance properties are also investigated numerically finding an excellent agreement with the measurements. The large localized field enhancements that can be achieved by bowtie antennas in subwavelength volumes, may open the possibility of using standard far-field THz time domain spectrometers for the detection and spectroscopy of single nanostructures.

Chapter 4

Enhanced extinction in chains of dipoles

We investigate theoretically the enhanced THz extinction by periodic arrays of semiconductor particles. Scattering particles of doped semiconductors can support localized resonances, which can be diffractively coupled giving rise to surface lattice resonances. These resonances are characterized by a large extinction and narrow bandwidth, which can be tuned by controlling the charge carrier concentration in the semiconductor. The underlaying mechanism leading to this tuneability is explained using the coupled dipole approximation and considering GaAs as the semiconductor. The enhanced THz extinction in arrays of GaAs particles could be tuned in a wide range by optical pumping of charge carriers.

This chapter is based on M.C. Schaafsma and J. Gómez Rivas, *Semiconductor plasmonic crystals: active control of THz extinction*, Semicond. Sci. Technol. 28, 124003 1-7 (2013).

4.1 Introduction

Doped semiconductors have a metallic behavior at THz frequencies, which enables the excitation of surface plasmon polaritons (SPPs). The characteristics of the SPPs can be tuned by controlling the carrier concentration in the semiconductor, which can be achieved by doping [103] or, actively, with magnetic fields [131, 132], or by thermal- [96–98], photo-excitation [41, 99–102] or electrical injection of charge carriers [98]. Arrays of metallic particles exhibit very narrow bands with extraordinary extinction [71, 72, 133]. These bands, known as surface lattice resonances (SLRs) are the result of the enhanced radiative coupling of localized resonances (LRs) through Rayleigh anomalies (diffracted orders in the plane of the array) [70]. SLRs have been mostly investigated at optical and near IR frequencies [74–76, 79, 134, 135]. The few works on diffractive coupling of LRs at THz frequencies have been done on metallic structures [136–139], with the exception of ref. [140] where arrays of Si resonators have been considered. However, in that reference no connection with SLRs was made.

In this chapter we investigate theoretically the properties of SLRs in 1D arrays of GaAs particles at THz frequencies. GaAs is a high mobility semiconductor with a bandgap that allows for absorption of near IR wavelengths. Absorbed photons can excite free charge carriers in the semiconductor, which results in a metallic behavior at THz frequencies. The localized resonances in semiconductor particles depend on the concentration of charge carriers. Since SLRs in an ensemble of scatterers depend in turn on the individual LRs, control over the concentration of charge carriers will result in a control of the SLRs. The sharp resonances in SLRs and the tuneability of the material properties in semiconductors are interesting for THz modulation. The control of the material properties in semiconductors is an advantage over most metals, which cannot be actively tuned since they behave as nearly perfect electric conductors at THz frequencies. The chapter is organized as follows: Using the Drude model as introduced in chapter 1 the localized resonances in GaAs ellipsoids are described in section 4.2 as a function of both carrier concentration in the GaAs and the shape of the ellipsoid. The coupled dipole approximation for an ensemble of scatterers is described in section 4.3, after which the active control of the extinction in arrays of GaAs scatterers is discussed. In section 4.4 the mechanism of diffractive coupling is explained in further detail by representing the relevant field components in the complex plane as calculated with the coupled dipole model. The chapter is ended with conclusions.

4.2 GaAs localized resonances

As introduced in the first chapter of this thesis, the extinction cross section C_{ext} of an isolated scattering particle is determined by its polarizability tensor α

$$C_{\text{ext}} = 4\pi k \,\text{Im}(\alpha_{\text{m}}) \,, \tag{4.1}$$

for light polarized along the axis m of the particle. This polarizability tensor depends on the shape and size of the particle, and the permittivity of the materials forming the

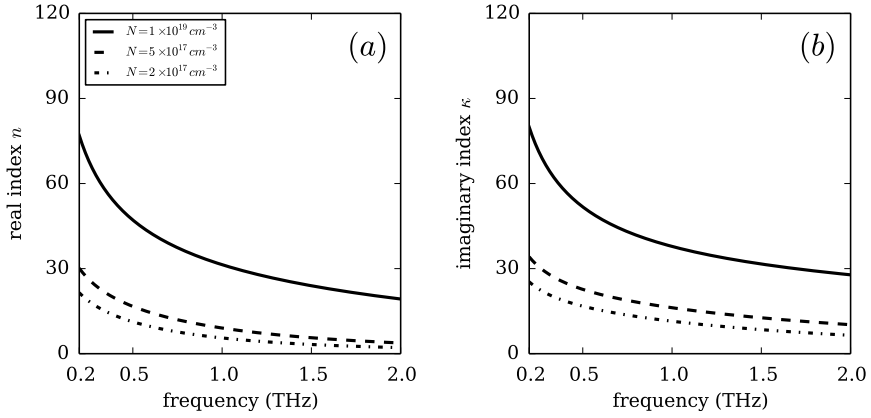

Figure 4.1: Real (a) and imaginary (b) components of the refractive index of GaAs for various carrier concentrations, as calculated with the Drude model of free charge carriers

particle and its surrounding. For scatterers of finite size, both dynamic depolarization and radiative damping dominate the spectral dependency of the polarizability. In the modified long wavelength approximation (MLWA), which holds for particles of subwavelength dimensions, the polarizability is given by [46]

$$\alpha_m = \frac{\alpha_m^{\text{static}}}{1 - \frac{2}{3}ik^3\alpha_m^{\text{static}} - \frac{2k^2}{d_m}\alpha_m^{\text{static}}} \,, \tag{4.2}$$

where the static polarizibility is given by

$$\alpha_m^{\text{static}} = V\frac{(\epsilon_p - \epsilon_s)}{(3(\epsilon_p - \epsilon_s)\cdot L_m + 3\epsilon_s)} \,. \tag{4.3}$$

where $m = 1, 2, 3$ represent the principal axes of the ellipsoid with corresponding diameters d_m, and V the volume of the particle. The permittivities of the particle and of the surrounding dielectric medium are ϵ_p and ϵ_s respectively, and L_m is the shape factor taking account for the flattening of the particle. This factor consists out of an integral and is given by equation (1.16).

The refractive index of GaAs is dispersive, and depends on the concentration of charge carriers. As mentioned in section 2.2 its optical properties can be described with a Drude model. Figure 4.1 shows the real and imaginary part of the GaAs complex refractive index as calculated with the Drude model for various carrier concentrations, namely, 2×10^{17} cm^{-3} (dash-dotted curves), 5×10^{17} cm^{-3} (dashed curves), and 10^{19} cm^{-3} (solid curves). Changes in the carrier concentration of the order of 10^{19} cm^{-3} can be reached by photo-excitation [114]. Increasing the carrier concentration increases the plasma frequency, giving to the material a more metallic

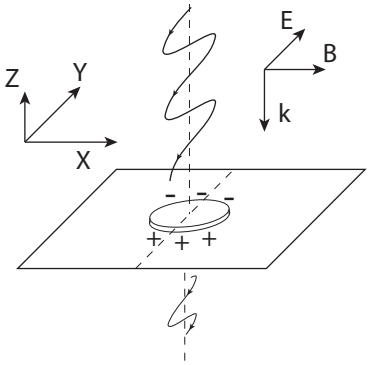

Figure 4.2: Schematic representation of the ellipsoidal particle geometry and illumination.

behavior, i.e. the magnitude of the real component of the permittivity increases, but also increases the imaginary component associated with the Ohmic losses in the semiconductor.

Calculations of the extinction cross section of GaAs micro-ellipsoids with two identical long axes of varying lengths and a short axis of 1.5 µm, are shown in figure 4.3. This height is chosen such that the structures can be made by thin film deposition and optical lithography [114]. The incident electromagnetic field is chosen such that the wave vector is parallel with the short axis of the ellipsoid along the z-axis, and a polarization in the y-direction. A scheme of the geometry is shown in figure 4.2. The extinction cross section is normalized against the geometrical cross section of the respective ellipsoids, resulting in the extinction efficiency Q_{ext}. The GaAs particles are considered to be surrounded by a lossless material with $\epsilon_s = 4$, or $n = 2$. This corresponds to quartz at THz frequencies. The extinction spectra are calculated for diameters of 50 µm (a), 60 µm (b), 70 µm (c) and 80 µm (d), and by varying the carrier concentration in GaAs in the range 2×10^{17} cm^{-3} to 10^{19} cm^{-3} (different curves in figure 4.3). All the spectra show a resonant behavior that corresponds to the coherent and resonant oscillation of the charge carriers in the particle, i.e. the LRs in conducting GaAs.

The resonant frequency and the spectral width of the LRs are shown in figure 4.4, as a function of the disk diameter and carrier concentration. Due to the asymmetric shape of the LR and in order to have a clear comparison with the spectra discussed in the next section, we define the resonance width at the lower frequency half width at half maximum (HWHM). Increasing the particle diameter gives rise to a pronounced redshift of the LR (figure 4.4(a)). This redshift can be qualitatively described by the decrease in the oscillator restoring force of the charge density as the distance between charges of different sign increases. Increasing the carrier concentration increases the plasma frequency ω_p and blueshifts the resonant extinction spectrum as a consequence of the increased oscillator restoring force. We can also see that the HWHM is reduced

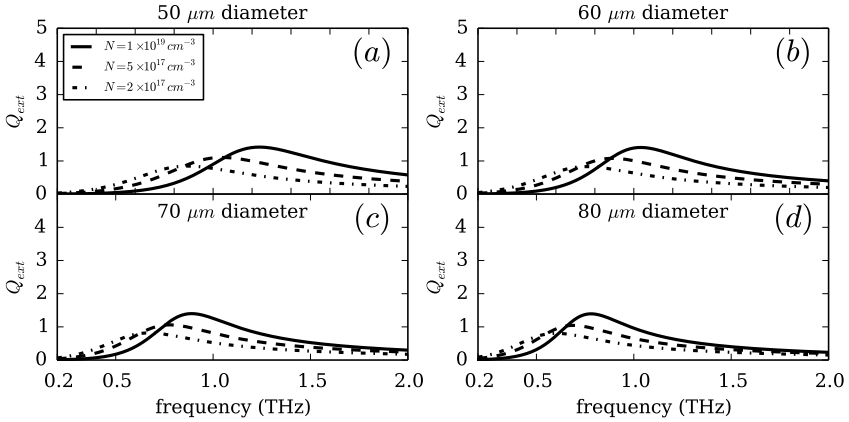

Figure 4.3: Extinction efficiencies of GaAs ellipsoids as a function of the size and carrier concentration under normal incidence illumination. The dash-dotted curves indicate a carrier concentration of 2×10^{17} cm^{-3}, the dashed curves 5×10^{17} cm^{-3}, and the solid curves 10^{19} cm^{-3}. The figures show the extinction spectra for ellipsoids having diameters in a plane perpendicular to the incident wave vector of 50 µm, 60 µm, 70 µm and 80 µm, respectively. All ellipsoids have a short axis parallel to the incident wave vector of 1.5 µm and are surrounded by a dielectric with a refractive index of $n = 2$.

as the particle diameter is increased (figure 4.4(b)). The strong dispersion of GaAs and the resonance shifts as the particle size is varied give rise to this reduction of the HWHM for larger particles: The larger values of the permittivity at lower frequencies are responsible for the reduction of the skin depth of GaAs and the concomitant reduction of the Ohmic losses, thus the narrowing of the resonance.

4.3 Arrays of plasmonic particles

When multiple dipolar particles are placed in close proximity, the field scattered by each of them will reach its neighbors, i.e. the neighboring particles will couple radiatively. The interference of this scattered field with the incident field can modify the overall scattering properties of the ensemble. Diffraction becomes relevant when the particles are placed in an ordered periodic array. Diffracted orders in the plane of the array, known as Rayleigh anomalies (RA), are responsible for an enhanced radiative coupling between the particles. This enhanced coupling results in hybrid diffraction-plasmonic modes known as surface lattice resonances (SLRs). In this section we discuss SLRs in arrays of THz plasmonic particles and their effect on the extinction spectrum of the arrays. In order to investigate the hybridization of a LR with a diffracted order it is important that higher orders are well separated in frequency. The simplest configuration meeting this condition is a 1D periodic lattice of scatterers.

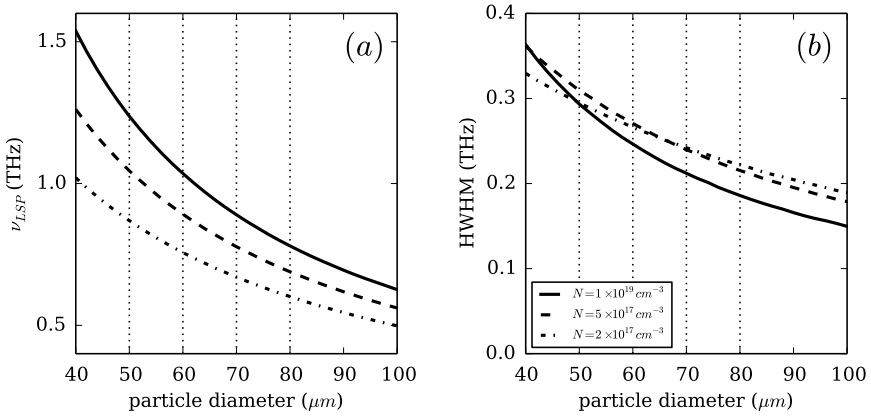

Figure 4.4: The LR resonance frequency (a) and the lower frequency half width half maximum (b) as a function of the diameter of the ellipsoid for the different carrier concentrations. The vertical dotted lines indicate the particle diameters for the extinctions shown in figure 4.3.

Coupled dipole model

An intuitive model for understanding the physics, and describing the interaction of an incident electromagnetic wave with an array of sub-wavelength scatterers is a system of coupled dipoles. In this model the collective response of the free electrons in each individual particle is approximated as an oscillating dipole. Each dipole absorbs and scatters a fraction of the incident light, depending on the incident wave-vector and the permittivity and geometry of the particle. This scattered light can reach other particles, and when placed in a periodic arrangement the scattered light from all particles can coherently interfere with the incident field. This interference can range from constructive to destructive and influences the effective spectrum of the extinction.

The polarization of each particle in an array (labeled with the subindex i) is defined as the product of its polarizability tensor with the local field at the particle position E_i^{loc}, which is the sum of the incident field E_i^{inc} and the scattered field by all other particles in the ensemble E_i^{ens}

$$p_i = \alpha_i E_i^{\mathrm{loc}} = \alpha_i (E_i^{\mathrm{inc}} + E_i^{\mathrm{ens}}) \; . \tag{4.4}$$

The scattered field produced by a point dipole representing particle j at the position of particle i is given by the product of the dipole moment p_j and the dipole-dipole interaction tensor, $G(r_i - r_j)$. For an array of dipoles the polarization of particle i is thus given by

$$p_i = \alpha_i \left[E_i^{\mathrm{inc}} + \sum_{j \neq i} G(r_i - r_j) p_j \right] \; . \tag{4.5}$$

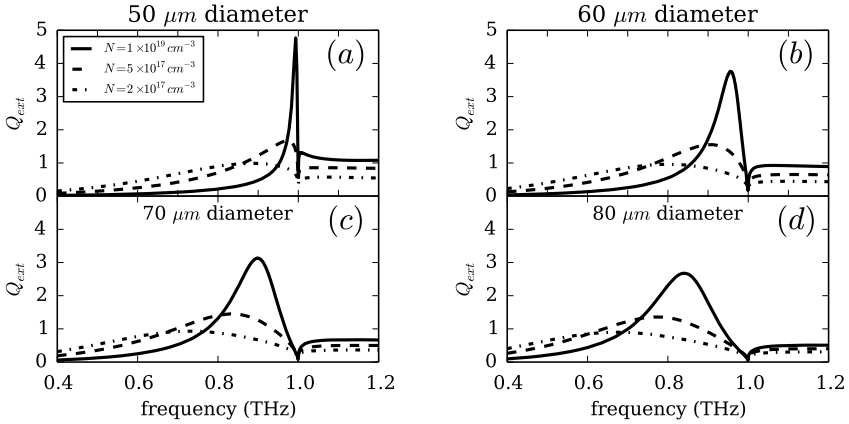

Figure 4.5: Extinction efficiencies of arrays of 2000 GaAs ellipsoids in a medium with refractive index $n = 2$ as a function of size and carrier concentration under normal incidence illumination. The pitch is 150 µm, resulting in a Rayleigh anomaly at 1 THz. The figures show the extinction spectra for ellipsoids having diameters of 50 µm, 60 µm, 70 µm and 80 µm, respectively. All ellipsoids have a height of 1.5 µm.

For a long chain of indistinguishable particles the polarization is independent of the particle position. Only for a small fraction of particles within an interaction length of a boundary $P \equiv p_i = p_j$ does not hold. Considering an array large enough to neglect this fraction, we can express the polarization as

$$P = \frac{\alpha E^{\text{inc}}}{1 - \alpha \sum_j G(r_i - r_j)} = \alpha^* E^{\text{inc}} \,, \tag{4.6}$$

where the effective polarizability α^* is defined as

$$\alpha^* = \frac{1}{1/\alpha - S} \,. \tag{4.7}$$

The term $S = \sum_j G(r_i - r_j)$ describes the coupling between the dipoles due to scattering.

When the array is illuminated such that the incident wave vector is parallel with the short axes of the ellipsoids, and the polarization direction is orthogonal to the direction of the array, we can use the scalar approximation for the polarizability and fields. Under these conditions the coupling term S for a 1D array is given by [133]

$$S = \sum_{\text{dipoles}} \exp(ikr) \left(\frac{ik}{r^2} - \frac{1}{r^3} + \frac{k^2}{r} \right) , \tag{4.8}$$

in which r is the distance of the respective dipoles. The scalar approximation is justified since, as a result of symmetry, the polarization of the particles is always parallel with the polarization of the incident field.

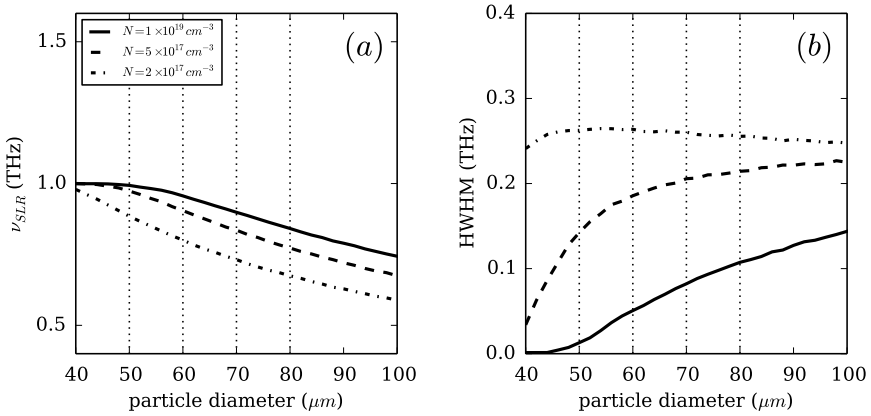

Figure 4.6: The SLR resonance frequency (a) and the lower frequency half width half maximum (b) as a function of the ellipsoid diameter for the different carrier concentrations. The dotted black vertical lines indicate the particle diameters for the curves shown in figure 4.5.

The extinction cross section of the coupled system in terms of this effective polarizability can now be written as

$$C_{\text{ext}} = 4\pi k \,\text{Im}(\alpha^*) \,. \tag{4.9}$$

An interesting situation in periodic arrays occurs at the frequency at which the incident field is diffracted in the direction parallel to the array, i.e. at the Rayleigh anomaly (RA) condition. This condition can be established by the conservation of the wave vector parallel to the interface, which for a plane wave incident normal to the surface leads to $\nu = mc/(\Gamma n)$, where c is the speed of light in vacuum, m an integer defining the diffracted order and Γ the period of the array.

GaAs surface lattice resonances

To illustrate the diffractive coupling of LRs in a row of identical scatterers forming a 1D periodic array we set the lattice constant Γ to 150 µm, which results in a RA at 1 THz in a surrounding medium with $n = 2$. The second order RA is at 2 THz, and it is largely detuned in frequency from the first order. For scatterers with the same properties and dimensions as described in section 4.2, the extinction spectra of a row of identically coupled ellipsoidal particles are calculated and displayed in figure 4.5. As in figure 4.3, the particles have long axes of 50 µm, 60 µm, 70 µm and 80 µm, respectively, a height of 1.5 µm and are surrounded by a dielectric with permittivity $n = 2$, e.g. quartz. The extinction cross sections are calculated using the coupled dipole method for a 1D array of 2000 particles and are normalized to the geometrical

cross sections of the respective particles. For this number of particles the spectra are converged to those of an infinite array.

Two main and distinct features can be appreciated in the spectra of figure 4.5. First, at the frequency of the RA the extinction efficiency is reduced. This reduction is a consequence of the scattered field from each particle being out of phase with the local incident field. Second, a pronounced resonance with an enhanced extinction appears at frequencies lower than the RA. For these frequencies the scattered field is in phase with incident field. These resonances with enhanced extinction are known as surface lattice resonances [70] and, besides of their large extinction, they are characterized by a narrow line width. This characteristic highlights the hybrid character of SLRs originating from the enhanced radiative coupling of localized resonances mediated by photonic/diffraction modes. The hybrid character can be also appreciated in the dependence of the resonant frequency and width with the particle size as shown in figure 4.6. Similar to the resonances of the individual particles shown in figure 4.4(a), the SLR blueshifts by decreasing the long axis of the ellipsoid and by increasing the carrier concentration. However, the blueshift in the array is limited by the frequency of the RA at 1 THz. A more remarkable difference with LRs can be found in the dependence of the HWHM with the particle diameter. The smaller the particle diameter, the stronger the radiative coupling of the LRs mediated by the Rayleigh anomaly, and the narrower the resonance becomes. The coupling strength is determined by the detuning between the resonant frequency of the LRs and the RA. This characteristic makes it possible to actively control the extinction by particle arrays, enhancing or suppressing it by tuning the carrier concentration in the semiconductor.

The mechanism enabling the tuneability of the extinction is further elucidated in figure 4.7. Figure 4.7(a) shows both the LR (dashed curves) and SLR (solid curves) spectra of a disk having a diameter of 60 µm for the carrier concentrations 2×10^{17} cm^{-3}, 5×10^{17} cm^{-3} and 10^{19} cm^{-3}, as shown in figures 4.3(b) and 4.5(b). In figure 4.7(b) the real component of $1/\alpha$ for these carrier concentrations is compared against both components of S. The extinction of the coupled system has a maximum whenever the real component of $(1/\alpha - S)$ vanishes, i.e. at the poles in the real axis of the effective polarizability given in (equation 4.7). The maxima in extinction are indicated by the dotted lines in figure 4.7(a). These lines mark also the crossing of $\Re(1/\alpha)$ with $\Re(S)$ at frequencies below 1 THz. The array factor S has a large value at the RA, i.e. 1 THz, as indicated by the vertical black dashed line, dominating the denominator in equation 4.7 and minimizing α^*. The asymptotic behavior at the RA also explains why in figure 4.6 the SLR frequency is limited to frequencies lower than 1 THz. By tuning the carrier concentration, and thus the magnitude of α, the frequency at which $\Re(1/\alpha)$ equals $\Re(S)$, thus the SLR, can be precisely controlled. We can see in figure 4.7(b) that $\Re(1/\alpha) = \Re(S)$ for a carrier concentration of $N = 10^{19}$ cm^{-3} at 1.08 THz, while for this frequency we do not observe a maximum in the extinction efficiency. The reason for the absence of this maximum is the large value of the imaginary component of S, represented by the magenta curve in figure 4.7(b), which reduces the extinction efficiency defined in (equation 4.9).

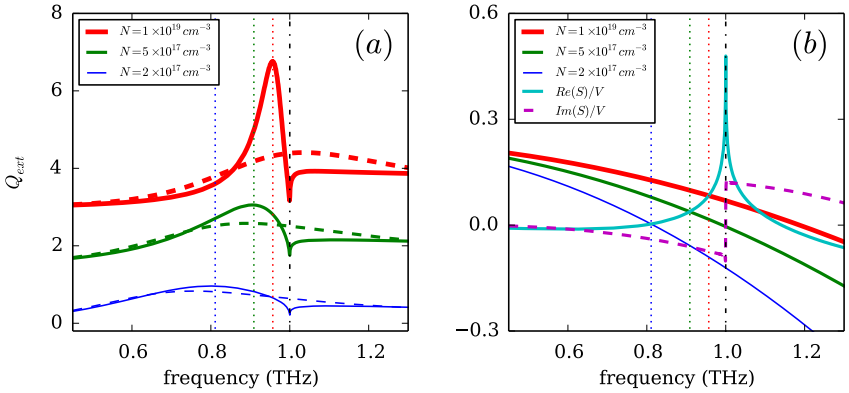

Figure 4.7: (a) Surface lattice resonances in diffractively coupled ensembles of GaAs ellipsoids with a 60 µm diameter as shown in figure 4.5(b) (solid curves), and the uncoupled responses as shown in figure 4.3(b) (dashed curves). For clarity the spectra are displaced vertically. (b) The real and imaginary components of the array factor S as calculated with the coupled dipole approximation for a 1D array of 2000 particles, and for each carrier concentration $1/\alpha$. The dotted lines mark the extinction maxima, and the crossings of $\Re(1/\alpha)$ with $\Re(S)$, the dash-dotted line marks the Rayleigh anomaly condition. S and $1/\alpha$ are normalized against the ellipsoid volume V.

4.4 Complex representation

The mechanism of how the diffractive coupling in a periodic arrangement of scatterers influences the extinction spectrum around the RA condition becomes more intuitive when the various electric field components that contribute to the spectrum are represented as vectors in the complex plane. These components are the total transmitted field, which is given by the coherent sum of both the incident field and the field scattered from the particles in the forward direction:

$$\mathbf{E}^t = \mathbf{E}^{\mathrm{inc}} + \mathbf{E}^{\mathrm{sca}} \,. \tag{4.10}$$

The scattered field depends on the polarizability and the local field and is given by

$$\mathbf{E}^{\mathrm{sca}} = 4\pi k i \frac{\alpha \mathbf{E}^{\mathrm{loc}}}{\Gamma^2} \,. \tag{4.11}$$

The local field is the sum of the incident and the diffracted field from the ensemble of scatterers in the plane of the array

$$\mathbf{E}^{\mathrm{loc}} = \mathbf{E}^{\mathrm{inc}} + \mathbf{E}^{\mathrm{ens}} \,. \tag{4.12}$$

In the limit of an infinite lattice all particles are interchangeable, and we can drop the labeling of the individual dipoles as $\mathbf{p}_i \equiv \mathbf{p}$. Equation (4.5) can now be re-written as

$$\mathbf{E}^{\text{ens}} = S\mathbf{p} \,, \tag{4.13}$$

and equations (4.4) and (4.5) can be solved for $\mathbf{p}$ as

$$\mathbf{p} = \frac{\mathbf{E}^{\text{inc}}}{\alpha^{-1} - S} \,, \tag{4.14}$$

which allows us to express the diffracted field in terms of the incident field, polarizability and lattice sum as

$$\mathbf{E}^{\text{ens}} = \frac{\mathbf{E}^{\text{inc}}}{1/(\alpha S) - 1} \,. \tag{4.15}$$

In case of a system of isolated particles there is no diffracted field and equation (4.11) for the scattered field reduces to

$$\mathbf{E}^{\text{sca}} = 4\pi k i \frac{\alpha \mathbf{E}^{\text{inc}}}{\Gamma^2} \,. \tag{4.16}$$

The colors of the expressions introduced below match the calculated arrows as shown in figure 4.8. In this figure the diffractive coupling is analyzed for the 60 µm diameter GaAs ellipsoids with a carrier concentration of 10^{19} cm^{-3}, corresponding to the red curves in figure 4.7.

Figure 4.8 shows the various electric fields that contribute to the LR/SLR, calculated with the coupled dipole model, as vectors on a unit-circle when all fields are normalized to the incident field. The length of the vectors represents the magnitude of each field, the angle their phase ϕ relative to the incident field according to

$$\mathbf{E} = E_0 e^{i\phi} \,. \tag{4.17}$$

Panel 4.8(a) is calculated for the isolated scatterer, at the frequency where the SLR of the lattice has the maximum in the extinction. This is at 0.96 THz. The incident field (grey arrow) drives the conducting electrons in the scatterer, which radiate in turn in the forward direction (red arrow). The magnitude and relative phase are related to the complex value of the particle polarizabiliy. The coherent sum of the incident field and the scattered field result in a reduction and change in phase of the total transmitted field, which is indicated with the blue arrow. When the frequency is increased to that of the RA condition at 1.0 THz, as shown in figure 4.8(a), there are no significant changes in the representation of the fields compared to those calculated for 0.96 THz. This is related to the LR being a very broad resonance, and the value of the polarizability has not changed significantly upon the change in frequency.

For the periodic lattice, an additional term is present to account for the diffractive coupling. This term is indicated by the green arrows. The magnitude and phase of the field resulting from this diffractive coupling are related to the periodicity of the lattice and the detuning from the RA condition. This field, that is diffracted in

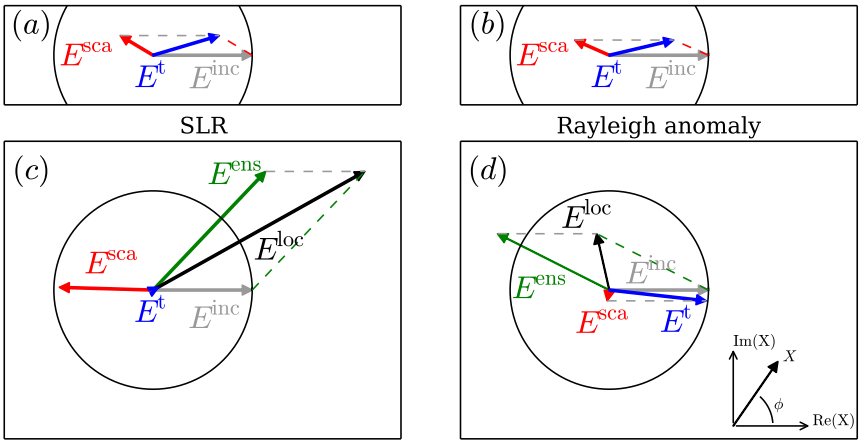

Figure 4.8: Coupled dipole model calculations of amplitudes and phases of the fields that contribute to the diffractive coupling, represented by arrows. Panels (a) and (b) represent an isolated dipole, panels (c) and (d) a lattice. (a) and (c) are calculated at the SLR frequency where the extinction is enhanced, (b) and (d) at the Rayleigh anomaly condition which has a transparency window. The colors of the arrows match the variables in equations 4.10-4.16: The gray arrows indicate the incident field, the red arrows the scattering in the far-field. The green arrows indicate the contributions of the other dipoles to the local field (black) due to diffractive coupling, and the blue arrow represents the total far-field. The inset in (d) indicates the coordinates of a vector in the complex plane.

the plane of the lattice contributes together with the incident field to the local field (black arrows) at the position of the scatterers. However, as a result of the diffractive coupling both the magnitude and the phase of the local field have changed. Since the relation between the local field and the forward scattered field is determined by the polarizability, it is these changes in phase and magnitude of the local field due to the diffractive coupling which is responsible for the large difference in extinction between the isolated particles and the chain of particles.

The isolated particle from figure 4.8(a) can be compared to the chain of particles at the SLR condition, which is shown in figure 4.8(c). At the SLR condition in the chain the amplitude and phase of the diffracted field (green arrow) change the local field such, that the field scattered by the dipoles (red arrow) is in anti-phase compared to the incident field (grey arrow) and interferes destructively. As a result, the extinction is maximized. The phase that will be measured when conducting experiments corresponds to the phase, or angle, of the red arrows in figure 4.8. In all cases the angle between the local field and the scattered field is determined by the phase of the polarizability. This is, in this example, practically the same for the SLR frequency and RA condition, and exactly the same for the lattice as for the isolated

dipole. However, in the case of the isolated dipoles the local field is identical to the incident field due to the absence of diffractive coupling. For the lattice the phase of the local field is strongly dependent on the diffracted field. At the RA condition (figure 4.8(d)) the wavelength equals the pitch ($\Gamma = 2\pi/k$). At this condition the diffracted field (green arrow) arriving at each scatterer has been delayed by an integer number of oscillations. As a consequence, the diffracted field has approximately the same phase as the scattered field of the isolated scatterer of figure 4.8(b). The amplitude is such, that when the scattered field (red arrow in figure 4.8(d)) is added to the incident field the resulting vector lies still close to the unit circle. This can be understood as an amplitude in the far field which has not changed, but only picked up a finite additional phase.

4.5 Conclusions

We have investigated theoretically the THz extinction by individual GaAs particles and by periodic arrays. The localized surface plasmon resonance in individual particles depends on both the particle diameter and the charge carrier density. Using the coupled dipole approximation, we show that a 1D lattice of these particles can exhibit an enhanced extinction which is the result of the radiative coupling of localized surface plasmons through diffraction. Additionally, an intuitive representation is introduced to understand and explain the mechanism of how diffractive coupling influences the phases and amplitudes of the electric fields. The possibility to tune the resonance frequency and strength of localized resonances by controlling the carrier density in the GaAs particles, enables to control the enhanced THz extinction in periodic arrays. This approach may be interesting for the development of efficient THz modulators.

Chapter 5

Control of THz resonances in arrays of semiconductor antennas

Doped semiconductor structures can sustain localized resonances (LRs). In an ensemble of these structures LRs can couple through diffraction. In this chapter we study at terahertz frequencies the coupling of LRs to diffraction orders in a periodic array of Si square particles, and photo-generated arrays of THz resonators in a continuous GaAs layer. Experimental results from the Si arrays are supported by coupled dipole model calculations and simulations using the finite-difference in time-domain method. Numerical simulations show local intensity enhancements over an order of magnitude in the near-field, and an average intensity enhancement in the unit-cell of a factor 2.5*. We demonstrate the concept of active control of surface lattice resonances in a continuous GaAs thin film through local photo-excitation. Using a spatial light modulator an image is projected on the semiconductor, inducing free charge-carriers only on the illuminated areas. By changing the pattern of illumination, the optical properties of the film at THz frequencies can be controlled. The experimental results are compared against numerical simulations and are found to be in good agreement.*

5.1 Introduction

The previous chapter discussed theoretically the extinction of 1D chains of GaAs ellipsoids, and how diffractive coupling influences their extinction spectra. In this chapter we demonstrate experimentally, and verify theoretically how localized resonances (LRs) of semiconductor scatterers couple through diffraction when they are ordered in a 2-dimensional periodic array. The electromagnetic response of such an array is called a surface lattice resonance (SLR). In particular we investigate how the THz extinction of arrays of Si particles correlate with the frequency detuning between the LR and the Rayleigh anomaly (RA) condition. A RA is the condition where a diffractive order grazes the plane of the array. We also relate the far-field enhanced extinction to local enhancements in the near-field. Although a 1-dimensional chain of scatterers is the simplest periodic structure, a 2-dimensional lattice is described by the same physics. A 2D lattice has a larger filling fraction of particles than a 1D chain, and increases the measured extinction.

A sample containing a continuous flat layer of GaAs will be used to demonstrate the photo-generation of SLRs in a thin semiconductor sample. As described in chapter 2 of this thesis, illuminating a semiconductor with photons of energies exceeding that of the bandgap induces electron-hole pairs that can contribute to the conduction of electrical charge. When projecting an image on the semiconductor, this image will be converted into a spatially dependent profile in the local concentration of charge carriers in the semiconductor. The induced charge carriers are confined to these illuminated areas, and the projected image is translated into a spatial dependent local permittivity. The photo-generation of THz diffraction gratings on Si was recently demonstrated by Okada and coworkers by illumination of the Si through a spatial light modulator (SLM) [102, 141]. Chatzakis et al. extended this work to GaAs gratings generated by illumination through an optical mask [142]. THz beam steering using photoactive diffraction gratings has been recently demonstrated by Busch and Xie and their coworkers [143, 144], beam steering by Steinbusch et al. [145], and photo-generated metamaterials have been theoretically proposed by Rizza et al. [146]. Georgiou et al. [117] bridged the emerging fields of active photonics and THz metamaterials by demonstrating experimentally the full all-optical generation of linear antennas at THz frequencies.

This chapter is organized as follows: first a description of the samples and the experimental conditions are given. Second, SLRs are demonstrated experimentally in periodic arrays of intrinsically doped Si particles, and compared to results from finite-difference in the time-domain (FDTD) simulations. The coupled dipole model (CDM) is used to explain the underlying physics. Furthermore, the near-field enhancement is discussed and a comparison is made to the simulated and measured far-field enhanced extinctions. In section 5.6 the SLRs that are launched from structures that are photo-generated in a GaAs thin layer are discussed. The experimental results are compared against FDTD in section 5.6, commenting on the limiting factors and future improvements for the experimental technique. The chapter is ended with conclusions.

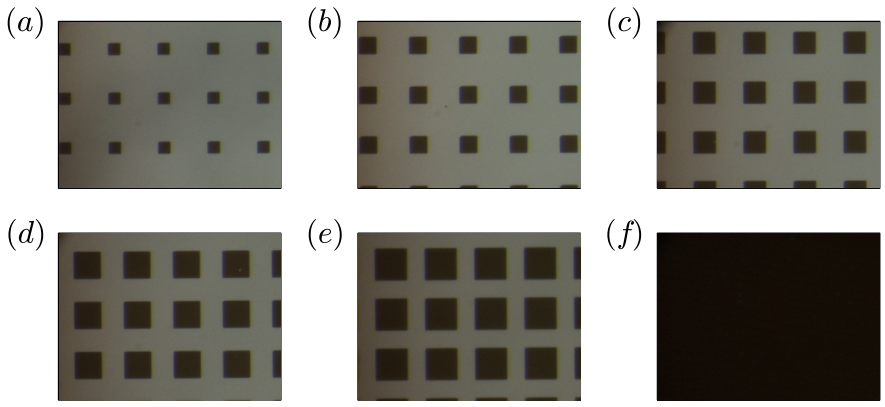

Figure 5.1: Optical microscope images of arrays of Si tiles on an amorphous quartz substrate. The pitch Γ is 100 μm, the particle lengths d are 25 μm (a), 35 μm (b), 45 μm (c), 55 μm (d) and 65 μm (e). Panel (f) shows a Si layer.

5.2 Samples and experimental setup

The semiconductor structures studied in the first part of this chapter consist out of 2D periodic arrays of 1.5 μm thick crystalline Si square tiles. From sample to sample the length of the tile ranges from $d = 25$ μm to $d = 85$ μm, while the lattice constant is kept constant at $\Gamma = 100$ μm. The fabrication has been done using standard microfabrication processes, as mentioned in chapter 2 of this thesis and described by Berrier and coworkers in refs [114, 115] in more detail. The layer containing the Si structures is bonded at both sides to an amorphous quartz substrate which is transparent at terahertz frequencies. The bonding layer is benzocyclobutene (BCB) and has an estimated thickness of 3 μm. These bonding layers do not significantly interact with the terahertz radiation. Optical microscope images of the samples are shown in figure 5.1 (a)-(e), for arrays with squares of 25 μm, 35 μm, 45 μm, 55 μm and 65 μm in length respectively. The last panel (f) shows an unstructured Si reference layer. The images are taken after the lithography was done but before the last bonding step, in which the Si structures were bonded to the superstrate to form a symmetric sample.

Single-crystalline Si which is not intrinsically doped at room temperature has most of the electrons in the valence band, and is transparent at terahertz frequencies since the semiconductor bandgap of 1.12 eV exceeds the thermal energy $k_B T$. Si behaves as a dielectric with a refractive index of $n = 3.4$ and is practically lossless. A permanent, intrinsic metallic behavior has been introduced by implanting the Si with arsenic (As) atoms, with a concentration of free carriers in the order of $N \approx 10^{20}$ cm^{-3}. The experiments have been carried out using the terahertz time-domain spectroscopy (THz-TDS) setup, which uses optical rectification for THz generation and electro-optic sampling for detection. This setup is described in section 2.1 of his thesis.

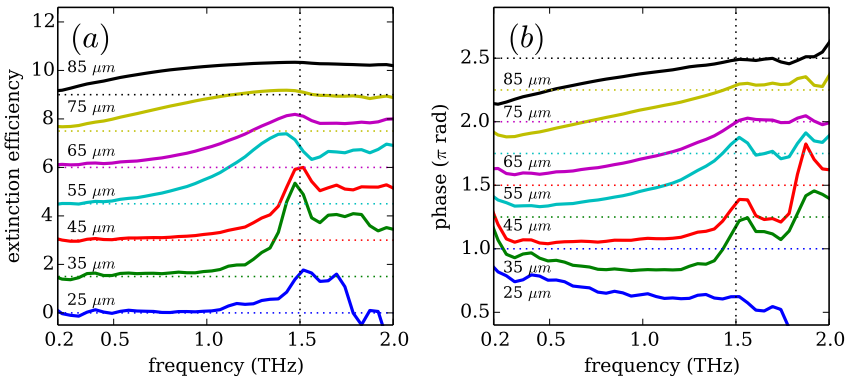

Figure 5.2: Extinction efficiency (a) and differential phase delay (b) spectra of the Si particle arrays, referenced against a sample without Si structures. From the solid blue to the solid black curves the particle sizes increase from 25 μm to 85 μm in steps of 10 μm. For clarity the curves are shifted vertically, as indicated by the horizontal dotted lines. The vertical dotted line indicates the Rayleigh anomaly condition at 1.5 THz.

5.3 Experimental results

The arrays of Si particles have been measured in transmission with the THz-TDS experimental setup. Intensity spectra $I(\nu)$ are calculated from the square of the Fourier transform of the time-domain transients. A sample without any silicon, i.e. only quartz and BCB, is used as a reference. For each array the transmitted intensity is normalized to this reference, and corrected for the filling fraction f of the Si in each unit cell ($f = d^2/\Gamma^2$) to determine the extinction efficiency

$$Q_{ext}(\nu) = \frac{1 - I(\nu)/I_{\mathrm{ref}}(\nu)}{f} \,. \tag{5.1}$$

The extinction efficiencies are shown in figure 5.2(a) as the solid curves, for arrays with particles ranging in length from 25 μm (blue curve) to 85 μm (black curve) in steps of 10 μm. The curves are vertical off-set for clarity, as indicated by the horizontal dotted lines. The vertical dotted line indicates the RA condition, which is at 1.5 THz for an array with a lattice constant of $\Gamma = 100$ μm and is surrounded by a medium with a refractive index of $n = 2$.

Three regimes of responses can be identified: For large particles, 65 μm (magenta curve)-85 μm (black curve), the response of the arrays show mainly a broad resonance. For particles in the range 35 μm (green curve)-55 μm (cyan curve) a characteristic surface lattice resonance appears close to the RA condition. The resonance becomes broad again for the smallest particles of 25 μm (blue curve).

The extinction of the arrays is a result of the induced electromagnetic field from the scatterers interfering destructively with the incident field at the position of the detector. The phase of this field from the scatterers, relative to the phase of the incident field, is shown in figure 5.2(b). This phase, which is indicated as the differential phase delay, is calculated from the complex Fourier transforms of the time-domain transients as

$$\phi = \arg(t - t_{\text{ref}}) - \arg(t_{\text{ref}}) \; . \tag{5.2}$$

These phase spectra show a trend consistent with the extinction spectra. For the smallest and largest particles the curves are smooth, while for the lengths in the range 35 μm (green curve)-55 μm (cyan curve) there is a pronounced local maximum in the phase. This maximum in phase appears at slightly higher frequencies than its corresponding maximum in extinction, and is consistently close to the RA condition.

5.4 Coupled dipole model

The experimental results are compared to calculations based on a coupled dipole model. The model presented here follows the main argumentation as introduced in chapter 4, but deviates from this argumentation on two aspects: The dipoles are in a 2D square lattice as opposed to the 1D chain, which requires a more general form of the dipole-dipole interaction tensor G, and a finite number of dipoles is assumed along both axes of the lattice instead of the infinitely long chain. The latter results in the dipoles near the edge of ensemble having a different polarization than those in the center.

For a disk of diameter d which is illuminated at normal incidence the extinction efficiency can be written as:

$$Q_{\text{ext}} = \frac{16k\Im(\alpha)}{d^2} \; , \tag{5.3}$$

where $k = n_s\omega/c$ is the wavevector in the surrounding medium with refractive index n_s and $\Im(\alpha)$ represents the imaginary component of the dipolar polarizability of the disk as defined in equation (1.18). The dipolar polarization of a particle depends on its polarizability and the local field at the position of the particle. For each dipole i in the ensemble this is the sum of the incident field $\mathbf{E}^{\text{inc}}$ and the field $\mathbf{E}^{\text{ens}}$ which is scattered from all the other dipoles in the ensemble

$$\mathbf{p}_i = \alpha\mathbf{E}_i^{\text{loc}} = \alpha\left(\mathbf{E}^{\text{inc}} + \mathbf{E}_i^{\text{ens}}\right) \; . \tag{5.4}$$

This scattered field can be calculated from the product of each polarization and the dipole-dipole interaction tensor [70], via a summation over all dipoles j different than dipole i.

$$\mathbf{E}_i^{\text{ens}} = \sum_{j\neq i} G(\mathbf{r}_i - \mathbf{r}_j)\mathbf{p}_j \; . \tag{5.5}$$

In differential form this tensor is defined as

$$G(\mathbf{r}) = (k^2 + \nabla\nabla)\frac{e^{ikr}}{r} \; . \tag{5.6}$$

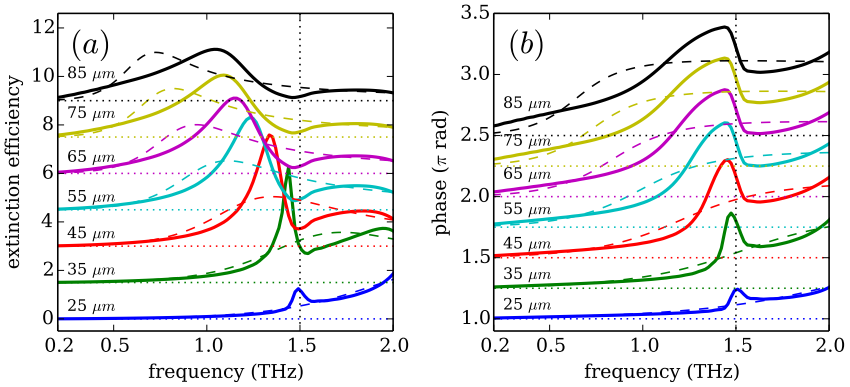

Figure 5.3: Extinction (a) and phase (b) spectra for arrays of 20×20 particles as calculated with the coupled dipole model and the modified long wavelength approximation. The solid curves represent the response of the arrays, the dashed curves that of an isolated particle. The vertical dotted line at 1.5 THz indicates the Rayleigh anomaly condition. For clarity the curves are shifted vertically, as indicated by the horizontal dotted lines. The Si particles are approximated as oblate spheroids, and are homogeneously surrounded by a loss-less material with a refractive index of $n = 2$.

The above equations can be re-written as a linear set of self-consistent equations

$$\mathbf{E}^{\text{inc}} = (\alpha^{-1} I - S)\mathbf{P} = A\mathbf{P} \,, \tag{5.7}$$

where I is the identity matrix and matrix S contains all the dipolar interactions. For finite arrays these equations can be solved for $\mathbf{P}$ by calculating the inverse of the matrix A. The extinction efficiency under these conditions is given by

$$Q_{\text{ext}} = \frac{16k}{d^2} \frac{\text{Im}(\mathbf{E}^{\text{inc}} \cdot \mathbf{P})}{|\mathbf{E}^{\text{inc}}|^2} \,. \tag{5.8}$$

Extinction spectra are calculated for arrays of 20×20 oblate spheroids, with parameters matching the experiments as close as possible. The length of the short axis of each dipole is taken as the height of the Si particles (i.e. 1.5 μm) and the dimensions of the long axes are set to the respective particle lengths. The refractive index used to describe the polarizabilities of the dipoles is a fit to the Drude model for Si with $N = 3.6 \times 10^{19}$ cm^{-3} and $\mu_e = 0.012$ m^{2}V^{-1}s^{-1}, as shown in figure 2.9. The refractive index of the surrounding material is taken as $n = 2$. The pitch of the lattice is kept at 100 μm for all the arrays.

The results of these calculations are shown in figure 5.3. Figure 5.3(a) shows with the solid curves the extinction efficiency of the ensemble, and with the dashed curves the response for an isolated particle. As for the experimental results the spectra

are vertically displaced for clarity. The vertical dotted line indicates the Rayleigh anomaly condition at 1.5 THz. Results are shown, from bottom to top, for particles with lengths of 25 μm to 85 μm in steps of 10 μm.

The resonances for the isolated particles are described as localized resonances. This resonant response is due to the coherent oscillation of the free charge carriers. The general trend is a redshift in the resonance for an increasing length of the particle while the shape of the resonance remains similar. The extinction efficiency is in first order independent of the particle length and is slightly larger than 2. The redshift can be understood from equation (1.18) where α^{static} scales with the volume and the denominator can be expressed in terms of kd. A particle with a larger geometrical cross section will have a resonant condition at a smaller wavenumber, which corresponds to a lower frequency and explains the redshift.

The extinction spectra for the arrays are much richer. For the largest particles (black to magenta curves) the resonance is somewhat blueshifted from the LR towards the RA condition, but remains broad. As the LR approaches the RA condition (cyan and red curves), the extinction gets enhanced, and the resonance becomes more narrow. The extinction efficiency is enhanced the most when the LR of the individual particles overlaps with the RA condition of the array, which corresponds to the particles of 35 μm and is indicated with the green curve in figure 5.3(a). The resulting extinction spectrum is asymmetric with resembles a Fano-like shape. These trends of enhanced extinction match the experimental results shown in figure 5.2(a). For the smallest particles (blue curve), when the LR is at much higher frequencies than the RA, the extinction efficiency of the array is not very different from that of the individual particles.

The phase of the average polarization of the dipoles is shown in figure 5.3(b), and is calculated as $\phi = \frac{1}{n}\sum_i \arg(\mathbf{p}_i)$. Solid curves represent the coupled system, and dashed curves isolated dipoles. The phase of the latter undergoes a smooth transition from an underdriven to an overdriven system, centered around the LR resonance frequency, which redshifts as the particle length increases. The phase of the arrays follows this trend, but has an additional modulation of the phase slightly redshifted from the RA condition. As in the case of the experimental results (figure 5.2) the maximum in phase appears at higher frequencies than the maximum in extinction, and remains close to the RA condition.

The phase resulting from the calculations (figure 5.3) and the experiments (figure 5.2) are a result of the mechanism that has been introduced in the previous chapter for a 1D chain of GaAs particles. The phases shown in figures 5.3(b) and 5.2(b) relate to the phase, or angle, of the red arrows shown in figure 4.8. Around the frequency of maximum extinction of the SLR, as illustrated in 4.8(c), the amplitude and phase of the diffracted field (green arrow in this figure) are such, that the field scattered by the dipoles (red arrow) is in anti-phase compared to the incident field and the two interfere destructively. This results in an increase of the phase of the field scattered into forward direction around this condition. Away from the SLR frequency the magnitude of the diffracted field is much smaller, reducing the change in phase of the local field (black arrow) and as a result, the forward scattered field.

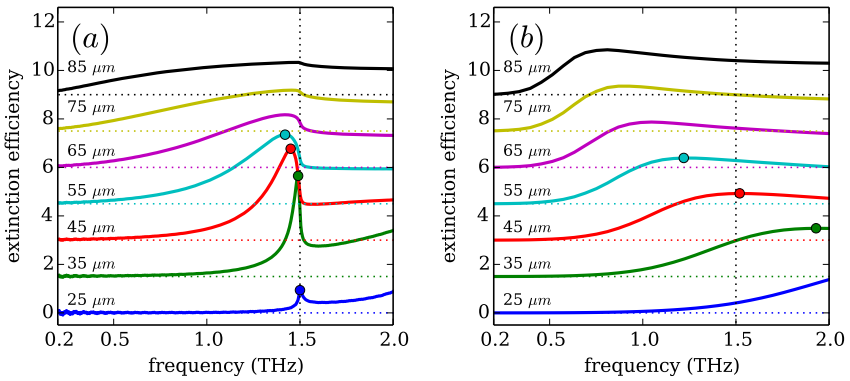

Figure 5.4: Extinction efficiency spectra simulated with FDTD for periodic arrays of square Si particles with a length as given in the figure (a) and isolated particles (b). The simulations include minor losses in the surrounding substrates and BCB bonding layer. For clarity the curves are shifted vertically, as indicated by the horizontal dotted lines. The vertical dotted line indicates the Rayleigh anomaly condition. The circles correspond to the frequencies at which the intensities in figure 5.7 are simulated.

5.5 Numerical simulations

To get a better insight in the interpretation of the experiments, simulations have been performed using the finite-difference in the time-domain method (Lumerical). The layout of the unit cell and dimensions of the particles are taken from the microscope images as shown in figure 5.1. For the refractive index of the Si the Drude fit shown in figure 2.9 is used, which corresponds to a concentration of charge carriers $N = 3.6 \times 10^{19}$ cm^{-3} with a mobility of $\mu_e = 0.012$ m^{2}V^{-1}s^{-1}. The surrounding medium is considered as quartz with minor losses $\tilde{n} = 2.0 + 0.01i$. For isolated particles the simulation volume is surrounded by perfectly matched layers (PMLs) and the extinction cross sections simulated with FDTD have been normalized to the geometric cross sections of the Si particles, resulting in an extinction efficiency. The results for the periodic arrays are simulated using periodic boundary conditions (PBC) in the directions perpendicular to the propagation direction of the incident field and the extinction has been normalized to the filling fraction of the particles. The resulting extinction efficiencies are shown in figure 5.4(a). The responses of the isolated particles are shown in figure 5.4(b), and are simulated with a single particle in a simulation volume surrounded by perfectly matched layers (PMLs).

For the periodic structures the results agree very well with the experimental data. For the large particles (65 µm-85 µm) the spectral response is broad, and there is no pronounced resonance around the RA condition. Also for the smaller particles the resonance is weak. For the arrays with particle lengths in the range 35 µm-

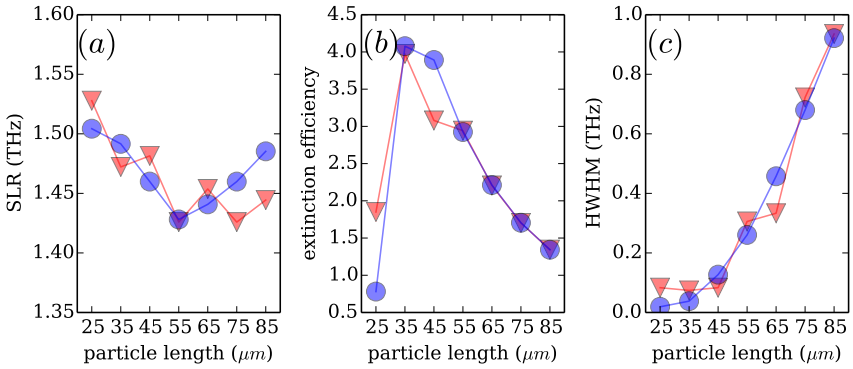

Figure 5.5: Analysis of the extinction spectra of the measured arrays (fig. 5.2, red triangles) and the results from FDTD simulations (fig. 5.4, blue circles). (a) shows the SLR frequency, which is the frequency of maximum extinction. The corresponding extinction efficiency is plotted in (b). The half width at half maximum of the SLR is shown in (c).

55 µm a pronounced enhancement of the extinction is present, slightly redshifted from the Rayleigh anomaly. The FDTD simulations tend to over-estimate the magnitude and under-estimate the width of the resonances. This occurs mostly for the smaller particles and can be attributed to the finite width of the experimental THz beam while the FDTD simulations have been carried out with plane-wave illumination. The extinction spectra for the isolated structures show a pronounced redshift as the particle length increases. The finite extinction at high frequencies is attributed to higher order resonances. The magnitude of the extinction efficiency in these results is independent of the particle length.

Analysis

The characteristics that define a resonance are its central frequency, magnitude and width. For the experimental data (figure 5.2), and the results from the FDTD simulations (figure 5.4) these parameters have been extracted for the SLRs and are shown in figure 5.5. The red triangles correspond to the experimental data, the blue circles to the spectra simulated with FDTD. The SLR frequency, defined as the frequency of maximum extinction and shown in figure 5.5(a), has for both the FDTD and experiments values in the range of 1.42 THz-1.53 THz. This is indicates that the diffractive coupling strongly modifies the collective response of the localized resonances. The maximum extinction efficiency (figure 5.5(b)) has a maximum value of 4 at a particle length of 35 µm. It is not practical to assign a full width at half maximum to the resonances due to the asymmetry of the extinction spectra, with an extinction that remains significant at high frequencies in both simulation and experiment. The extinction does however drop to zero at low frequencies, and

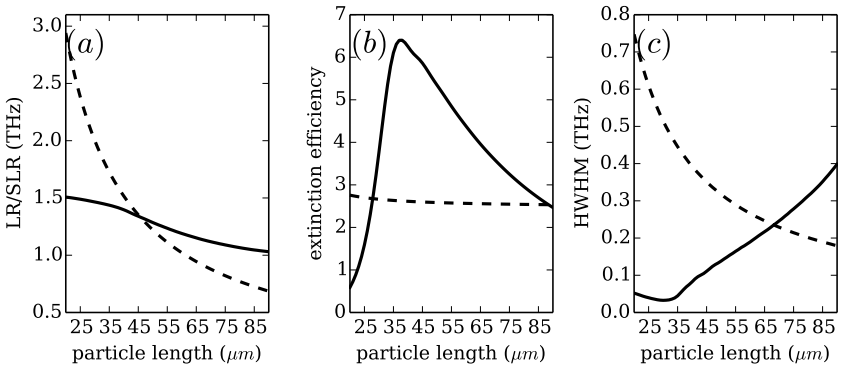

Figure 5.6: Analysis of the extinction spectra calculated with the Coupled Dipole Model (fig 5.3). (a) shows the frequency and (b) the extinction efficiency at the LR/SLR condition. The half width at half maximum of the resonance is shown in figure (c). The solid curves represent the SLR of an array of dipoles, the dashed curves the LR of an isolated particle.

therefore the lower half width at half maximum (HWHM) is used to quantify the widths of the resonances. As can be seen in figure 5.5(c), for both the FDTD and the experimental results the width increases as the particle length is increased.

The same analysis has been done for the SLRs calculated with the coupled dipole model. This is shown in figure 5.6, where the results of a 20×20 lattice (solid curves) are compared with those of an isolated scatterer (dashed curves). Even though the CDM approximated the rectangular tiles as ellipsoidal dipoles, and ignored the presence of the bonding layer, there is a qualitative agreement with experimental and numerical results. The CDM predicts in figure 5.6(a) a pronounced SLR frequency shift which scales with the particle length. For small particles the LR frequency is at high frequencies and the RA condition asymptotically keeps the SLR at 1.5 THz. In the experiments and FDTD the larger particles are no longer in the limit of truly dipolar behavior. The CDM neglects any higher order modes in these larger particles that couple through diffraction at the RA condition at 1.5 THz. The dependence of the extinction of the SLR on the particle length shown in figure 5.6(b) agrees very well with the experiments, reproducing the maximum around the particle length of 35 µm. This enhancement is due to the enhanced interaction with the lattice, as can be learned from the extinction efficiency of the isolated particles which is practically independent of the particle length. The small increase of the extinction efficiency for smaller particles can be attributed to the material dispersion and changing eccentricity of the ellipsoid.

The quality factor of the LR resonance, which is defined as the center frequency divided by the resonance width, is in first order independent from the particle length. This is confirmed by the trend shown in figure 5.6(c), where the HWHM of the LR scales inversely with the particle length as well. The solid curve displays a completely

different behavior. A reduction in the length of the particle reduces the width of the resonance, which is a direct result of the SLR approaching the RA condition. This is in agreement with the results from the experiments. Finally, we should mention that these trends are in agreement with the results presented in chapter 4 of this thesis, where 1D chains of doped GaAs dipoles were discussed.

Near fields

The enhanced extinction efficiency is closely related to a redistribution of energy in the near field in the proximity of the particles. This is illustrated with FDTD simulations. We compare isolated particles to a periodic lattice of particles at their respective resonance frequencies. These frequencies are indicated in figure 5.4 with the colored circles for each of the particle lengths under consideration. Cross-sections are shown in figure 5.7 for particles of 25 µm-55 µm in length. The cuts are taken through the center of each particle in the plane defined by the wavevector and the polarization.

Panels (a)-(d) in figure 5.7 show the near-field intensity enhancements in the periodic lattices for increasing particle length. We see that the fields are enhanced up to two orders of magnitude at the extrema of the particles, as a result of the accumulation of the electrons that are driven by the incident electric field. The fields however are enhanced not only in the proximity of the particle, but also extend in the region below the plane of the array. This effect is the largest in panel 5.7(b) where the local field intensity of the particle of 35 µm in length is shown. This is also in agreement with the results in figure 5.6(b), where for the 35 µm particles a large extinction efficiency is observed. The regions of reduced intensity in the upper halves of the figures are a result of destructive interference between the incident field and the fraction of the THz radiation that is reflected from the particles.

For the single particles at their respective LR resonance frequency (panels (e)-(h) of figure 5.7) the field is enhanced mostly at the edges of the particle, but not as pronounced as for the particles in the lattice.

The far-field extinction enhancements shown in figure 5.5(b) can be linked to the enhancements in the near-field intensity as discussed above and shown in figure 5.7. The simulated intensity enhancements at the resonance frequencies for the array and isolated particles (figure 5.4) are integrated and averaged over a full unit cell (dimensions 100 µm × 100 µm × 100 µm) for a range of particle lengths. This results in an average intensity enhancement (AIE) and is shown in figure 5.8. Figure 5.8(a) shows the AIE for the arrays of particles at each SLR frequency. The AIE of the array at the SLR frequency reproduces the trend of the far-field extinction shown in figure 5.5(b). For the array of particles with a length of 35 µm the coupling of the LR to the Rayleigh anomaly is the most efficient, and leads to an average enhancement of the field intensity in the full unit-cell which exceeds 2.5.

An AIE which is significantly larger than unity means that the structures in the simulation volume act like a cavity, where the incident electromagnetic wave resonates for a certain amount of time before it is either dissipated or re-radiated.

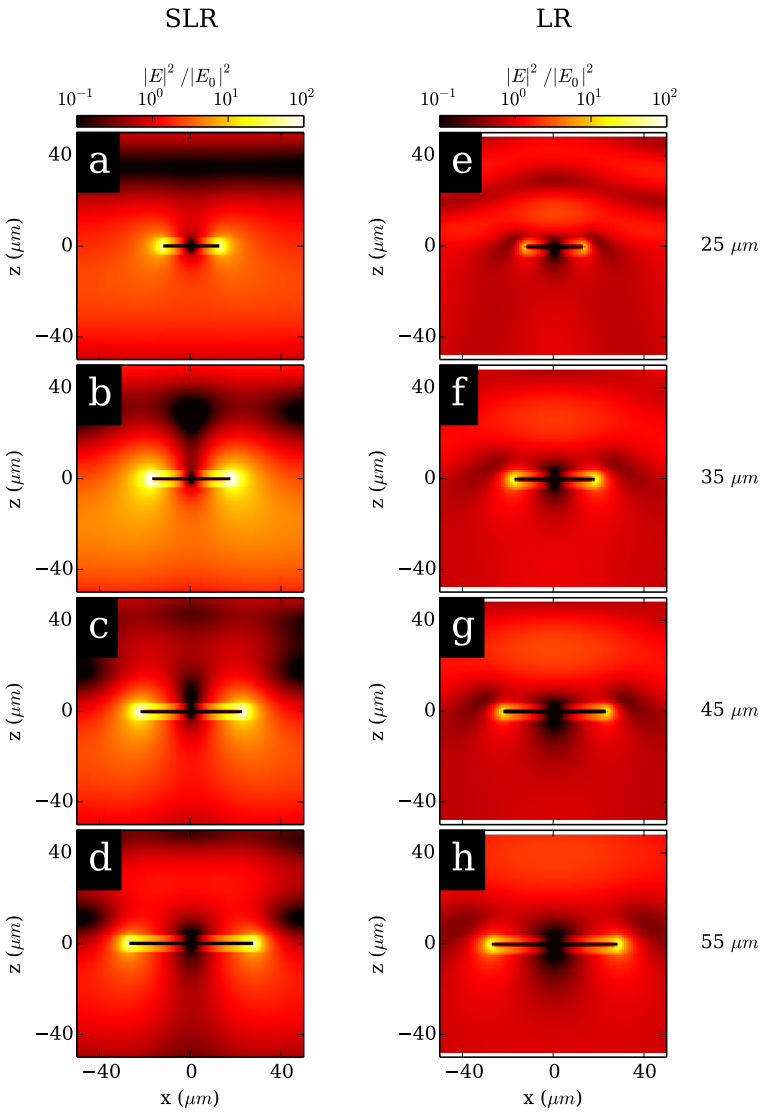

Figure 5.7: Near-field intensity enhancements simulated with FDTD. The fields are shown in the plane through the center of a particle, defined by the wavevector and the polarization of the incident field. The particles are symmetrically surrounded by amorphous quartz and a 6 µm thick lossy BCB bonding layer. The intensity enhancements are shown on a logarithmic color scale. The incident wave propagates in the $-z$ direction in the figures. From top to bottom the particle lengths are 25 µm, 35 µm, 45 µm and 55 µm. The pitch is 100 µm. Panels a-d are calculated at the frequency of maximum extinction of the SLR, panels e-h for the frequency of maximum extinction of the LR.

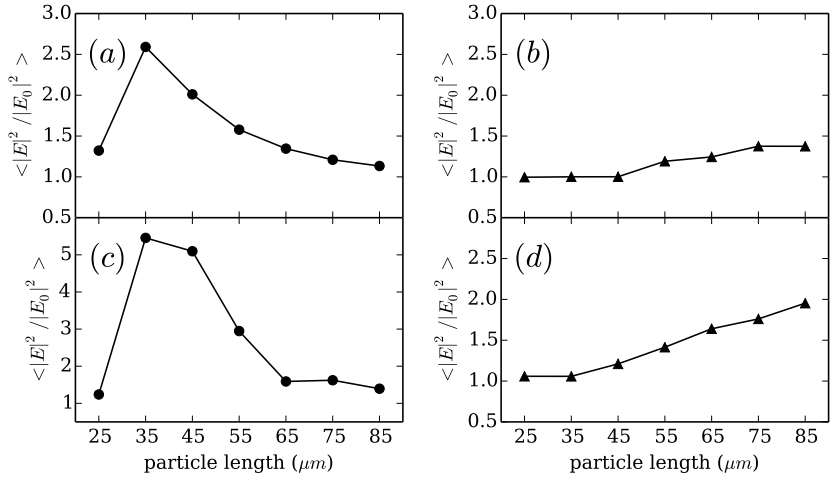

Figure 5.8: Average intensity enhancement simulated with FDTD in a unit cell of 100 µm × 100 µm × 100 µm for periodic arrays and isolated particles. Panel (a) shows results at the SLR resonance frequency in the Si particle arrays, panel (b) for the frequency of the LRs of the isolated particles. Panels (c) and (d) show the intensity enhancements at the SLR and LR frequencies for particles made out of a perfect metal.

The simulation for the isolated particle, for which the results are shown in figure 5.8(b), does not have a resemblance to a cavity, and as a result there is no significant AIE. The particle only redistributes the field, as opposed to the periodic lattice. There is a slight increase in the AIE as the particle length increases which can be explained as follows: The volume in which the LR enhances the electric field intensity scales with the particle length. For an increasing particle length the volume in which the field is enhanced becomes larger compared to the size of the integration volume. As a result the average field intensity increases. This biases the AIE for the isolated particles and explains the trend of figure 5.8(b).

For comparison the FDTD simulations discussed above are repeated for particles made out of a perfect electric conductor (PEC). Results for the AIE at the SLR and LR frequencies are shown in figures 5.8(c) and 5.8(d), respectively. Due to the reduced losses and larger scattering efficiency compared to the Si particles, the AIE is larger for the PEC particles. However, this difference is only a factor of two at maximum.

5.6 Photo-generated structures in a GaAs thin layer

In the previous sections of this chapter square arrays of As-implanted Si particles were considered. These arrays were fabricated by chemically etching, resulting in a permanent structure of Si between the quartz sub- and upperstrate. The following section discusses results of SLRs that are excited on a continuous and undoped thin layer of GaAs by photo-generating periodic structures that are projected with a spatial light modulator (SLM). As discussed in section 2.3 of this thesis the electrons in GaAs diffuse only a few micrometers during the time-scales of typical THz experiments. As a result the induced charge carriers are confined to the illuminated areas, and the projected image is translated into a spatial dependent local permittivity.

Experimental technique

The experimental setup used in this work is a modified version of the time-resolved THz time-domain spectrometer as introduced in section 5.2. The modification with respect to standard spectrometers [109] is in the optical pump arm as illustrated in figure 5.9. A horizontally polarized pump beam is sent in transmission through a polarizing beam splitter (PBS), after which the beam impinges at normal incidence on a spatial light modulator. The SLM is a pixelated LCD in which the birefringence of each pixel can be computer-controlled individually in 256 steps. On the return pass through the PBS, only pixels which rotate the polarization of the pump will be reflected by the PBS, directing this light onto the sample. The resolution of the projected image is limited by the pixel size of the SLM, which is 8×8 μm^2. This is highly sub-wavelength at THz frequencies. The sample used for the experimental results is a 1 μm thin layer of GaAs, symmetrically surrounded by mercapto-ester polymer bonding layers (40 μm) and a 1 mm sub- and upperstrate of amorphous quartz. The optical properties of this sample are discussed in section 2.2 of this thesis. An illustration of the sample is shown as an inset of figure 5.9.

Experimental results

Using the SLM, the GaAs sample is illuminated with a periodic lattice of squares. The dimensions of these squares are chosen in the range of 50 μm-110 μm. The pitch is chosen as 190 μm, which corresponds to a Rayleigh anomaly condition at 0.77 THz. A beam profiler has been used to examine the quality of the images projected onto the sample. Acquired images of these arrays are shown in figure 5.10. One can notice that the contrast in these images between the bright and the dark regions is finite. This is a result of the finite quality of the LCD, and a finite numerical aperture of the system projecting the image of the SLM onto the sample. When a periodic image is displayed the infrared pump beam will diffract upon reflection from the display. Since not all of the diffracted orders are collected by the imaging optics, the contrast is reduced and the background illumination is increased. The contrast between the bright and dark regions is estimated to exceed a factor of 40 in all the images shown.

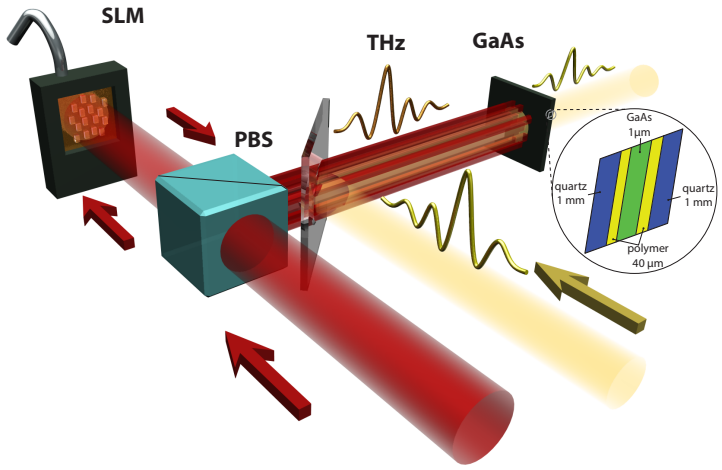

Figure 5.9: Illustration of the configuration used for the photo-excitation of GaAs, including the spatial light modulator (SLM). A horizontally polarized infrared pulse passes through a polarizing beam splitter (PBS) and reflects from the SLM. Computer controlled pixels can rotate the polarization of the pump beam over a range of angles. The PBS converts the polarization profile into an intensity profile, which is directed towards the sample in which the infrared pulse is absorbed. In the experiment the locally photo-excited sample is probed with a THz pulse. The inset shows, not to scale, a schematic representation of the cross section of the sample used for the experimental results presented in this chapter.

For the THz experiments the profiler is replaced by the sample containing the GaAs thin layer, and the pump fluence is increased such that the white regions in the projected images receive a maximum fluence of 60 $\mu J/cm^2$. The delay between the optical pump and the THz probe is set to 100 ps. The sample is measured in transmission, and each of the spectra for the photo-generated periodic arrays are referenced by a measurement in which the pump was blocked. The extinctions are normalized by the filling fraction of the illuminated areas. The resulting extinction efficiencies are shown in figure 5.11(a).

These spectra are characterized by a broad resonance, with a local minimum in the extinction at a frequency slightly blueshifted from the RA condition at 0.77 THz and a global maximum around 0.6 THz. As the length of the projected squares is decreased from 110 µm to 50 µm the resonance around this global maximum in the extinction becomes more narrow. This is consistent with the results discussed earlier

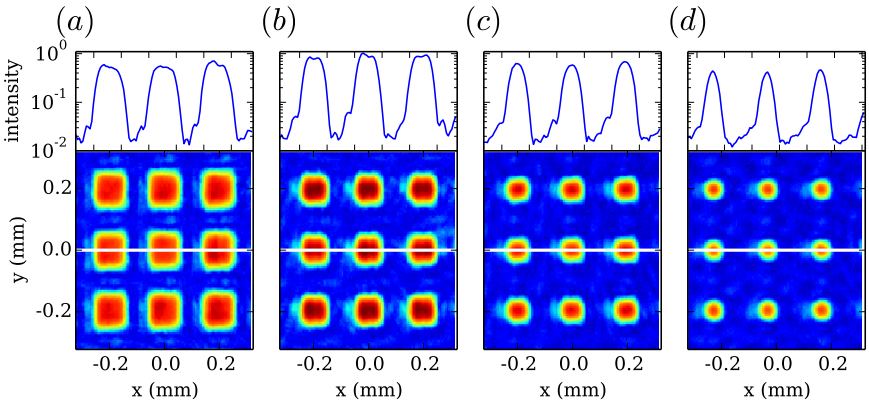

Figure 5.10: Intensity profiles of periodic arrays of photo-generated squares, with a pitch of 190 µm and square length of 110 µm (a), 90 µm (b), 70 µm (c) and 50 µm (d), respectively. The intensity profiles in the top panels are taken along the white lines in the lower panels. The intensity is normalized against the maximum intensity for a fully white image.

in this chapter and presented in figure 5.5(c). Additionally the extinction efficiency of the full spectra increases as the square length is reduced. This can be a result of a systematic under-estimation of the filling-fraction of the projected arrays. As can be seen in the profiler images the boundaries of the squares are not sharply defined, but have a finite gradient. For the normalization the full-width at half maximum in the intensity is used, but it is not unlikely that the effective length of the squares is slightly larger. An absolute under-estimation in the particle length has a larger relative effect on the extinction efficiency, which is consistent with the trend shown in figure 5.11(a).

Numerical simulations

The experimental results for the photo-generated periodic arrays are compared with numerical simulations (FDTD, Lumerical). The parameters for running these simulations have been chosen to match the experimental conditions as close as possible. The refractive indices for the quartz substrates and polymer bonding layers are those as determined in chapter 2, and the optical properties of the photo-excited GaAs are calculated with the Drude model using the parameters fitted to the experimental data presented in figure 2.11. Both lattice constant and dimensions of the photo-generated squares are taken from the profiler images as shown in figure 5.10. In the same profiler images it can be seen that the fluence on the sample has a finite gradient at the boundaries of the photo-generated squares. In the simulation volume this is accounted for by constructing the squares as 'onion' structures that consist of 3 concentric shells. In the center shell the carrier concentration is $N = 3.2 \times 10^{17}$ cm^{-3} and $\mu = 0.94$ m^{2}Vs, and the carrier concentration drops in each concentric ring by a

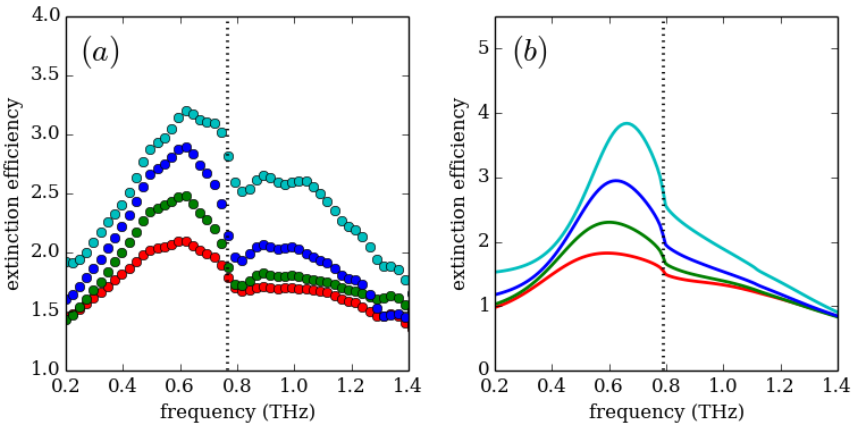

Figure 5.11: Experimental results (a) and numerical simulations (b) of the extinction efficiency for photo-generated square arrays with a fixed pitch of 190 µm, and square lengths of 110 µm (red circles/curve), 90 µm (green circles/curve), 70 µm (blue circles/curve) and 50 µm (cyan circles/curve). The vertical black dotted line indicates the frequency of the Rayleigh anomaly condition in the quartz substrate. For the simulations realistic parameters are used, including the 40 µm thick glue layers, a finite contrast between bright and dark regions and a gradient of charge concentration at the boundaries of the illuminated areas.

factor of 2. Figure 5.11(b) shows the results of these simulations. When comparing the results of these simulations to the experimental spectra presented in figure 5.11(a) there is an agreement on the main trends. There is a quantitative agreement with the experiments, as well in the extinction efficiency as in the resonance frequencies. The resonances are broad, and have their maximum around 0.6 THz. The minimum in extinction close to the RA condition is less pronounced in the simulations, and just slightly blueshifted from the RA condition as indicated by the vertical dotted black line.

Limitations

The experimental results for the periodic arrays shown in figure 5.11(a) present the main characteristics of diffractive coupling, but are also subject to a number of experimental limitations. In order to investigate these limitations and address an outlook for further improvements a number of FDTD simulations have been carried out. The simulations shown in figure 5.11(b) represent the experimental conditions as realistic as possible, where several parameters deviate from the optimum conditions for enhanced diffractive coupling as a result of restraints in the sample fabrication or imaging techniques. The spectra shown in figure 5.12(a) are results from FDTD simulations for an array of squares with dimensions of 110 µm in a lattice of 190 µm

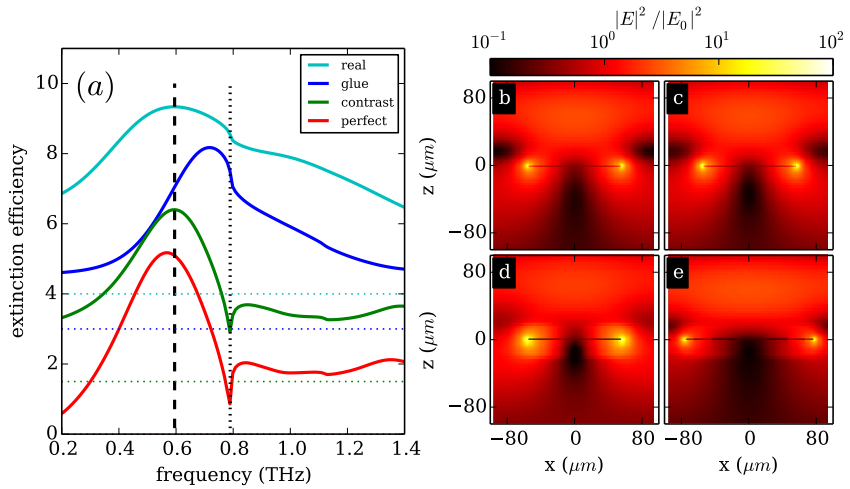

Figure 5.12: FDTD simulations of photo-generated squares with a length of 110 µm in a 190 µm square lattice, illustrating the cumulative contributions of several imperfections to the far-field spectrum and near-field enhancement of the intensity. Panel (a) shows the extinction efficiency for a system assuming a perfect sample (red curve), and introducing gradually a finite contrast in the intensity of 24 between the illuminated and dark regions (green curve), a 40 µm lossy glue layer at both sides of the GaAs thin film (blue curve) and a gradient in the carrier concentration at the illuminated boundaries (cyan curve). (b)-(e) Near-field profiles in the plane of the polarization and the wavevector through the center of each square for each of the samples: perfect (b), with finite contrast (c), including the polymer bonding layer (d) and with the gradient in the carrier concentration (e).

pitch where these restraints are introduced one-by-one. The red curve shows the spectrum for the ideal case where the GaAs thin film is directly in contact with the quartz substrates and no bonding polymer is present, and the projection of the image is such that there is an infinite contrast between the bright and the dark regions. Additionally the boundaries of the squares are sharp which allows for representing the illuminated regions with a single shell of $N = 3.2 \times 10^{17}$ cm^{-3}. The SLR is broad and the extinction has a well defined maximum. The minimum in extinction is pronounced and coincides with the RA condition. This behavior does not change significantly when a finite contrast of 24 is introduced between the bright and dark regions, as indicated by the green curve. The resonance broadens, and at low frequencies the extinction is increased. Although the carrier concentration is low, at these low frequencies the induced charge carriers introduce some losses. The blue curve represents the extinction spectrum after the introduction of the 40 µm thick mercapto-ester polymer glue layers at both sides of the GaAs thin film, of which

the complex refractive index is $\tilde{n} = 1.6 + 0.04i$. Due to the losses, but mainly as a result of the mismatch in refractive index from the substrate ($\tilde{n} = 2$), the diffractive coupling between particles is reduced and the pronounced minimum in the extinction disappears. The resonance frequency blueshifts, since the mode is distributed both over the quartz and the lower index glue. This also results in a small difference in frequency between the extinction minimum and the RA condition. The cyan curve represents the simulation with the realistic parameters as taken from the experiments, and corresponds to the red curve of figure 5.11(b). In this final step the perfect shape of the squares is replaced by one in which the carrier concentration gradually decreases in a set of concentric layers. This broadens the resonance, but also increases the effective length of the squares. As a result the resonance redshifts. Figures 5.12(b)-(e) show for each of the simulations described above a map of the near-field enhancement in the plane defined by the wave- and polarization vectors through the center of the squares.

5.7 Conclusions

In conclusion, we have experimentally investigated surface lattice resonances in periodic arrays of intrinsically doped Si particles at THz frequencies. As a function of the localized resonance frequency of the Si particles the mechanism of the coupling to a diffractive order has been studied. The experimental results can be reproduced with finite difference in the time domain (FDTD) simulations. The main results of the experiments and FDTD simulations are in agreement with the spectra calculated with a coupled dipole model. This coupled dipole model is used to explain the physics in terms of diffractive coupling, and relates the various contributions to the collective response. In order to link the intensity enhancement in the near-field to the enhanced extinction, the average intensity enhancement has been simulated.

We have also demonstrated the concept of active control of plasmonic effects in a continuous GaAs thin film through photo-excitation using a spatial light modulator. Periodic arrays of photo-imprinted squares result in extinction spectra that resemble a surface lattice resonance. The experimental results are compared against numerical simulations and were found to be in good agreement.

Chapter 6

Detuned and displaced dipoles

In a periodic lattice of dipoles the localized resonances (LRs) of these dipoles can scatter in the plane of the array. This condition is called the Rayleigh anomaly (RA), and the resulting surface lattice resonance (SLR) can be described as the coupling of the LRs to the RA. When a periodic lattice is formed out of a unit-cell which contains 2 dipolar scatterers two SLRs will be excited by the same RA, one from each dipole in the unit-cell. The interference between these two SLRs reshapes the collective extinction spectrum, as a function of the displacement between the dipoles. In this chapter the coupled dipole model as presented in previous chapters is extended to contain multiple dipoles per unit-cell. When the dipoles are detuned two distinct modes hybridize, which results in an additional maximum and an induced transparency window in the far-field extinction. The induced transparency window still exists when the scatterers are placed at an interface of air and quartz, which opens up opportunities for near-field experiments and potential sensing applications. The calculations are compared with numerical simulations and found to be in excellent agreement.

6.1 Introduction

Small scattering particles are among the most simple electromagnetic resonators. The resonances in these scatterers depend of the particle size, shape, orientation and material. Due to the presence of significant radiative losses these resonances are usually broad. One of the characteristics of a scatterer is the phase-change of the scattered field relative to the driving field when the frequency of the driving field changes from below the resonance frequency to above his frequency. This characteristic can be exploited to increase the complexity of the optical response of scatterers by having multiple scatterers interact with each other. Bozhevolnyi and coworkers demonstrated the existence of a transparency window in transmission for a system of two coupled and detuned dipoles at optical frequencies [147–149]. The mechanism was explained as destructive interference of the electromagnetic fields radiated into the far-field by these dipoles.

In a periodic lattice the broad localized resonances (LRs) of the particles can scatter into a diffraction order. When this diffraction order lies in the plane of the array a condition arises which is called a Rayleigh anomaly (RA). The Rayleigh anomaly is a very sharp resonance. When a broad mode couples to a sharp resonance a so-called Fano-resonance will appear, as discussed by Giannini et al. [150] for realistic plasmonic systems. For a periodic lattice such resonances are called surface lattice resonances (SLRs), which are introduced in chapter 1 and discussed in more detail in chapters 4 and 5 of this thesis. A periodic lattice with 2 dipoles per unit-cell combines the properties of interfering scatterers with the diffraction properties of the lattice. Bozhevolnyi and coworkers predicted theoretically and demonstrated in preliminary experiments that the selective scattering into, and suppression of diffractive orders in closely packed periodic arrays can be used for sensing applications. To our knowledge no literature exists where the arrays of detuned dipoles are designed such that the diffractive orders lie in the plane of the array and the resulting phenomena are explained as the interference of multiple SLRs. As for the studies of Bozhevolnyi et al, typical studies on THz metamaterials favor periodic lattices with filling fractions such that the RA conditions lie outside of the spectral region of interest [138, 151].

In this chapter we study with a rigorous approach the extinction properties of arrays of detuned and displaced dipoles. A theoretical model is developed and presented in section 6.2, extending the coupled dipole model (CDM) approximation presented in chapter 4. This model is used in section 6.3 to study the extinction spectra of 1D chains of perfect metallic ellipsoids for systems where the dipoles in each unit cell are either identical or detuned. In section 6.4 the coupled dipole calculations are compare with numerical simulations using the finite-difference in the time-domain method. In order to make a representative design for experimental verification a simulation has been carried out for the scatterers on a quartz-air interface. The chapter is ended with conclusions.

6.2 Theoretical model

The extinction cross section of an ensemble of metallic scatterers is related to the amount of work an incident electromagnetic wave does while driving the conducting electrons of these scatterers. As mentioned in section 1.3 this cross section can be expressed in terms of the wavenumber k, the polarization $\mathbf{p}_i$ of the i^{th}-scatterer and the incident field $\mathbf{E}_i^{\text{inc}}$ according to [46]

$$C_{\text{ext}} = 4\pi k \sum_i \frac{\text{Im}(\mathbf{E}_{\text{i}}^{\text{inc}} \cdot \mathbf{p}_{\text{i}})}{|\mathbf{E}_i^{\text{inc}}|^2} \ . \tag{6.1}$$

The polarization in turn, depends on the incident field, the properties of the scatterer like material, shape and orientation, and for an ensemble of scatterers their relative arrangement. The properties of the scatterer are described by the polarizability tensor α, relating the polarization and the local field as $\mathbf{p}_i = \alpha_i \mathbf{E}_i^{\text{loc}}$.

Coupled dipole model for displaced dipoles

In an ensemble of scatterers the local field at each scatterer i is the sum of the incident field, $\mathbf{E}_i^{\text{inc}}$, and the field scattered by all other scatterers, $\mathbf{E}_i^{\text{sca}}$:

$$\mathbf{p}_i = \alpha_i \mathbf{E}_i^{\text{loc}} = \alpha_i (\mathbf{E}_i^{\text{inc}} + \mathbf{E}_i^{\text{sca}}) \ . \tag{6.2}$$

The interaction through scattering between two sub-wavelength scatterers can be approximated with the dipole-dipole interaction tensor $\text{G}(\mathbf{r})$. Taking the sum over all dipoles gives

$$\mathbf{E}_i^{\text{sca}} = \sum_{j \neq i} G(\mathbf{r}_i - \mathbf{r}_j)\mathbf{p}_j \ , \tag{6.3}$$

where the dipole-dipole interaction tensor in differential form is defined as

$$G(\mathbf{r}) = (k^2 + \nabla\nabla)\frac{e^{ikr}}{r} \ . \tag{6.4}$$

In an infinite periodic lattice that is illuminated by a plane-wave the behavior of all unit cells is identical over the full array, and similar scatterers will have similar polarizations. When each unit cell contains two -not necessarily similar- scatterers the sum over all dipoles in equations (6.1) and (6.3) can be split into two contributions: one accounting for the interaction with all like dipoles, and one accounting for the interaction with all unlike dipoles. Figure 6.1 shows an illustration of such a lattice, and if we label the dipoles either $\circ$ or $\bullet$ we can express the polarizabilities as

$$\mathbf{p}_\circ = \alpha_\circ \left[\mathbf{E}_\circ^{\text{inc}} + \sum_{j \in \circ} G_{\circ,j}\mathbf{p}_\circ + \sum_{j \in \bullet} G_{\circ,j}\mathbf{p}_\bullet \right] \ , \tag{6.5}$$

and

$$\mathbf{p}_\bullet = \alpha_\bullet \left[\mathbf{E}^{\text{inc}}_\bullet + \sum_{j\in\bullet} G_{\bullet,j}\mathbf{p}_\bullet + \sum_{j\in\circ} G_{\bullet,j}\mathbf{p}_\circ \right] . \tag{6.6}$$

Equations (6.5) and (6.6) can be re-written in matrix form, where the matrix A accounts for the diffractive coupling,

$$\mathbf{E}^{\text{inc}} = A\mathbf{P} . \tag{6.7}$$

More explicitly

$$\begin{pmatrix} \mathbf{E}^{\text{inc}}_\circ \\ \mathbf{E}^{\text{inc}}_\bullet \end{pmatrix} = \begin{pmatrix} \alpha_\circ^{-1} - S_{\circ\circ} & -S_{\circ\bullet} \\ -S_{\bullet\circ} & \alpha_\bullet^{-1} - S_{\bullet\bullet} \end{pmatrix} \begin{pmatrix} \mathbf{p}_\circ \\ \mathbf{p}_\bullet \end{pmatrix} . \tag{6.8}$$

Each of the S matrices contains a lattice sum which is defined as

$$S_{AB} = \sum_{j\in B} G_{A,j}\mathbf{p}_B , \tag{6.9}$$

where A and B correspond to either $\circ$ or $\bullet$. Solving the above equations for $\mathbf{P}$, and applying eq. (6.1) the total extinction cross section of both the dipoles in the unit cell can now be expressed as

$$C_{\text{ext}} = 4\pi k \,\text{Im}\left(\frac{2\text{S}_{\circ\circ} - 2\text{S}_{\circ\bullet} + \alpha_\circ^{-1}\alpha_\bullet^{-1}}{\text{S}^2_{\circ\circ} - \text{S}^2_{\circ\bullet} - (\alpha_\circ^{-1} + \alpha_\bullet^{-1})\text{S}_{\circ\circ} + \alpha_\circ^{-1}\alpha_\bullet^{-1}} \right) . \tag{6.10}$$

The most simple periodic structure is a one-dimensional chain. When such a chain is illuminated such that the incident wave vector is parallel to one of the cardinal axes of each ellipsoid, and the polarization direction is orthogonal to the direction of the chain, the scalar approximation for the polarizability and fields can be used. Under these conditions the dipole interaction tensor $G(\mathbf{r})$ reduces to [133]

$$G(r) = \exp(ikr)\left(\frac{ik}{r^2} - \frac{1}{r^3} + \frac{k^2}{r} \right) , \tag{6.11}$$

in which r is the distance between the respective dipoles. The scalar approximation is justified, since as a result of symmetry, the polarization of the particles is always parallel with the polarization of the incident field. The diffractive coupling will, in general, significantly affect the overall extinction spectrum compared to the response from the particles without any interaction.

Polarizibility of an isolated particle

The results that will be presented in this chapter are calculated for particles that are perfectly metallic, i.e. $\text{Re}(\tilde{\epsilon}) \to -\infty$. Under this condition the static polarizability reduces to

$$\alpha_y^{\text{static}} = \frac{V}{3L_y} . \tag{6.12}$$

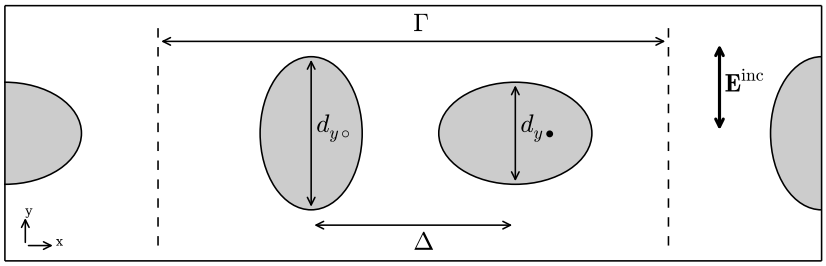

Figure 6.1: Illustration of two displaced and detuned dipoles in a periodic chain. The pitch of the chain is Γ and the displacement of the dipoles is Δ. The dipoles have an identical cross-section, but are detuned in resonance frequency as a result of the difference in length d_y parallel to the incident field $\mathbf{E}^{\mathrm{inc}}$.

For spherical particles the shape factor L_y is equal to 1/3 for the three particle axes, while it deviates from this value for oblate and prolate spheroids. For scatterers of finite size dynamic depolarization and radiative damping influence the polarizability. In the modified long wavelength approximation [46], which holds for particles of subwavelength dimensions, the polarizability can now be written as

$$\alpha_y = \frac{1}{\frac{3L_y}{V} - \frac{2}{3}ik^3 - \frac{2k^2}{d_y}} \,. \tag{6.13}$$

This is an important result since it is, for a given wavevector, completely characterized by the particle shape and orientation and no material properties are present.

6.3 Calculations

Scattering from an isolated dipole

Before the results for systems of interacting dipoles are discussed, it is instructive to have a look at the extinction spectra of isolated particles and how they correlate with the particle geometry. Figure 6.2 shows extinction spectra for perfect metallic oblate spheroids with varying lengths, but where the geometrical cross section is kept constant at 8000π μm^2. All particles have the same height of 0.1 μm and are illuminated at normal incidence polarized along the y-direction, which is the long axis of the ellipsoid. The extinction cross sections are normalized against the geometrical cross section of 300 μm × 300 μm. This area corresponds to the cross section of a unit cell in the arrays investigated in the following sections. This normalization, resulting in extinction spectra, is not to be confused with the extinction efficiencies presented in chapters 4 and 5 of this thesis where the extinction cross sections were normalized against the geometrical cross sections of the scatterers. The extinction spectra calculated for a range of aspect ratios is shown in figure 6.2(a), where the

dashed blue curve corresponds to a particle with dimensions 200 µm × 40 µm, and the magenta curve to a particle with a length of 112 µm × 71 µm. For each particle a single, well-defined resonance can be resolved. The resonance is broad due to the large radiation losses due to the oscillating charges. As the aspect ratio decreases, the length of the particle along the direction of the polarization decreases as well. As a consequence the maximum of the extinction shifts to higher frequencies. The change in magnitude of the resonance is a result of the change in the form factor L. Figure 6.2(b) shows in a 2D color plot the extinction spectra, both as a function of frequency, and on a logarithmic scale the particle length. Both the blueshift of the resonance frequency as well as the reduction of the extinction as the aspect ratio is reduced are clearly visible. The resonance frequency is indicated by the black curve, and scales inversely with the length of the scatterer d_y.

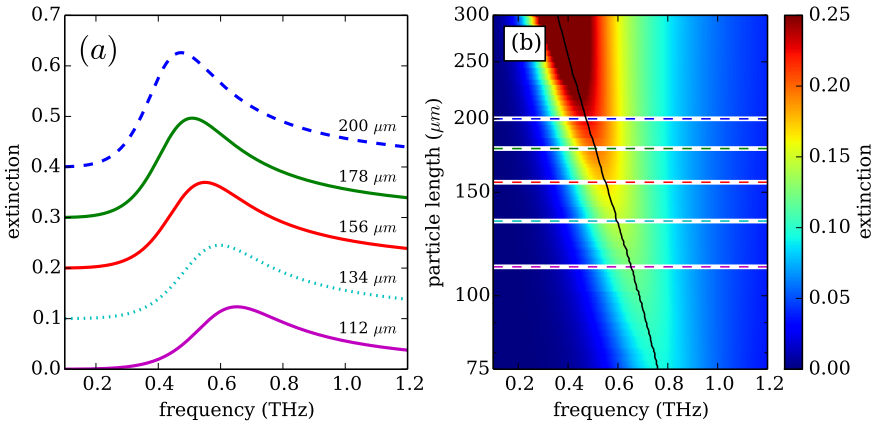

Figure 6.2: Extinction spectra of oblate spheroidal particles surrounded by an index $n = 2$ environment as calculated in the MLWA approximation. All particles have a height of 0.1 µm, and a geometrical cross section of 8000π µm^2. The extinction cross sections are normalized to an area of 300 µm × 300 µm. (a) Spectra for particles with a length along the polarization direction ranging from 200 µm (dashed blue curve) to 112 µm (magenta curve). (b) Extinction spectra for particle lengths ranging from 75 µm to 300 µm, where the dashed lines correspond to the spectra shown in (a). The black curve indicates the extinction maximum.

Extinction of two detuned dipoles

When two particles are brought into close proximity mutual radiative coupling will affect the scattering properties of the ensemble. For two dipoles this is illustrated with CDM calculations in figure 6.3. In figure 6.3(a) the LRs for scatterers with dimensions of 200 µm × 40 µm and 50 µm × 160 µm are shown with the black dotted and dashed curves, respectively. These resonances are significantly detuned as a result

of the large difference in length along the direction of polarization. The incoherent sum of these two scatterers is indicated with the solid black curve, and represents the extinction cross section of the two particles when any form of coupling or interference is neglected. The colored curves represent extinction spectra for these two dipoles when they are placed in proximity of each other and the radiative coupling is taken into account. This is illustrated in figure 6.1 when the dipoles outside the vertical dashed lines are omitted. Each curve corresponds to a different separation Δ between the scatterers, changing the relative phase of the scattered light that couples the dipoles. The blue curve is for a separation between the centers of the scatterers of 75 µm, which means that the two particles are overlapping. The green curve represents a separation of 110 µm. At this separation the ratio between the maximum in extinction around 0.9 THz and the extinction at the local minimum is the largest. The red curve corresponds to a separation of 133 µm, containing the global maximum in the extinction at 0.81 THz. For a separation of 200 µm, indicated with the cyan curve, the coupling between the dipoles is such that the two resonances have merged into a single broad resonance. Figure 6.3(b) shows the development of the extinction spectra as a function of the separation between the dipoles on the vertical axis in a color plot. The dashed horizontal lines correspond to the separations as shown for figure 6.3(a).

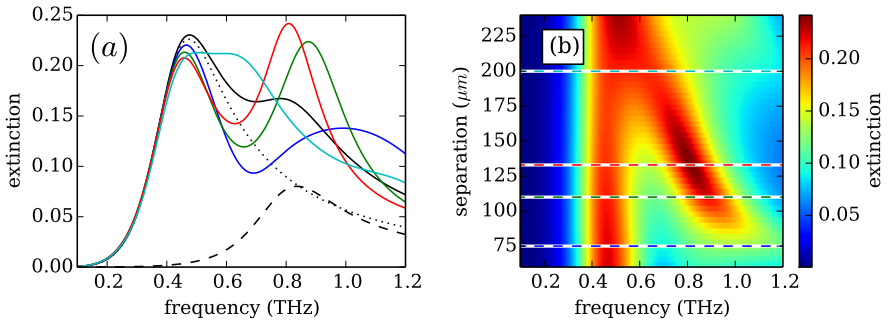

Figure 6.3: Extinction spectra for two detuned dipoles, calculated with the CDM representing scatterers with dimensions of 200 µm × 40 µm and 50 µm × 160 µm for a range of separations. Panel (a) shows spectra for separations of 75 µm (blue curve), 110 µm (green curve), 133 µm (red curve) and 200 µm (cyan curve). The black dotted and dashed curves represent the LRs of either isolated particle and the solid black curve is their incoherent sum. Panel (b) shows in a color plot the extinction spectra of the two coupled dipoles as a function of the separation. The dashed horizontal lines match the separations for which the spectra are shown in panel (a). All particles are surrounded symmetrically by an index $n = 2$ environment.

Displaced identical dipoles in a lattice

The response of a particle with dimensions of 200 μm × 40 μm is shown again in figure 6.4(a) and indicated with the black dashed curve. This is the same spectrum as the blue dashed curve from figure 6.2(a). When a 1D periodic chain of these particles is formed, the spectrum is altered as a result of diffractive coupling. The solid black curve in figure 6.4(a) represents the extinction spectrum for a chain with a pitch of $\Gamma = 300$ μm in the direction of the short axis of the particles (along the x-axis of figure 6.1). The incident field is at normal incidence, and polarized perpendicular to the direction of the chain, and parallel to the long axis of the particles. This lattice has the RA condition at 0.5 THz as indicated by the vertical dotted black line. As explained in more detail in chapters 4 and 5 of this thesis at this condition the polarizations of the dipoles in the lattice are out of phase with the incident field, and as a result the extinction at this frequency is minimized. At somewhat lower frequencies however the dipoles and incident field are in phase, and the extinction is greatly enhanced. This is the characteristic response of a surface lattice resonance (SLR).

The interaction between the scatterers in the lattice changes when a second particle is added to the unit cell which is identical to the first. This is illustrated in figure 6.1 when assumed that all the dipoles sketched in this figure have the same dimensions and orientation. The ensemble of scatterers can be interpreted as two lattices which are displaced from each other by a finite distance Δ. The SLRs that are excited in both lattices will interfere with a certain difference in phase depending on the relative displacement of the two lattices. As a consequence the resulting extinction spectra will depend not only on the lattice constant Γ, but also on the relative displacement of the two dipoles Δ. Extinction spectra are shown in figure 6.4(b) for displacements of 150 μm (blue curves), 100 μm (green curves) and 75 μm (red curves), respectively. The solid curves represent the extinction of a lattice of displaced dipoles, the dashed curves are calculated for just 2 identical displaced dipoles. For convenience some of the spectra are off-set vertically as indicated by the horizontal dotted lines. When the particles are displaced by 150 μm the displacement is half of the lattice constant, i.e. $\Delta = \Gamma/2$. Effectively the periodicity of the chain doubles and the lowest diffraction order shifts to 1 THz. This is in correspondence with the calculations as the solid blue curve in figure 6.4(b) is smooth around 0.5 THz, and resembles the spectrum of just two dipoles. This symmetry is broken when the dipoles are displaced over distances not matching this condition, as can be seen for the 100 μm and 75 μm displacements. In both cases a clear SLR is visible around the RA condition. Note though that the extinction maximum is shifted to high frequencies when compared to the lattice where the unit cell just contains a single particle.

The color plots in figures 6.4(c) and 6.4(d) illustrate in more detail the effect of the lattice on the extinction spectrum when the distance between the two dipoles in the unit-cell is varied. Figure 6.4(c) shows the response of two identical coupled dipoles. For displacements Δ in the range of 60 μm-125 μm the extinction spectrum is characterized by a broad resonance, which in first order corresponds to the spectrum of the LRs of the isolated particles. When the displacement is increased, a maximum

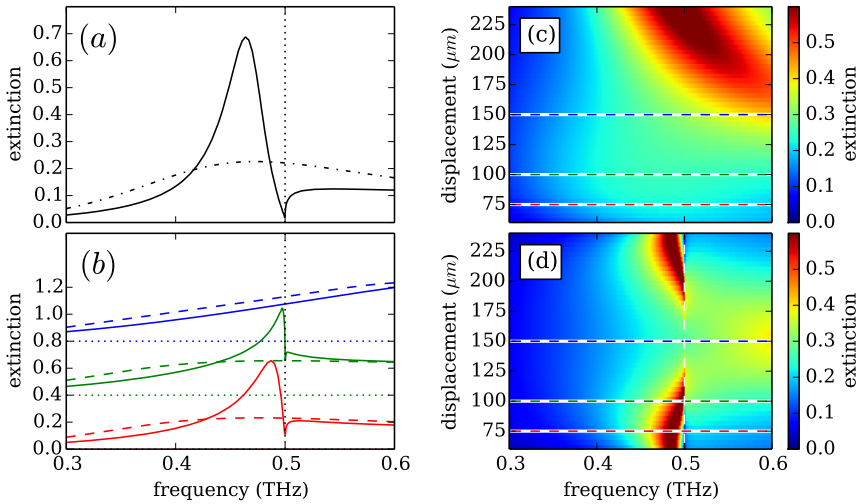

Figure 6.4: (a) Extinction spectra of a perfect metal particle with dimensions of 200 μm × 40 μm, in a 1D lattice with a pitch of $\Gamma = 300$ μm (solid curve), and as an isolated particle (dashed curve). The vertical dotted line indicates the RA condition at 0.5 THz. (b) Extinction spectra for a 1D lattice with a pitch of $\Gamma = 300$ μm containing 2 identical dipoles, displaced by 150 μm (blue curve), 100 μm (green curve) and 75 μm (red curve). The spectra are vertically off-set for convenience as indicated by the dotted lines. The dashed curves indicate the extinction spectra of 2 identical dipoles in the absence of any lattice. (c) Extinction spectra for 2 identical dipoles as a function of the displacement. The dashed lines mark the displacements of the dashed curves in panel (b). (d) Extinction spectra for 2 identical dipoles in a 1D lattice as a function of the displacement. The RA condition is indicated by the white dashed line and the horizontal dashed lines correspond to the cuts shown in (b) by the solid curves. The particles are surrounded by an environment with a refractive index of $n = 2$, and the calculation is done for a lattice containing 2000 unit cells.

in the extinction appears at higher frequencies, which redshifts as the displacement is further increased. The wavelength in the surrounding medium at this frequency matches the displacement, and indicates that the scattered field from one particle interferes constructively with the incident field on the other. Destructive interference between scattered and incident fields explains the extinction reduction at lower frequencies.

The response of the lattice of identical displaced dipoles (figure 6.4(d)) is symmetric around $\Delta = 150$ μm, and visualizes how in the range of frequencies shown the spectrum of a $\Gamma = 300$ μm lattice transforms into a lattice with $\Gamma = 150$ μm. For small displacements there is a pronounced SLR just slightly redshifted from the RA condition at 0.5 THz. Increasing the displacement causes the SLR to blueshift, reduce in amplitude and eventually disappear. For each displacement Δ the distance

of a dipole to the dipole in the neighboring unit cell is $\Gamma - \Delta$. These distances are interchangeable for the diffractive coupling, which explains the symmetry at $\Delta = 150$ µm.

Displaced and detuned dipoles in a lattice

The same analysis as for 2 identical dipoles can be carried out for an ensemble of dipoles which are detuned in their resonance frequency and strength, as illustrated in figure 6.1. For this purpose the dimensions of one of the dipoles used in the calculations of this section are changed to 134 µm × 60 µm which blueshifts the localized resonance, while the dimensions of the other dipole are kept at 200 µm × 40 µm. These dimensions are chosen such that while the localized resonance of the 200 µm long particle is redshifted from the RA condition, the localized resonance of the 134 µm long particle has its maximum at higher frequencies than the RA. This is shown in figure 6.5(a) by the dashed magenta and dotted cyan curves respectively. As a consequence of the detuning of the localized resonances of the two dipoles forming the unit cell, the surface lattice resonances are detuned as well when either of the dipoles is placed in a periodic 1D chain. Both SLRs still have a minimum in the extinction at the RA condition, but the extinction maxima are clearly detuned. The incoherent sum of these two SLRs is shown with the solid black curve in figure 6.5(a).

When the coupling between the detuned dipoles in the lattice is considered two trends can be discerned. Extinction spectra are shown in figure 6.5(b) for the same displacements as in figure 6.4(b) which are $\Delta = 150$ µm, $\Delta = 100$ µm and $\Delta = 75$ µm. The dashed curves represent the two interacting dipoles, while the solid curves represent a lattice with 300 µm pitch. The behavior around the RA condition shows a similar trend as for the identical dipoles: the SLR disappears when the displacement approaches $\Gamma/2$. Different from the case when the dipoles are identical, is the appearance of another resonance slightly redshifted from the RA condition. In between this maximum and the RA condition a transparency window opens up. The frequency of the additional resonance is much lower than either the RA condition or the SLRs presented in figure 6.5(a), and is a direct result from coherent interference between the two SLRs launched from the sub-lattices containing either particle in their unit-cell.

A more complete view of how the extinction spectra behave as a function of the displacement is shown in figures 6.5(c) and (d), for just the two dipoles and the lattice of detuned dipoles, respectively. The response for the two detuned dipoles differs from the response of the identical dipoles shown in figure 6.4(c) mostly on details. The most pronounced is the reduced overall magnitude of the extinction at the resonance condition. This can be directly related to the reduced scattering cross section of the detuned dipole in the frequency range shown. Figure 6.5(d) clearly shows for the lattice of detuned dipoles how, as for the identical dipoles, the resonance around the RA condition (indicated with the white dashed line) vanishes when the displacement approaches 150 µm. Although the maximum in extinction is in the same order, compared to the identical dipoles the coupling to the diffraction order seems

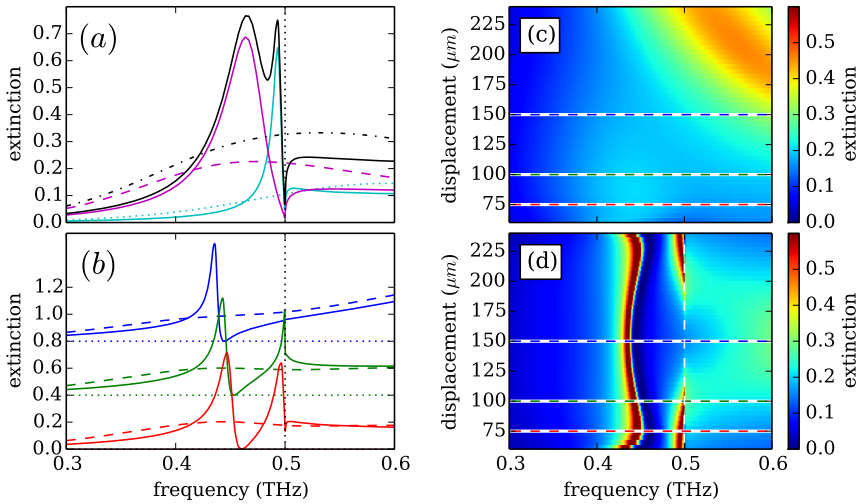

Figure 6.5: (a) Extinction spectra of a 1D lattice with a pitch of $\Gamma = 300$ μm for particle dimensions of 200 μm × 40 μm (solid magenta curve) and 134 μm × 60 μm (solid cyan curve), with the solid black curve their incoherent sum. The dashed/dotted curves indicate the corresponding spectra for the LRs while the vertical dotted line represents the RA condition at 0.5 THz. (b) Extinction spectra for a 1D lattice with a pitch of $\Gamma = 300$ μm containing the 2 detuned dipoles, displaced by 150 μm (blue curve), 100 μm (green curve) and 75 μm (red curve). The spectra are vertically off-set for convenience as indicated with the dotted lines. The dashed curves are extinction spectra of the two detuned dipoles in the absence of any lattice. (c) Extinction spectra for 2 detuned dipoles in the absence of a lattice, as a function of the displacement. The dashed lines mark the displacements of the spectra shown in (b). (d) Extinction spectra for 2 detuned dipoles in a 1D lattice as a function of the displacement. The RA condition is indicated by the vertical white dashed line and the horizontal dashed lines correspond to the cuts shown in (b). The particles are surrounded by an environment with a refractive index of $n = 2$, and the calculation is done for a lattice containing 2000 unit cells.

to be suppressed for a broader range of displacements. The additional resonance at lower frequencies, and corresponding transparency window is clearly present for all displacements. The exact frequency of this resonance however varies as a function of the displacement.

S-parameters

The suppression of the SLR at the RA condition as shown above can be understood by having a closer look at the S parameters as defined in equations (6.9) and (6.10). For a lattice of 2000 unit cells the S parameters are calculated for displacements of 75 µm ($\Gamma/4$) and 150 µm ($\Gamma/2$). The black curves in figure 6.6 (a) and (b) show the real (solid) and imaginary (dashed) components of $S_{\circ\circ}$. These terms are independent of the displacement between the two dipoles in the unit-cell and only depend on the periodicity of the lattice. The $S_{\circ\bullet}$ terms however depend both on the periodicity and the displacement of the dipoles in the lattice. The spectra for a displacement of 150 µm are shown in figure 6.6 (a), whereas the spectra of $S_{\circ\bullet}$ for a displacement of 75 µm are presented in figure 6.6(b). The real component of $S_{\circ\circ}$ has a maximum at the RA condition at 0.5 THz and the imaginary component of $S_{\circ\circ}$ has a discontinuity in which it switches sign from negative to positive for increasing frequency. When we now compare the $S_{\circ\bullet}$ term for a displacement of 150 µm (blue curves in figure 6.6 (a)) we can notice that around the diffraction order $S_{\circ\circ}$ and $S_{\circ\bullet}$ are comparable in magnitude but opposite in sign. This can be interpreted as the diffractive effects of the two superimposed lattices being exactly out of phase.

In terms of these S parameters, the spectra for identical displaced dipoles in a lattice can be explained as follows: In this case all polarizabilities are identical and as a result $\alpha_\circ = \alpha_\bullet$, equation 6.10 can be simplified to

$$C_{\text{ext}} = 4\pi k \,\text{Im}\left(\frac{2\text{S}_{\circ\circ} - 2\text{S}_{\circ\bullet} + \alpha_\circ^{-2}}{\text{S}_{\circ\circ}^2 - \text{S}_{\circ\bullet}^2 - 2(\alpha_\circ^{-1})\text{S}_{\circ\circ} + \alpha_\circ^{-2}}\right) . \tag{6.14}$$

At the RA, when $S_{\circ\circ} = -S_{\circ\bullet}$, all contributions from diffractive coupling drop out of the equation and we are left with

$$C_{\text{ext}} = 8\pi k \,\text{Im}(\alpha_\circ) . \tag{6.15}$$

The mechanism for suppressing diffraction orders in arrays of displaced dipoles as introduced above is in principle more general. The relation between the displacement Δ and the pitch Γ for the order m to be suppressed is

$$\Delta = \Gamma\frac{i - 1/2}{m}, \text{ where i} = 1, 2..\text{m} \tag{6.16}$$

which holds for all higher orders. In practice however these higher orders become of less relevance, since at very high frequencies the MLWA breaks down and the coupled dipole model as discussed here is no longer valid. It is interesting to note though that it is not necessary for the two dipoles to be identical, as we can learn from the spectra indicated by the blue curves in figures 6.6(c) and 6.6(d). The spectrum becomes smooth around the RA condition both for the identical dipoles (figure 6.6(c)) as for the detuned dipoles (figure 6.6(d)), even though in the latter case the localized resonances of the individual dipoles differ in the magnitude of the extinction.

The spectra of $S_{\circ\bullet}$ for a displacement of 75 µm are smooth around the RA condition, and it is therefor not possible to compensate the effect of the RA as present

in the spectra of $S_{\circ\circ}$. This is confirmed by the spectra indicated with the red curves in figures 6.6(c) and 6.6(d).

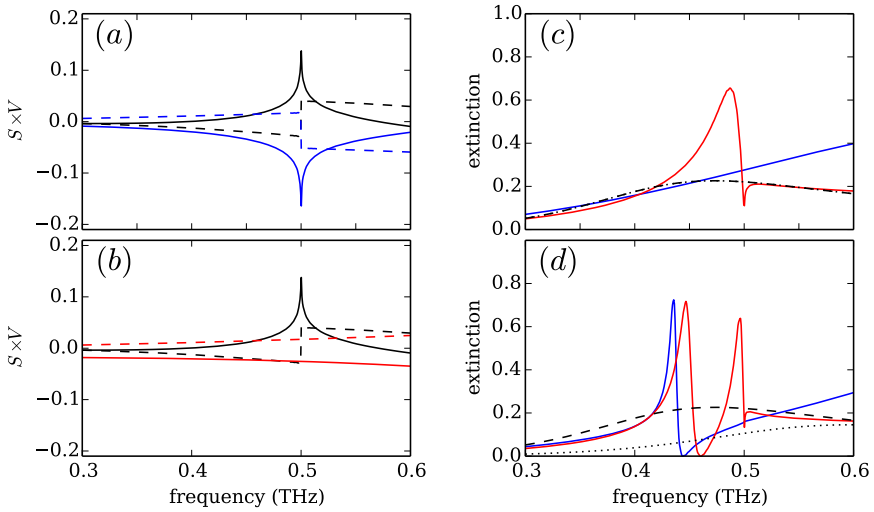

Figure 6.6: (a) and (b) For a 1D lattice of $\Gamma = 300$ μm pitch: real (solid curves) and imaginary (dotted curves) components of $S_{\circ\circ}$ (black curves) and $S_{\circ\bullet}$ for a displacement of 150 μm (blue curves) and a displacement of 75 μm (red curves). (c) Extinction spectra for the identical dipoles and (d) the detuned dipoles. The LRs of the isolated particles are indicated with the black dashed and dotted curves, the solid curves represent the spectra for the 1D lattice. The blue curves represent a displacement of 150 μm and the red curves a 75 μm displacement.

Hybridization

The characteristic shape of the spectra of a lattice of displaced dipoles can be understood as an interference between the SLRs that are launched from both the dipoles in the lattice. In case the dipoles are detuned and one of the LRs is redshifted from the RA condition, the resulting mode can be understood as a hybridization two modes: One resembling a lattice with two displaced identical dipoles, and the SLR of a chain containing only a single dipole in the unit-cell. This is presented in the results of figure 6.7.

In figure 6.7 we investigate the extinction spectra of a lattice of displaced and detuned dipoles as a function of the detuning between the displaced dipoles. The localized resonance of one of the dipoles is constant, corresponding with a ellipsoid of 200 μm × 40 μm, while for the other particle the aspect ratio is varied. Results are shown for 2 cases: a displacement of 100 μm (figures 6.7(a) and (b)) where the SLR is not suppressed at the RA condition, and a displacement of 150 μm (figures 6.7(c)

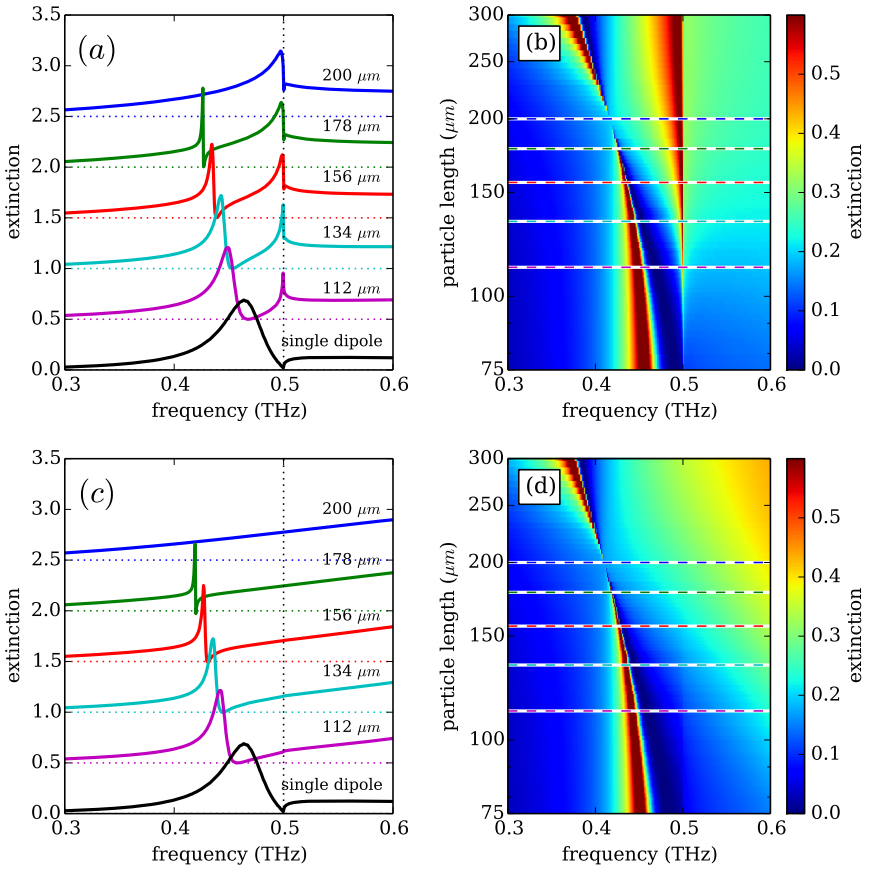

Figure 6.7: Extinction spectra for a 1D lattice of detuned dipoles as a function of the detuning, which is achieved by decreasing the length of one of the dipoles but keeping the geometrical cross-section constant. This length is indicated in the figures. The other dipole corresponds to a particle with dimensions of 200 µm × 40 µm, which means that the blue curves represent identical displaced dipoles. Results are shown for displacements of 100 µm (a) and (b), and 150 µm (c) and (d). Figures (a) and (c) show cuts of figures (b) and (d) respectively, and the curves are off-set vertically for convenience as indicated by the horizontal dotted lines, and the vertical dotted lines indicate the RA condition at 0.5 THz.

and (d)) where the condition is such that SLR does vanish at the RA condition.

The spectra for a 100 µm displacement show in figure 6.7(a) that when the dipoles are identical (blue curve) a single resonance is present, located at the RA condition of 0.5 THz. When the aspect ratio of one of the scatterers is reduced, i.e. the axis parallel to the polarization is shortened and the perpendicular axis is enlarged, the dipoles become detuned and an additional resonance appears redshifted from the RA. This is clearly visible for the green to magenta curves in figure 6.7(a). As one of the dipoles is detuned, the localized resonance shifts to higher frequencies and gets reduced in amplitude, as shown in figure 6.2. In the limit of a very large detuning, these detuned particles do no longer contribute to the extinction spectrum and the response converges to that of a lattice with only the non-detuned scatterer. The latter is indicated in the figure by the black curve. Figure 6.7(b) shows the same results, but in a 2D color plot, with the length of the detuned dipole on the vertical axis on a logarithmic scale. This length is parallel to polarization of the incident field. The length for which the scatterers are identical is 200 µm, which is indicated by the dashed blue line. The colored horizontal dashed lines match the spectra shown in figure 6.7(a).

The spectra for a displacement of 150 µm show a very similar trend as a function of the detuning. The evolution of the resonance is nearly identical to that of the lower branch of the 100 µm displacement. The upper branch is absent, since this mode is forbidden by symmetry.

6.4 Numerical simulations

In order to extend the model to a system that can be experimentally verified, numerical simulations have been carried out using the finite-difference in the time-domain method (FDTD, Lumerical). The scatterers are defined as cylindrical disks consisting of a perfect electric conductor (PEC), and the illumination with a broadband THz pulse is at normal incidence. The unit-cell contains either a single scatterer or a pair of scatterers, and is surrounded by perfectly matched layers (PMLs) at all sides for the simulations of the localized resonances of the individual scatterers, or the isolated pair of scatterers. In the simulations for the 1D chains the PMLs in one of the directions are replaced by Bloch-periodic boundary conditions. The disks have a height of 0.1 µm. The exinction is calculated by normalizing the total power of the scattered field by the power of the source over the cross section of the unit cell, which is 300 µm × 300 µm. In the simulations the scatterers are illuminated from the side of the substrate, which has always a refractive index of $n = 2$. The superstrate has a refractive index of either $n = 2$, representing a symmetrically surrounded scatterer, or a value of $n = 1$ for a scatterer at an air/quartz interface.

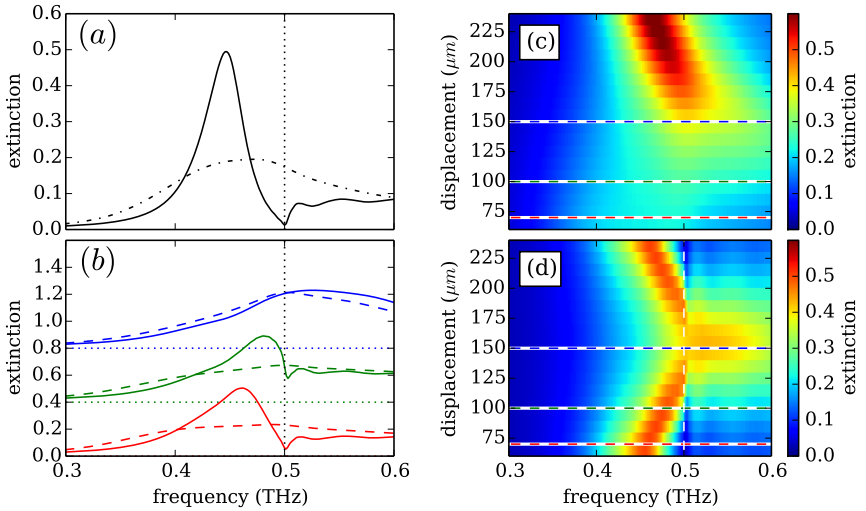

Figure 6.8: FDTD simulations for 2 identical disks of 160 μm × 40 μm, symmetrically surrounded by an index $n = 2$ dielectric. (a) Extinction spectrum of a 1D lattice with $\Gamma = 300$ μm containing a single disk per unit cell (solid black curve), and the isolated disk (dash-dotted curve). (b) Spectra of 2 identical disks displaced by 150 μm (blue curves), 100 μm (green curves), 70 μm (red curves). The curves are vertically off-set as indicated by the horizontal dotted lines. The dashed curves represent the extinction of the two disks surrounded by a PML, while the solid curves are simulations for a 1D chain of disks. The vertical dotted line indicates the RA condition at 0.5 THz. (c) Extinction spectra for 2 identical disks surrounded by a PML, where the dashed lines correspond to the displacements of the spectra shown in (b) with the dashed curves. (d) Extinction spectra of a 1D chain of identical disks with a period of $\Gamma = 300$ μm, as a function of the displacement. The horizontal dashed lines indicate the displacements of the solid curves shown in panel (b), the vertical dashed line indicates the RA condition.

Scatterers in a homogeneous environment

Results of the numerical simulations for configurations where all scatterers are identical are shown in figure 6.8. These simulations resemble the results of the CDM calculations presented in figure 6.4. The black dash-dotted curve represents the localized resonance of a cylindrical disk with diameters of 160 μm × 40 μm and a height of 0.1 μm. When the oblate spheroids used for the CDM calculations are replaced by cylindrical disks with the same outer dimensions the localized resonances undergo a redshift. Reducing the diameter of the long axis of the cylinder from 200 μm to 160 μm compensates this shift and allows the results from FDTD to be compared with the CDM calculations. As a consequence, the FDTD simulation for a 1D chain of one of these disks per unit-cell (solid black curve) agrees very well with

the CDM calculations, with only a small mismatch on the exact shape of the spectra around the RA condition at 0.5 THz. The resemblance of the FDTD to the CDM holds as well for the results of the simulations carried out for two identical dipoles in the unit-cell, presented in figure 6.8(b). When one of the scatterers is displaced by 150 µm (blue curves) the diffracted order at 0.5 THz is suppressed and the spectrum of the chain (solid curve) follows the spectrum of just the two interacting scatterers. This changes when the displacement is decreased to either 100 µm (green curves) or 70 µm (red curves) and the symmetry is broken. As for the CDM calculations there appears a narrow extinction minimum at the RA condition, and at slightly lower frequencies the extinction is enhanced. This is confirmed when looking at the

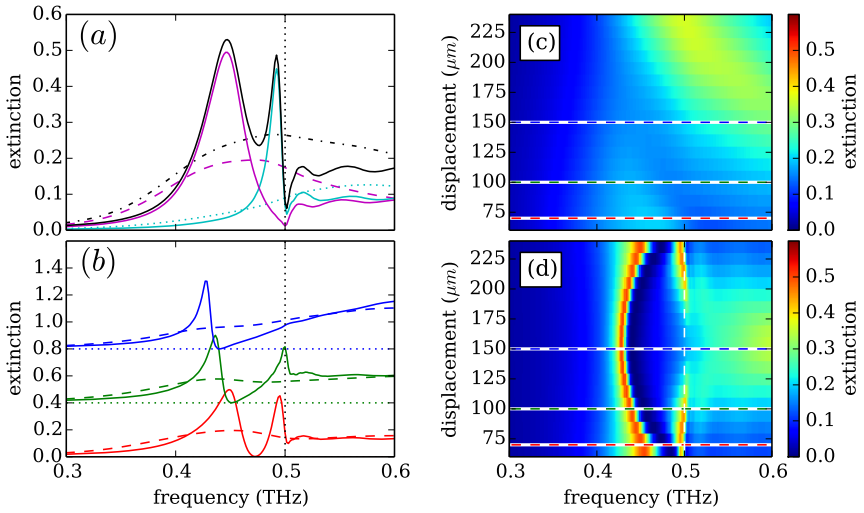

Figure 6.9: FDTD simulations for 2 detuned disks with dimensions of 160 µm × 40 µm and 125 µm × 60 µm, symmetrically surrounded by an index $n = 2$ dielectric. The height of the disks is 0.1 µm. (a) Extinction spectra for a 1D chain with a period of $\Gamma = 300$ µm containing only the 160 µm × 40 µm disk (solid magenta curve), only the 160 µm × 40 µm disk (solid cyan curve), and their incoherent sum (solid black curve). The discontinuous curves represent the extinction spectra of isolated disks, the vertical dotted line indicates the RA condition at 0.5 THz. (b) Spectra for the 2 detuned disks displaced by 150 µm (blue curves), 100 µm (green curves), 70 µm (red curves). The spectra are vertically off-set as indicated by the horizontal dotted lines. The dashed curves represent a pair of detuned dipoles, while the solid curves are simulations for a 1D periodic chain with a period of $\Gamma = 300$ µm. (c) Extinction spectra of the 2 detuned disks. The dashed lines mark the displacements of the spectra shown in (b) with the dashed curves. (d) Extinction spectra of a 1D chain of detuned disks with a period of $\Gamma = 300$ µm, as a function of the displacement of the dipoles. The horizontal dashed lines mark the displacements of spectra indicated by the solid curves shown in panel (b), the vertical dashed line indicates the RA condition.

color plots in figures 6.8(c) and 6.8(d), where the extinction is shown as a function of both frequency and displacement for just two disks and a 1D chain of displaced disks respectively. The difference between the calculations and the simulations as presented in 6.8(c) are minute, and can be attributed to the fact that the oblate spheroids in the CDM calculations are approximated by flat cylinders in the FDTD. The spectra simulated for the 1D chain of displaced scatterers differ from the CDM calculations on details but are similar on the main trends. In both systems the transparency window at the RA condition disappears when the displacement approaches half the pitch. Moving away from this condition the extinction minimum is re-introduced, as well as the extinction enhancement at slightly lower frequencies. The maximum in extinction redshifts as the displacement is further reduced.

Figure 6.9 shows results of FDTD simulations resembling CDM calculations for the displaced and detuned dipoles. As for the simulations of the identical dipoles the dimensions of the particles are adjusted to get a better agreement with the CDM calculations. The dimensions of one of the cylinders are set to 160 μm × 40 μm, while the other cylinder is resized to 125 μm × 60 μm. The surrounding material has a refractive index of $n = 2$. The agreement between the CDM calculations (figure 6.5) and the FDTD presented in figure 6.9 for the displaced and detuned dipoles is excellent. Aside from a few minor details all relevant characteristics are reproduced. The SLRs for a lattice containing either scatterer as presented in figure 6.9(a) both have a minimum in the extinction at the RA condition. The SLRs however do have their respective maximum in extinction at different frequencies since the dipoles are detuned. When these two SLRs are allowed to interfere coherently, as shown in figure 6.9(b), the additional extinction maximum appears at lower frequencies and a transparency window opens up.

Scatterers at an interface

The results presented in the previous subsection were generated for scatterers that are symmetrically embedded in a higher refractive index medium. Translating these systems to structures that are available for experimental verification requires that the scatterers are fabricated out of a good metal at THz frequencies, e.g. gold, on top of a quartz substrate and covered by a quartz superstrate. Although this should allow for verifying the far-field extinction spectra presented above, the presence of the superstrate prevents direct access to the near-fields. They can neither be measured nor used for potential sensing purposes. This limitation is resolved when the scatterers are placed at an interface of quartz and air. As mentioned in section 5.6 of this thesis the presence of multiple layers with mismatching refractive indexes prevents the existence of a transparency window at the RA condition. The transparency window resulting from the interference of the two SLRs when each unit-cell contains two detuned dipoles has a different origin and might exist at the interface.

The dimensions of the cylinders are chosen at 200 μm×40 μm and 155 μm×60 μm, which are 0.1 μm in height and made out of PEC. The particles are placed on top of a quartz ($n = 2$) substrate, and the upperstrate is replaced by air ($n = 1$). The

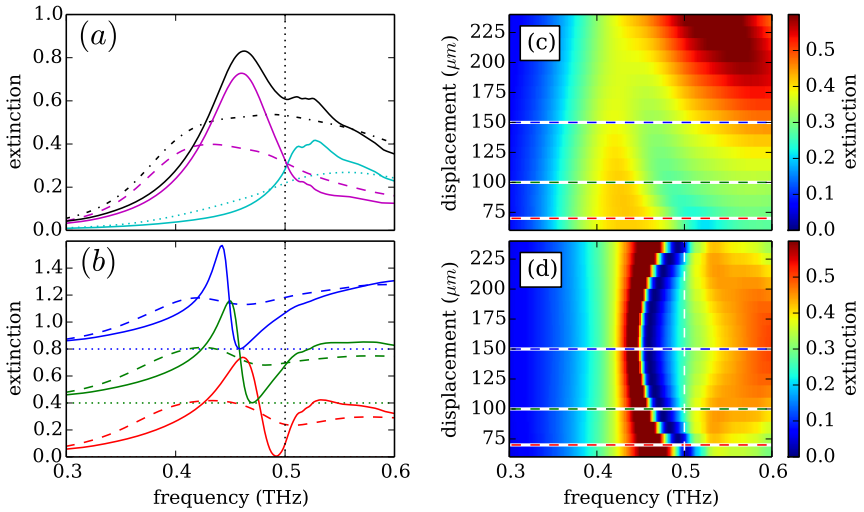

Figure 6.10: FDTD simulations for 2 detuned disks of 200 μm × 40 μm and 155 μm × 60 μm, on top of a substrate with an index of $n = 2$, at an interface with air. (a) Extinction spectra for a 1D chain with a period of $\Gamma = 300$ μm containing just the 200 μm × 40 μm disk (solid magenta curve), just the 155 μm × 60 μm disk (solid cyan curve), and their incoherent sum (solid black curve). The discontinuous curves represent the spectra of disks surrounded by PML, the vertical dotted line indicates the RA condition at 0.5 THz. (b) Spectra for the 2 detuned disks for displacements of 150 μm (blue curves), 100 μm (green curves), 70 μm (red curves) which are vertically off-set as indicated by the horizontal dotted lines. The dashed curves represent just the unit cell surrounded by a PML, while the solid curves are simulations for a 1D periodic chain with a period of $\Gamma = 300$ μm. (c) Extinction spectra for the 2 detuned disks surrounded by a PML, where the dashed lines correspond to the displacements of the spectra shown in (b) with the dashed curves. (d) Extinction spectra of a 1D chain of detuned disks with a period of $\Gamma = 300$ μm, as a function of the displacement. The horizontal dashed lines mark the displacements of the solid curves shown in panel (b), the vertical dashed line indicates the RA condition.

THz source in the simulations is incident from the quartz side. The configurations as presented for the detuned dipoles which are completely surrounded by quartz are repeated, and the results are presented in figure 6.10. Indeed, the SLRs in the chains with just one of the cylinders per unit-cell (figure 6.10(a)) do not show a clear minimum at the RA condition, and neither does their incoherent sum (solid black curve). This changes when both scatterers are placed in a single unit-cell and the two SLRs are allowed to interfere (figure 6.10(b)). As for the scatterers that are completely surrounded by quartz a transparency window opens up. A large difference though is that for the scatterers that are on top of the substrate the spectra appear less sensitive to their actual relative displacement. This is confirmed in figure 6.10(d).

6.5 Conclusions

When dipolar scatterers are ordered in a periodic lattice they can give rise to surface lattice resonances. When another dipole is added to the unit-cell SLRs are launched from both scatterers that scatter into the same RA. The interference between these two SLRs reshapes the extinction spectrum, as a function of the displacement between the dipoles in the unit cell. Is has been demonstrated that for a displacement which is half of the pitch of the lattice the transparency window at the diffraction order can be suppressed. When the dipoles are detuned the two SLRs form a hybrid mode, which results in an additional maximum at a frequency redshifted from the RA condition and an induced transparency window. This transparency window still exists when the scatterers are placed at an interface of air and quartz. This opens up opportunities for near-field experiments and potential sensing applications. Results calculated with a coupled dipole model are compared with numerical simulations and found to be in excellent agreement.

Appendix A

Transfer matrix method

An electromagnetic wave traveling through a stack of layers experiences reflections that affect the transmission due to interference. When a wave travels through a medium of a complex refractive index $\tilde{n} = n + i\kappa$, it acquires a phase proportional to both the thickness and n, while the amplitude decreases exponentially with κ upon propagation. At any discontinuity of the refractive index along the direction of propagation the wave is partially transmitted and reflected. For a geometry that contains multiple interfaces these reflections can interfere. This can result in non-trivial and complex valued transmission spectra. An approach based on the transfer matrix method can be used to calculate these spectra when all parameters defining the thickness and refractive indexes of the layers are known. The transfer matrix method can also be used for sample characterization. The dielectric properties of a single layer in the stack can be extracted by fitting the calculated transmission to the transmission experimentally acquired. The method described here combines the transfer matrix model as described by Troparevski [152] with the characterization algorithm of Duvillaret [153].

A continuous plane-wave in a medium A with a complex refractive index $\tilde{n}_A = n_A + i\kappa_A$ traveling in the $\pm x$ direction, with angular frequency ω and wavenumber $k_A = \tilde{n}_A\omega/c$, is described as a function of position and time according to:

$$E_A^{\pm}(x,t) = E_A^{\pm} e^{i(\pm k_A x - \omega t)} \ . \tag{A.1}$$

At an interface between two media, A and B, one can derive from Maxwell's equations the amplitude Fresnel coefficients for reflection and transmission [66]

$$\begin{aligned} r_{AB} &= \frac{\tilde{n}_B - \tilde{n}_A}{\tilde{n}_B + \tilde{n}_A} \ , \\ t_{AB} &= \frac{2\tilde{n}_A}{\tilde{n}_B + \tilde{n}_A} \ . \end{aligned} \tag{A.2}$$

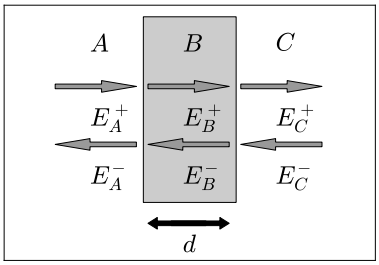

Figure A.1: Fresnel reflection at an interface. A schematic view of a slab of material (B) in between two semi-infinite planes (A and C). The arrows indicate the electromagnetic waves propagating in the forward and backward directions. The slab has a thickness of d.

Each wave propagating away from one of the interfaces inside the stack can be described as the sum of the transmission of one wave, and the reflection of another. As illustrated in figure A.1, which visualizes a slab of material in between two semi-infinite planes, the electric fields propagating away from interface AB can be expressed as

$$\begin{aligned} E_B^+ &= t_{AB}E_A^+ + r_{BA}E_B^- \\ E_A^- &= r_{AB}E_A^+ + t_{BA}E_B^- \end{aligned} \tag{A.3}$$

These equations can be rearranged, to express the fields in medium B in terms of fields in medium A, using $r_{AB} = -r_{BA}$ and $r_{AB}^2 + t_{AB}^2 = 1$:

$$\begin{aligned} E_A^+ &= \frac{1}{t_{AB}}(E_B^+ + r_{AB}E_B^-) \ , \\ E_A^- &= \frac{1}{t_{AB}}(r_{AB}E_B^+ + E_B^-) \ . \end{aligned} \tag{A.4}$$

This can be written in matrix notation

$$\begin{bmatrix} E_A^+ \\ E_A^- \end{bmatrix} = \boldsymbol{F}_{AB} \begin{bmatrix} E_B^+ \\ E_B^- \end{bmatrix} \ , \tag{A.5}$$

with the Fresnel matrix defined as

$$\boldsymbol{F}_{AB} = \frac{1}{t_{AB}} \begin{bmatrix} 1 & r_{AB} \\ r_{AB} & 1 \end{bmatrix} \ . \tag{A.6}$$

The waves also propagate through a layer between interfaces, which results in an increase of the phase, and a reduction of the amplitude in the presence of losses. Following the layout of figure A.1 we can describe the propagation between the left side (L) and the right (R) side of layer B as

$$\begin{aligned} E_R^+ &= E_L^+ e^{k_B d i} \ , \\ E_L^- &= E_R^- e^{k_B d i} \ . \end{aligned} \tag{A.7}$$

which can we rearranged as

$$\begin{bmatrix} E_L^+ \\ E_L^- \end{bmatrix} = \boldsymbol{P}_B \begin{bmatrix} E_R^+ \\ E_R^- \end{bmatrix} , \tag{A.8}$$

with the propagation matrix

$$\boldsymbol{P}_B = \begin{bmatrix} e^{-k_B di} & 0 \\ 0 & e^{k_B di} \end{bmatrix} , \tag{A.9}$$

where d is the thickness of the layer. The real part of k contributes to the development of the phase, while the imaginary part is responsible for losses due to absorption. The signs in he exponentials correct for the fact that waves at the left side are expressed in those at the right.

The behavior of a wave that travels through a series of layers, can now be described by simple matrix multiplication of the relevant Fresnel and propagation matrices. In the example case of figure A.1 we can write:

$$\begin{bmatrix} E_A^+ \\ E_A^- \end{bmatrix} = \boldsymbol{F}_{AB}\boldsymbol{P}_B\boldsymbol{F}_{BC} \begin{bmatrix} E_C^+ \\ E_C^- \end{bmatrix} = \boldsymbol{T}_{AC} \begin{bmatrix} E_C^+ \\ E_C^- \end{bmatrix} , \tag{A.10}$$

in which we define

$$\boldsymbol{T}_{AC} = \boldsymbol{F}_{AB}\boldsymbol{P}_B\boldsymbol{F}_{BC} , \tag{A.11}$$

as the transfer matrix (T-matrix).

The analysis above describes the waves that are incident and reflected on the left side, as a function of the incident and reflected/transmitted waves at the right side of the stack of layers. Assuming the only incident wave is the wave entering from the left, one can write $E_A^+ = T_{11}E_C^+$. The transmission coefficient of the total system, which can be complex valued, is given by $T_m = E_C^+/E_A^+ = 1/T_{11}$. A similar approach is applied for a multilayer system, and multiplying the alternating Fresnel and propagation matrices.

This complex transmission coefficient for an object under investigation can be obtained experimentally via THz-TDS, as explained in chapter 1. Using the T-matrix method as described above, for each frequency, one can solve for a set of unknown parameters. Here we will solve for the complex refractive index of one of the layers. There does not exist an unique solution for $\tilde{n}$, since the phase of T_m is only defined up to multiples of 2π. Additionally, the expression for T_m cannot be solved analytically for any of the refractive index parameters. Instead, the system needs to be solved numerically. The algorithm implemented is similar to the one described in [153]. In essence, with all other parameters of the system known (refractive indices and layer thicknesses), the ones to solve for are iteratively adjusted until the calculated T_m matches the experimental value T_{exp} within a specified range. This mismatch is defined as $\delta(n, \kappa) = \delta\rho^2 + \delta\phi^2$, with

$$\delta\rho = \ln|T_m| - \ln|T_{\text{exp}}| \tag{A.12}$$

and

$$\delta\phi = \arg(T_m) - \arg(T_{\exp}) \; . \tag{A.13}$$

The logarithms in equation (A.12) have he purpose to increase the robustness of the convergence of the algorithm for small transmissions.

Starting from an experimental transmission spectrum for a given sample, the frequency dependent complex refractive index for one of the layers can be reconstructed by consecutively solving for all frequencies. Beginning at the lowest frequency, an educated guess has to be made for the index. For all other frequencies, the converged value of the refractive index for a slightly lower frequency is used. This allows for fast convergence of the algorithm.

For continuous-wave signals, the procedure described above is accurate since it describes the transmission through a stack of layers taking into account an infinite number of internal reflections. Since THz-TDS operates in the time domain with well separated pulses of finite duration, the time window which is sampled does not necessarily contain the contributed reflections from all interfaces. This is for instance the case for the quartz and GaAs thick substrates. In the analysis this is compensated for by setting the relevant reflection coefficients r to zero in equation (A.6). The reliability of the extracted refractive spectrum depends on the experimental error in the transmission spectra, and dimensions of the layers. The experimental error that propagates as a result from the noise on the THz-TDS is indicated in the relevant graphs by error bars.

References

[1] Fitzpatrick, *History of Geometric Optics*, http://farside.ph.utexas.edu/teaching/302l/lectures/node125.html.

[2] H. Kubbinga, *Christiaan Huygens and the foundations of optics*, Pure and Applied Optics: Journal of the European Optical Society Part A **4**, 723 (1995).

[3] D. L. Sengupta and T. K. Sarkar, *Maxwell, Hertz, the Maxwellians, and the early history of electromagnetic waves*, Antennas and Propagation Magazine, IEEE **45**, 13 (2003).

[4] K. B. Wolf and G. Krotzsch, *Geometry and dynamics in refracting systems*, European Journal of Physics **16**, 14 (1995).

[5] R. Rashed, *A pioneer in anaclastics: Ibn Sahl on burning mirrors and lenses*, Isis , 464 (1990).

[6] C. Huygens, *Traite de la lumière*, 1678.

[7] A. Van Helden, *Roemer's speed of light*, Journal for the History of Astronomy **14**, 137 (1983).

[8] Fizeau, *Sur une expérience relative à la vitesse de propagation de la lumière*, Comp. Rend. Acad. Sci. **29**, 90 (1849).

[9] L. Foucault, *Détermination expérimentale de la vitesse de la lumière; parallaxe du Soleil*, Comptes Rendus **55**, 501 (1862).

[10] G. A. Boutry and A. J. Fresnel, *Augustin Fresnel: his time, life and work, 1788-1827.(Reprinted from" Science Progress")*, John Murray, 1949.

[11] D. J. Griffiths and R. College, *Introduction to electrodynamics*, volume 3, prentice Hall Upper Saddle River, NJ, 1999.

[12] J. C. Maxwell, *A Dynamical Theory of the Electromagnetic Field*, Proceedings of the Royal Society of London **13**, 531 (1863).

[13] H. Hertz and W. T. B. Kelvin, *Electric waves*, Macmillan London, 1893.

[14] M. Rothschild, T. Bloomstein, N. Efremow, T. Fedynyshyn, M. Fritze, I. Pottebaum, and M. Switkes, *Nanopatterning with UV optical lithography*, MRS bulletin **30**, 942 (2005).

[15] M. Stewart, M. Motala, J. Yao, L. Thompson, and R. Nuzzo, *Unconventional methods for forming nanopatterns*, Proceedings of the Institution of Mechanical Engineers, Part N: Journal of Nanoengineering and Nanosystems **220**, 81 (2006).

[16] A. A. Tseng, *Recent developments in nanofabrication using focused ion beams*, Small **1**, 924 (2005).

[17] F. Watt, A. Bettiol, J. Van Kan, E. Teo, and M. Breese, *Ion beam lithography and nanofabrication: a review*, International Journal of Nanoscience **4**, 269 (2005).

[18] P. Drude, *Zur elektronentheorie der metalle*, Annalen der Physik **306**, 566 (1900).

[19] N. Ashcroft and N. Mermin, *Solid State Physics*, Holt-Saunders, 1976.

[20] H. Raether, *Surface plasmons on smooth surfaces*, Springer, 1988.

[21] S. A. Maier, *Plasmonics: Fundamentals and Applications*, Springer, New York, USA, 2007.

[22] J. W. S. B. Rayleigh, *On the scattering of light by small particles*, 1871.

[23] H. C. van de Hulst, *Light Scattering by small particles*, Dover Publications, Inc., 1981.

[24] C. F. Bohren and D. R. Huffman, *Absorption and scattering of light by small particles*, Wiley, New York, 1983.

[25] J. Krenn et al., *Squeezing the optical near-field zone by plasmon coupling of metallic nanoparticles*, Physical Review Letters **82**, 2590 (1999).

[26] P. Nordlander, C. Oubre, E. Prodan, K. Li, and M. Stockman, *Plasmon hybridization in nanoparticle dimers*, Nano Letters **4**, 899 (2004).

[27] I. Romero, J. Aizpurua, G. W. Bryant, and F. J. García De Abajo, *Plasmons in nearly touching metallic nanoparticles: singular response in the limit of touching dimers*, Optics Express **14**, 9988 (2006).

[28] W. A. Murray and W. L. Barnes, *Plasmonic materials*, Advanced materials **19**, 3771 (2007).

[29] H. A. Bethe, *Theory of Diffraction by Small Holes*, Phys. Rev. **66**, 163 (1944).

[30] C. J. Bouwkamp, *Diffraction theory*, Reports on progress in physics **17**, 35 (1954).

[31] T. W. Ebbesen, H. Lezec, H. Ghaemi, T. Thio, and P. Wolff, *Extraordinary optical transmission through sub-wavelength hole arrays*, Nature **391**, 667 (1998).

[32] T. J. Kim, T. Thio, T. W. Ebbesen, D. Grupp, and H. J. Lezec, *Control of optical transmission through metals perforated with subwavelength hole arrays*, Optics Letters **24**, 256 (1999).

[33] J. Prikulis, P. Hanarp, L. Olofsson, D. Sutherland, and M. Käll, *Optical spectroscopy of nanometric holes in thin gold films*, Nano Letters **4**, 1003 (2004).

[34] D. Gao, W. Chen, A. Mulchandani, and J. S. Schultz, *Detection of tumor markers based on extinction spectra of visible light passing through gold nanoholes*, Appl. Phys. Lett. **90**, 073901 (2007).

[35] T. Rindzevicius, Y. Alaverdyan, A. Dahlin, F. Höök, D. S. Sutherland, and M. Käll, *Plasmonic sensing characteristics of single nanometric holes*, Nano Letters **5**, 2335 (2005).

[36] A. B. Dahlin, J. O. Tegenfeldt, and F. Höök, *Improving the instrumental resolution of sensors based on localized surface plasmon resonance*, Analytical chemistry **78**, 4416 (2006).

[37] A. Dahlin, M. Zäch, T. Rindzevicius, M. Käll, D. S. Sutherland, and F. Höök, *Localized surface plasmon resonance sensing of lipid-membrane-mediated biorecognition events*, Journal of the American Chemical Society **127**, 5043 (2005).

[38] C. Genet and T. Ebbesen, *Light in tiny holes*, Nature **445**, 39 (2007).

[39] J. Dintinger, S. Klein, and T. W. Ebbesen, *Molecule–Surface Plasmon Interactions in Hole Arrays: Enhanced Absorption, Refractive Index Changes, and All-Optical Switching*, Advanced Materials **18**, 1267 (2006).

[40] I. I. Smolyaninov, A. V. Zayats, A. Stanishevsky, and C. C. Davis, *Optical control of photon tunneling through an array of nanometer-scale cylindrical channels*, Physical Review B **66**, 205414 (2002).

[41] C. Janke, J. G. Rivas, P. H. Bolivar, and H. Kurz, *All-optical switching of the transmission of electromagnetic radiation through subwavelength apertures*, Optics Letters **30**, 2357 (2005).

[42] J. Dintinger, I. Robel, P. V. Kamat, C. Genet, and T. W. Ebbesen, *Terahertz All-Optical Molecule-Plasmon Modulation*, Advanced Materials **18**, 1645 (2006).

[43] E. Altewischer, M. Van Exter, and J. Woerdman, *Plasmon-assisted transmission of entangled photons*, Nature **418**, 304 (2002).

[44] K. L. Kelly, E. Coronado, L. L. Zhao, and G. C. Schatz, *The optical properties of metal nanoparticles: the influence of size, shape, and dielectric environment*, The Journal of Physical Chemistry B **107**, 668 (2003).

[45] J. Mock, M. Barbic, D. Smith, D. Schultz, and S. Schultz, *Shape effects in plasmon resonance of individual colloidal silver nanoparticles*, The Journal of Chemical Physics **116**, 6755 (2002).

[46] T. Jensen, L. Kelly, A. Lazarides, and G. C. Schatz, *Electrodynamics of Noble Metal Nanoparticles and Nanoparticle Clusters*, Journal of Cluster Science **10**, 295 (1999).

[47] W. Eggimann and R. Collin, *Electromagnetic diffraction by a planar array of circular disks*, Microwave Theory and Techniques, IRE Transactions on **10**, 528 (1962).

[48] C.-C. Chen, *Diffraction of electromagnetic waves by a conducting screen perforated periodically with holes*, Microwave Theory and Techniques, IEEE Transactions on **19**, 475 (1971).

[49] R. McPhedran, G. Derrick, and L. Botten, *Electromagnetic theory of gratings*, Topics in Current Physics **22**, 227 (1980).

[50] D. H. Dawes, R. C. McPhedran, and L. B. Whitbourn, *Thin capacitive meshes on a dielectric boundary: theory and experiment*, Applied optics **28**, 3498 (1989).

[51] E. Popov, M. Neviere, S. Enoch, and R. Reinisch, *Theory of light transmission through subwavelength periodic hole arrays*, Physical Review B **62**, 16100 (2000).

[52] L. Martin-Moreno, F. Garcia-Vidal, H. Lezec, K. Pellerin, T. Thio, J. Pendry, and T. Ebbesen, *Theory of extraordinary optical transmission through subwavelength hole arrays*, Physical Review Letters **86**, 1114 (2001).

[53] L. Salomon, F. Grillot, A. V. Zayats, and F. De Fornel, *Near-field distribution of optical transmission of periodic subwavelength holes in a metal film*, Physical Review Letters **86**, 1110 (2001).

[54] R. Wannemacher, *Plasmon-supported transmission of light through nanometric holes in metallic thin films*, Optics communications **195**, 107 (2001).

[55] M. Sarrazin, J.-P. Vigneron, and J.-M. Vigoureux, *Role of Wood anomalies in optical properties of thin metallic films with a bidimensional array of subwavelength holes*, Phys. Rev. B **67**, 085415 (2003).

[56] F. Przybilla, A. Degiron, J. Laluet, C. Genet, and T. Ebbesen, *Optical transmission in perforated noble and transition metal films*, Journal of Optics A: Pure and Applied Optics **8**, 458 (2006).

[57] H. Cao and A. Nahata, *Resonantly enhanced transmission of terahertz radiation through a periodic array of subwavelength apertures*, Optics Express **12**, 1004 (2004).

[58] S. Selcuk, K. Woo, D. Tanner, A. Hebard, A. Borisov, and S. Shabanov, *Trapped electromagnetic modes and scaling in the transmittance of perforated metal films*, Physical Review Letters **97**, 067403 (2006).

[59] Y. Ekinci, H. H. Solak, and C. David, *Extraordinary optical transmission in the ultraviolet region through aluminum hole arrays*, Optics Letters **32**, 172 (2007).

[60] F. Przybilla, C. Genet, and T. Ebbesen, *Enhanced transmission through Penrose subwavelength hole arrays*, Appl. Phys. Lett. **89**, 121115 (2006).

[61] S. Mei, T. Jie, L. Zhi-Yuan, C. Bing-Ying, Z. Dao-Zhong, J. Ai-Zi, and Y. Hai-Fang, *The role of periodicity in enhanced transmission through subwavelength hole arrays*, Chinese Physics Letters **23**, 486 (2006).

[62] T. Matsui, A. Agrawal, A. Nahata, and Z. V. Vardeny, *Transmission resonances through aperiodic arrays of subwavelength apertures*, Nature **446**, 517 (2007).

[63] N. Papasimakis, V. Fedotov, A. Schwanecke, N. Zheludev, and F. G. de Abajo, *Enhanced microwave transmission through quasicrystal hole arrays*, Appl. Phys. Lett. **91**, 081503 (2007).

[64] A. Krishnan, T. Thio, T. Kim, H. Lezec, T. Ebbesen, P. Wolff, J. Pendry, L. Martin-Moreno, and F. Garcia-Vidal, *Evanescently coupled resonance in surface plasmon enhanced transmission*, Optics communications **200**, 1 (2001).

[65] J. Gomez Rivas, C. Schotsch, P. Haring Bolivar, and H. Kurz, *Enhanced transmission of THz radiation through subwavelength holes*, Physical Review B **68**, 201306 (2003).

[66] E. Hecht, *Optics*, Addison Wesley, 4th edition, 2002.

[67] R. W. Wood, *On a Remarkable Case of Uneven Distribution of Light in a Diffraction Grating Spectrum*, Proceedings of the Physical Society of London **18**, 269 (1902).

[68] L. Rayleigh, *III. Note on the remarkable case of diffraction spectra described by Prof. Wood*, Philosophical Magazine Series 6 **14**, 60 (1907).

[69] L. Rayleigh, *On the Dynamical Theory of Gratings*, Proceedings of the Royal Society of London. Series A **79**, 399 (1907).

[70] F. J. García de Abajo, *Colloquium: Light scattering by particle and hole arrays*, Reviews of Modern Physics **79**, 1267 (2007).

[71] S. Zou, N. Janel, and G. C. Schatz, *Silver nanoparticle array structures that produce remarkably narrow plasmon lineshapes*, The Journal of chemical physics **120**, 10871 (2004).

[72] E. M. Hicks, S. Zou, G. C. Schatz, K. G. Spears, R. P. Van Duyne, L. Gunnarsson, T. Rindzevicius, B. Kasemo, and M. Käll, *Controlling plasmon line shapes through diffractive coupling in linear arrays of cylindrical nanoparticles fabricated by electron beam lithography*, Nano letters **5**, 1065 (2005).

[73] F. G. De Abajo and J. Sáenz, *Electromagnetic surface modes in structured perfect-conductor surfaces*, Physical Review Letters **95**, 233901 (2005).

[74] Y. Chu, E. Schonbrun, T. Yang, and K. B. Crozier, *Experimental observation of narrow surface plasmon resonances in gold nanoparticle arrays*, Applied Physics Letters **93**, 181108 (2008).

[75] B. Auguié and W. Barnes, *Collective Resonances in Gold Nanoparticle Arrays*, Physical Review Letters **101**, 1 (2008).

[76] V. Kravets, F. Schedin, and a. Grigorenko, *Extremely Narrow Plasmon Resonances Based on Diffraction Coupling of Localized Plasmons in Arrays of Metallic Nanoparticles*, Physical Review Letters **101**, 087403 (2008).

[77] G. Vecchi, V. Giannini, and J. Gómez Rivas, *Surface modes in plasmonic crystals induced by diffractive coupling of nanoantennas*, Phys. Rev. B **80**, 201401 (2009).

[78] S. R. K. Rodriguez, A. Abass, B. Maes, O. T. A. Janssen, G. Vecchi, and J. Gómez Rivas, *Coupling Bright and Dark Plasmonic Lattice Resonances*, Phys. Rev. X **1**, 021019 (2011).

[79] W. Zhou and T. W. Odom, *Tunable subradiant lattice plasmons by out-of-plane dipolar interactions*, Nature Nanotech. **6**, 423 (2011).

[80] T. V. Teperik and A. Degiron, *Design strategies to tailor the narrow plasmon-photonic resonances in arrays of metallic nanoparticles*, Phys. Rev. B **86**, 245425 (2012).

[81] D. A. Burns and E. W. Ciurczak, *Handbook of near-infrared analysis*, CRC press, 2007.

[82] C. A. Balanis, *Circular waveguides*, Int. J. Electron. **1996**, 551 (1996).

[83] J. Pedersen and S. Keiding, *THz time-domain spectroscopy of nonpolar liquids*, Quantum Electronics, IEEE Journal of **28**, 2518 (1992).

[84] J. Qin, Y. Ying, and L. Xie, *The detection of agricultural products and food using terahertz spectroscopy: A review*, Applied Spectroscopy Reviews **48**, 439 (2013).

[85] D. M. Mittleman, R. Jacobsen, R. Neelamani, R. G. Baraniuk, and M. C. Nuss, *Gas sensing using terahertz time-domain spectroscopy*, Applied Physics B: Lasers and Optics **67**, 379 (1998).

[86] M. Tonouchi, *Cutting-edge terahertz technology*, Nature Photonics **1**, 97 (2007).

[87] A. Markelz, S. Whitmire, J. Hillebrecht, and R. Birge, *THz time domain spectroscopy of biomolecular conformational modes*, Physics in Medicine and Biology **47**, 3797 (2002).

[88] T. Chan, J. Bjarnason, A. Lee, M. Celis, and E. Brown, *Attenuation contrast between biomolecular and inorganic materials at terahertz frequencies*, Appl. Phys. Lett. **85**, 2523 (2004).

[89] P. H. Siegel, *Terahertz technology in biology and medicine*, in *Microwave Symposium Digest, 2004 IEEE MTT-S International*, volume 3, pages 1575–1578, IEEE, 2004.

[90] B. Ferguson and X.-C. Zhang, *Materials for terahertz science and technology*, Nature materials **1**, 26 (2002).

[91] S. L. Dexheimer, *Terahertz spectroscopy: principles and applications*, CRC press, 2008.

[92] P. Jepsen, D. Cooke, and M. Koch, *Terahertz spectroscopy and imaging - Modern techniques and applications*, Laser & Photonics Reviews **5**, 124 (2011).

[93] R. Matsunaga and R. Shimano, *Nonequilibrium BCS State Dynamics Induced by Intense Terahertz Pulses in a Superconducting NbN Film*, Phys. Rev. Lett. **109**, 187002 (2012).

[94] T. Kampfrath, K. Tanaka, and K. A. Nelson, *Resonant and nonresonant control over matter and light by intense terahertz transients*, Nature Photonics **7**, 680 (2013).

[95] M. Hangyo, M. Tani, and T. Nagashima, *Terahertz time-domain spectroscopy of solids: a review*, International journal of infrared and millimeter waves **26**, 1661 (2005).

[96] J. Gomez Rivas, M. Kuttge, H. Kurz, P. Haring Bolivar, and J. A. Sanchez-Gil, *Low-frequency active surface plasmon optics on semiconductors*, Applied Physics Letters **88**, 082106 (2006).

[97] J. Sánchez-Gil and J. Rivas, *Thermal switching of the scattering coefficients of terahertz surface plasmon polaritons impinging on a finite array of subwavelength grooves on semiconductor surfaces*, Physical Review B **73**, 205410 (2006).

[98] H.-T. Chen, H. Lu, A. K. Azad, R. D. Averitt, A. C. Gossard, S. a. Trugman, J. F. O'Hara, and A. J. Taylor, *Electronic control of extraordinary terahertz transmission through subwavelength metal hole arrays*, Optics Express **16**, 7641 (2008).

[99] J. Gomez Rivas, J. Sanchez-Gil, M. Kuttge, P. Haring Bolivar, and H. Kurz, *Optically switchable mirrors for surface plasmon polaritons propagating on semiconductor surfaces*, Physical Review B **74**, 245324 (2006).

[100] E. Hendry, F. Garcia-Vidal, L. Martin-Moreno, J. Rivas, M. Bonn, A. Hibbins, and M. Lockyear, *Optical Control over Surface-Plasmon-Polariton-Assisted THz Transmission through a Slit Aperture*, Physical Review Letters **100**, 123901 (2008).

[101] A. K. Azad, H.-T. Chen, S. R. Kasarla, A. J. Taylor, Z. Tian, X. Lu, W. Zhang, H. Lu, A. C. Gossard, and J. F. O'Hara, *Ultrafast optical control of terahertz surface plasmons in subwavelength hole arrays at room temperature*, Applied Physics Letters **95**, 011105 (2009).

[102] T. Okada, S. Tsuji, K. Tanaka, and K. Hirao, *Transmission properties of surface plasmon polaritons and localized resonance in semiconductor hole arrays*, Appl. Phys. Lett. **97**, 261111 (2010).

[103] J. Rivas, M. Kuttge, P. Bolivar, H. Kurz, and J. Sánchez-Gil, *Propagation of Surface Plasmon Polaritons on Semiconductor Gratings*, Physical Review Letters **93**, 256804 (2004).

[104] Wafertech, http://www.wafertech.co.uk/products/gallium-arsenide-gaas/.

[105] IOFFE, http://www.ioffe.ru/SVA/NSM/Semicond/Si/basic.html.

[106] C. Jacoboni, C. Canali, G. Ottaviani, and A. Alberigi Quaranta, *A review of some charge transport properties of silicon*, Solid-State Electronics **20**, 77 (1977).

[107] IOFFE, http://www.ioffe.ru/SVA/NSM/Semicond/InSb/basic.html.

[108] G. Stillman, C. Wolfe, and J. Dimmock, *Hall coefficient factor for polar mode scattering in n-type GaAs*, Journal of Physics and Chemistry of Solids **31**, 1199 (1970).

[109] R. Ulbricht, E. Hendry, J. Shan, T. F. Heinz, and M. Bonn, *Carrier dynamics in semiconductors studied with time-resolved terahertz spectroscopy*, Reviews of Modern Physics **83**, 543 (2011).

[110] A. Yariv and P. Yeh, *Photonics: Optical Electronics in Modern Communications*, Oxford University Press, Oxford, 6 edition, 2007.

[111] D. Grischkowsky, S. Keiding, M. Van Exter, and C. Fattinger, *Far-infrared time-domain spectroscopy with terahertz beams of dielectrics and semiconductors*, J. Opt. Soc. Am. B **7**, 2006 (1990).

[112] B. R. Bennett, R. A. Soref, and J. A. Del Alamo, *Carrier-induced change in refractive index of InP, GaAs and InGaAsP*, Quantum Electronics, IEEE Journal of **26**, 113 (1990).

[113] E. Perret, N. Zerounian, S. David, and F. Aniel, *Complex permittivity characterization of benzocyclobutene for terahertz applications*, Microelectronic Engineering **85**, 2276 (2008).

[114] A. Berrier, R. Ulbricht, M. Bonn, and J. G. Rivas, *Ultrafast active control of localized surface plasmon resonances in silicon bowtie antennas*, Optics Express **18**, 23226 (2010).

[115] A. Berrier, P. Albella, M. A. Poyli, R. Ulbricht, M. Bonn, J. Aizpurua, and J. G. Rivas, *Detection of deep-subwavelength dielectric layers at terahertz frequencies using semiconductor plasmonic resonators*, Optics Express **20**, 5052 (2012).

[116] J. Schermer, G. Bauhuis, P. Mulder, E. Haverkamp, J. van Deelen, A. van Niftrik, and P. Larsen, *Photon confinement in high-efficiency, thin-film III-V solar cells obtained by epitaxial lift-off*, Thin Solid Films **511-512**, 645 (2006).

[117] G. Georgiou, H. K. Tyagi, P. Mulder, G. J. Bauhuis, J. J. Schermer, and J. G. Rivas, *Photo-generated THz antennas*, Scientific reports **4**, 3584 (2014).

[118] D. Rode, *Semiconductors and semimetals*, Academic, New York , 5 (1975).

[119] A. Sundaramurthy, K. Crozier, G. Kino, D. Fromm, P. Schuck, and W. Moerner, *Field enhancement and gap-dependent resonance in a system of two opposing tip-to-tip Au nanotriangles*, Physical Review B **72**, 165409 (2005).

[120] A. Rusina, M. Durach, K. A. Nelson, and I. Mark, *Nanoconcentration of terahertz radiation in plasmonic waveguides*, Optics Express **16**, 1377 (2008).

[121] S.-H. Kim, E. S. Lee, Y. B. Ji, and T.-I. Jeon, *Improvement of THz coupling using a tapered parallel-plate waveguide*, Optics Express **18**, 1289 (2010).

[122] V. Zon and B. Zon, *Terahertz surface plasmon polaritons on a conductive right circular cone: Analytical description and experimental verification*, Physical Review A **84**, 013816 (2011).

[123] J. Zhang and D. Grischkowsky, *Adiabatic compression of parallel-plate metal waveguides for sensitivity enhancement of waveguide THz time-domain spectroscopy*, Applied Physics Letters **86**, 061109 (2005).

[124] H. Zhan, R. Mendis, and D. M. Mittleman, *Superfocusing terahertz waves below λ / 250 using plasmonic parallel-plate waveguides*, Optics Express **18**, 9643 (2010).

[125] M. Wachter, M. Nagel, and H. Kurz, *Tapered photoconductive terahertz field probe tip with subwavelength spatial resolution*, Applied Physics Letters **95**, 041112 (2009).

[126] T. D. Nguyen, Z. V. Vardeny, and A. Nahata, *Concentration of terahertz radiation through a conically tapered aperture*, Optics Express **18**, 25441 (2010).

[127] J. Saxler, J. Gómez Rivas, C. Janke, H. Pellemans, P. Bolívar, and H. Kurz, *Time-domain measurements of surface plasmon polaritons in the terahertz frequency range*, Physical Review B **69**, 155427 (2004).

[128] S. Adachi, *Handbook of physical properties of semiconductors*, volume 2, Kluwer Academic Pub, 2004.

[129] N. Marcuvitz, *Waveguide handbook*, volume 10 of *MIT Radiation Laboratory Series*, McGraw-Hill, New York, 1951.

[130] B. J. Messinger, V. Raben, R. K. Chang, P. W. Barber, J. Messinger, and K. Ulrich, *Local fields at the surface of noble-metal microspheres*, Physical Review B **24** (1981).

[131] J. Han, A. Lakhtakia, Z. Tian, X. Lu, and W. Zhang, *Magnetic and magnetothermal tunabilities of subwavelength-hole arrays in a semiconductor sheet*, Optics Letters **34**, 1465 (2009).

[132] H. Yin and P. Hui, *Controlling enhanced transmission through semiconductor gratings with subwavelength slits by a magnetic field: Numerical and analytical results*, Appl. Phys. Lett. **95**, 011115 (2009).

[133] S. Zou and G. C. Schatz, *Narrow plasmonic/photonic extinction and scattering line shapes for one and two dimensional silver nanoparticle arrays*, The Journal of chemical physics **121**, 12606 (2004).

[134] G. Vecchi, V. Giannini, and J. Gómez Rivas, *Shaping the Fluorescent Emission by Lattice Resonances in Plasmonic Crystals of Nanoantennas*, Physical Review Letters **102**, 146807 (2009).

[135] V. Giannini, A. Berrier, S. a. Maier, J. A. Sánchez-Gil, and J. G. Rivas, *Scattering efficiency and near field enhancement of active semiconductor plasmonic antennas at terahertz frequencies*, Optics Express **18**, 2797 (2010).

[136] A. Bitzer, J. Wallauer, H. Helm, H. Merbold, T. Feurer, and M. Walther, *Lattice modes mediate radiative coupling in metamaterial arrays*, Optics Express **17**, 758 (2009).

[137] B. Ng, S. M. Hanham, V. Giannini, Z. C. Chen, M. Tang, Y. F. Liew, N. Klein, M. H. Hong, and S. a. Maier, *Lattice resonances in antenna arrays for liquid sensing in the terahertz regime*, Optics Express **19**, 14653 (2011).

[138] R. Singh, C. Rockstuhl, and W. Zhang, *Strong influence of packing density in terahertz metamaterials*, Applied Physics Letters **97**, 241108 (2010).

[139] J. Wallauer, A. Bitzer, S. Waselikowski, and M. Walther, *Near-field signature of electromagnetic coupling in metamaterial arrays : a terahertz microscopy study*, Optics Express **19**, 3212 (2011).

[140] J. Grant, X. Shi, J. Alton, and D. Cumming, *Terahertz localized surface plasmon resonance of periodic silicon microring arrays*, Journal of Applied Physics **109**, 054903 (2011).

[141] T. Okada and K. Tanaka, *Photo-designed terahertz devices*, Scientific reports **1** (2011).

[142] I. Chatzakis, P. Tassin, L. Luo, N.-H. Shen, L. Zhang, J. Wang, T. Koschny, and C. M. Soukoulis, *One-and two-dimensional photo-imprinted diffraction gratings for manipulating terahertz waves*, Applied Physics Letters **103**, 043101 (2013).

[143] S. Busch, B. Scherger, M. Scheller, and M. Koch, *Optically controlled terahertz beam steering and imaging*, Optics letters **37**, 1391 (2012).

[144] Z. Xie, X. Wang, J. Ye, S. Feng, W. Sun, T. Akalin, and Y. Zhang, *Spatial Terahertz Modulator*, Scientific Reports **3** (2013).

[145] T. Steinbusch, H. Tyagi, M. Schaafsma, G. Georgiou, and J. Gómez Rivas, *Active terahertz beam steering by photo-generated graded index gratings in thin semiconductor films*, Optics Express **22**, 26559 (2014).

[146] C. Rizza, A. Ciattoni, L. Columbo, M. Brambilla, and F. Prati, *Terahertz optically tunable dielectric metamaterials without microfabrication*, Optics letters **38**, 1307 (2013).

[147] A. B. Evlyukhin, S. I. Bozhevolnyi, A. Pors, M. G. Nielsen, I. P. Radko, M. Willatzen, and O. Albrektsen, *Detuned electrical dipoles for plasmonic sensing*, Nano Letters **10**, 4571 (2010).

[148] S. I. Bozhevolnyi, A. B. Evlyukhin, A. Pors, M. G. Nielsen, M. Willatzen, and O. Albrektsen, *Optical transparency by detuned electrical dipoles*, New Journal of Physics **13**, 023034 (2011).

[149] A. Pors, M. Willatzen, O. Albrektsen, and S. I. Bozhevolnyi, *Detuned electrical dipoles metamaterial with bianisotropic response*, Physical Review B **83**, 245409 (2011).

[150] V. Giannini, Y. Francescato, H. Amrania, C. C. Phillips, and S. A. Maier, *Fano resonances in nanoscale plasmonic systems: a parameter-free modeling approach*, Nano letters **11**, 2835 (2011).

[151] Z. Tian, A. K. Azad, X. Lu, J. Gu, J. Han, Q. Xing, A. J. Taylor, J. F. OâHara, and W. Zhang, *Large dynamic resonance transition between surface plasmon and localized surface plasmon modes*, Optics express **18**, 12482 (2010).

[152] M. C. Troparevsky, A. S. Sabau, A. R. Lupini, and Z. Zhang, *Transfer-matrix formalism for the calculation of optical response in multilayer systems: from coherent to incoherent interference*, Optics Express **18**, 24715 (2010).

[153] L. Duvillaret, F. Garet, and J.-L. Coutaz, *A reliable method for extraction of material parameters in terahertz time-domain spectroscopy*, IEEE Journal of Selected Topics in Quantum Electronics **2**, 739 (1996).

THz resonances in semiconductor structures: Summary

Light is one of the most marvelous phenomena around us. We use the light that scatters and reflects from our surroundings to orient ourselves, while the energy from the light that is absorbed by organisms fuels most of the life on this planet. The interaction between light and matter depends not only strongly on the atomic and/or molecular properties of the material; as a result of the wave-like nature of light, it also depends on the structure of an object and its surroundings on length-scales in the order of the wavelength. Understanding the precise interaction between light and its environment enables the design of structures with well-defined optical properties. Being able to design when, where and how the light interacts with its surroundings opens up possibilities for many sensing applications.

One of the ways to manipulate light is by scattering of small metallic particles. Exactly how a particle scatters the light depends on how it is shaped, its composition and surrounding. In this doctoral thesis we discuss both experimentally and theoretically how scatterers smaller than the wavelength interact with incident electromagnetic waves, and how this interaction changes when an ensemble of these scatterers is organized into a periodic lattice. Although the frequency range under consideration in this thesis is that of THz frequencies, i.e. far infrared, most of the physics applies to the full electromagnetic spectrum. Especially the range of frequencies in the visible and near-infrared.

In *Chapter 1* a short historic background is given on the development of the fundamental theory for optics and electromagnetism. The optical properties of most metals and doped semiconductors can be described with the Drude model, which is explained. The chapter describes how scattering properties of semiconductor and metallic particles are approximated, and where these approximations are limited. A periodic arrangement of particles has diffraction orders which depend on the

spacing between the particles, the frequency and angle of the incident light. An important condition is when a diffracted order scatters into the plane of the array. This frequency is called the Rayleigh anomaly (RA) condition. Light diffracted in the plane of the array enhances the radiative coupling between the scatterers and gives rise to sharp resonances known as Surface Lattice Resonances (SLRs). Next the electromagnetic spectrum at terahertz frequencies, versatile in applications and rich in physics, is introduced. In particular the optical properties of doped semiconductors at these frequencies are explained, and a comment is made on the relation between semiconductors and plasmonics. The chapter is ended with a short description of standard techniques for generating and detecting single-cycle THz pulses.

Chapter 2 introduces in more detail the operation of the THz time-domain spectrometers which are used for the acquisition of the experimental results presented in this thesis. An example of a typical transient and spectrum is given, as well as an explanation of how the measurement data are processed in order to obtain the extinction spectra. The time-domain signals of the THz spectrometer can be used as well for retrieving the optical constants of thick undoped substrates, and the electronic properties of thin films of doped semiconductors. This retrieval is done with an analysis based on the transfer matrix method. The substrates of the samples, as well as the polymers used for bonding the semiconductor thin layers to these substrates, are characterized using this transfer matrix method. For photo-excited carriers in a thin GaAs film this method is used to theoretically estimate the effect on the transmission of THz radiation due to ambipolar carrier diffusion.

We demonstrate experimentally the resonant extinction of THz radiation from a single metallic bowtie antenna in *Chapter 3*. This antenna is formed by two n-doped Si monomers with a triangular shape and facing apexes. This demonstration is achieved by placing the antenna at the output aperture of a conically tapered waveguide, which enhances the intensity of the incident THz field at the antenna position by a factor 10. The waveguide also suppresses the background radiation from the experimental setup that otherwise is transmitted without being scattered by the antenna. Bowtie antennas, supporting localized resonances, are relevant due to their ability of resonantly enhancing the field intensity at the gap separating the two triangular elements. This gap has subwavelength dimensions, which allows the concentration of THz radiation beyond the diffraction limit. The combination of a bowtie antenna and a conical waveguide may serve as a platform for far-field THz time-domain spectroscopy of single nanostructures placed in the gap.

In *Chapter 4* we investigate theoretically the enhanced THz extinction by periodic arrangements of semiconductor particles. The localized resonances of the individual particles in the ensemble can couple with each other through diffraction, and as a result of the periodic nature of the array give rise to SLRs. This diffractive coupling can be modeled with a coupled dipole model, which is introduced in this chapter. The most simple structure with periodicity is a 1D chain of dipoles. Using GaAs

as the semiconductor it is shown that these resonances are characterized by a large extinction and narrow bandwidth. The enhanced THz extinction in 1D chains of GaAs particles can be tuned in a wide range as a function of the concentration of the charge carriers present in the semiconductor. The underlaying mechanism of the diffractive coupling leading to this tuneability is explained in this chapter.

The experimental investigation of the enhanced THz extinction by periodic arrays of semiconductor particles is presented in *Chapter 5*. In this chapter we study at terahertz frequencies SLRs in a 2D periodic array of As doped Si square particles, and in photo-generated arrays in a continuous GaAs layer. The 2D arrays are chosen instead of a 1D chain due to the larger filling fraction of the particles, which leads to a larger extinction in the measurements. Experimental results from the Si arrays are supported by coupled dipole model calculations and simulations using the finite-difference in time-domain method. Numerical simulations show local intensity enhancements over an order of magnitude in the near-field, and an average intensity enhancement in the unit-cell of a factor 2.5. We demonstrate the concept of active control of SLR in a continuous GaAs thin film through selective photo-excitation. Using a spatial light modulator an image is projected on the semiconductor, inducing free charge-carriers only on the illuminated areas. By changing the pattern of illumination, the optical properties of the film at THz frequencies can be manipulated and controlled. The experimental results are compared against numerical simulations and are found to be in good agreement.

Chapter 6 discusses the extinction spectrum of a periodic chain of dipoles with two dipoles per unit-cell. In such a periodic lattice two SLRs will be excited by the same RA, one from each dipole in the unit-cell. The interference between these two SLRs reshapes the collective extinction spectrum, as a function of the displacement between the dipoles. In this chapter the coupled dipole model as presented earlier is extended to contain multiple dipoles per unit-cell. It is found that for a displacement which is half of the pitch of the lattice the characteristic transparency window at the RA can be suppressed. When the dipoles are detuned two modes hybridize, which results in an additional maximum in the far-field extinction at a frequency redshifted from the RA condition and an induced transparency window. The calculations are compared with numerical simulations and found to be in excellent agreement. This induced transparency window still exists when the scatterers are placed at an interface of air and quartz. This opens up opportunities for near-field experiments and potential sensing applications.

Samenvatting in het Nederlands

In de wereld om ons heen is 'licht' een van de meest bijzondere fenomenen. Het licht dat verstrooit en reflecteert in onze omgeving gebruiken we om ons te oriënteren, terwijl de energie van het licht dat wordt geabsorbeerd door organismen het overgrote deel van het leven op aarde aandrijft. De interactie tussen licht en materie hangt niet alleen sterk samen met de atomaire en/of moleculaire eigenschappen van een materiaal; als gevolg van de golf-eigenschappen van het licht hangt deze ook samen met de structuur van een object en zijn omgeving op de lengte-schaal van de golflengte. Het doorgronden van die precieze interactie tussen licht en zijn omgeving maakt het mogelijk om structuren te ontwerpen met specifieke optische eigenschappen. In staat zijn om te ontwerpen wanneer, waar en hoe licht in interactie met zijn omgeving is, biedt mogelijkheden voor veel toepassingen op het gebied van sensoren.

Een van de mogelijkheden om licht te manipuleren is verstrooiing vanaf kleine metalen deeltjes. De exacte verstrooiing van een deeltje hangt samen met zijn vorm, samenstelling en omgeving. In dit proefschrift wordt zowel experimenteel als theoretisch beschreven hoe de wisselwerking is tussen verstrooiers kleiner dan de golflengte van licht en elektromagnetische golven én hoe deze wisselwerking verandert wanneer een verzameling van deze verstrooiers wordt gerangschikt in een periodiek rooster. Hoewel het frequentiedomein dat wordt besproken in dit proefschrift ligt in dat van enkele terahertz, d.w.z. het verre infrarood, kan de meeste fysica toegepast worden op het volledige elektromagnetische spectrum. Dus ook en vooral op het domein van het zichtbare licht en het nabije infrarood.

In *hoofdstuk 1* wordt kort de historische achtergrond geschetst van de ontwikkeling van de fundamentele theorie voor optica en elektromagnetisme. De optische eigenschappen van de meeste metalen en gedoteerde halfgeleiders kunnen worden beschreven met het Drude model dat hier wordt uitgelegd. Het hoofdstuk beschrijft hoe de verstrooiings eigenschappen van halfgeleider en metalen deeltjes worden benaderd en tot waar de geldigheid van deze benaderingen reikt. Een periodieke ordening van deeltjes leidt tot diffractie-orders die afhangen van de afstand tussen

de deeltjes, de frequentie en hoek van inval van het inkomende licht. Een belangrijke omstandigheid is die waar diffractie-orders verstrooien in het vlak van het rooster. De frequentie waarbij dit gebeurt, wordt de Rayleigh anomaly (RA) voorwaarde genoemd. Licht dat wordt verstrooid in het vlak van het rooster versterkt de koppeling tussen de verschillende verstrooiers door middel van straling en kan leiden tot scherpe resonanties die bekend zijn als oppervlakte rooster resonanties (Surface Lattice Resonances, SLRs). Vervolgens wordt het elektromagnetische spectrum bij terahertz frequenties geïntroduceerd, dat veelzijdig is in toepassingen en rijk aan fysica. De optische eigenschappen van gedoteerde halfgeleiders bij deze frequenties worden beschreven en er wordt ingegaan op de relatie tussen halfgeleiders en plasmonica. Het hoofdstuk wordt afgesloten met een korte beschrijving van standaard technieken voor het opwekken en waarnemen van terahertz pulsen met een enkele cyclus.

Hoofdstuk 2 introduceert meer in detail de werking van de THz tijd-domein spectrometers die gebruikt zijn voor het verkrijgen van de experimentele resultaten gepresenteerd in dit proefschrift. Er wordt een voorbeeld gegeven van een typisch signaal en bijbehorend spectrum en er wordt uitgelegd hoe de ruwe meetdata wordt verwerkt om tot een uitdovingsspectrum te komen. De tijd-domein signalen van de THz spectrometer kunnen worden gebruikt om de optische eigenschappen van dikke ongedoteerde substraten alsmede de elektronische eigenschappen van dunne lagen van gedoteerde halfgeleiders te bepalen. Dit kan worden gedaan door middel van een analyse die gebaseerd is op de transfer matrix methode. De eigenschappen van de substraten van de samples alsmede de polymeren die gebruikt zijn voor het binden van de dunne halfgeleider lagen zijn bepaald met deze transfer matrix methode. Voor foto-geëxciteerde ladingsdragers in een dunne laag gallium-arsenide is deze methode gebruikt om een theoretische schatting te maken van het effect op de transmissie ten gevolge van ambipolaire diffusie van ladingsdragers.

We tonen experimenteel de resonante uitdoving van terahertz straling van een enkele metallische strikvormige antenne aan in *hoofdstuk 3*, waarbij deze antenne is gevormd door twee n-gedoteerde silicium monomeren met een driehoekige vorm met de punten gericht naar elkaar. Hierin zijn we geslaagd door de antenne te plaatsen bij de uitgang van een kegelvormige golfgeleider, die de intensiteit van het invallende THz veld op de plaats van de antenne versterkt met een factor 10. De golfgeleider onderdrukt ook de achtergrondstraling van de meetopstelling die anders zou zijn doorgelaten zonder te worden verstrooid door de antenne. Strikvormige antennes, die gelokaliseerde resonanties ondersteunen, zijn relevant door hun vermogen om resonant de intensiteit van het elektromagnetische veld te versterken in de opening tussen de twee driehoekige elementen. Deze opening heeft afmetingen die vele malen kleiner zijn dan de golflengte van de terahertz straling en kan ervoor zorgen dat deze wordt geconcentreerd beneden de diffractie-limiet. De combinatie van een strikvormige antenne met een kegelvormige golfgeleider kan dienen als een platform voor verre-veld THz tijd-domein spectroscopie van enkele nanostructuren die geplaatst worden in de opening van de antenne.

In *hoofdstuk 4* onderzoeken we theoretisch de versterkte uitdoving van THz straling door periodiek gerangschikte halfgeleider deeltjes. De gelokaliseerde resonanties van de individuele deeltjes in de verzameling kunnen met elkaar een koppeling aangaan door middel van diffractie, en als gevolg van de periodieke eigenschappen van het rooster leiden tot SLRs. Deze diffractieve koppeling kan worden gemodelleerd met een gekoppeld dipool model dat in dit hoofdstuk wordt geïntroduceerd. De meest eenvoudige periodieke structuur is een 1D ketting van dipolen. Met gallium-arsenide als halfgeleider wordt aangetoond dat deze resonanties worden gekenmerkt door een grote uitdoving en een smalle bandbreedte. De versterkte uitdoving van THz straling in 1D kettingen van gallium-arsenide deeltjes kan worden afgestemd over een groot bereik als functie van de concentratie van ladingsdragers aanwezig in de halfgeleider. Tot slot wordt in dit hoofdstuk het onderliggende mechanisme van diffractieve koppeling dat leidt tot deze afstembaarheid verklaard.

De experimentele analyse van de versterkte uitdoving van THz straling door periodieke roosters van halfgeleider deeltjes wordt gepresenteerd in *hoofdstuk 5*. In dit hoofdstuk onderzoeken we bij THz frequenties SLRs in 2D roosters van vierkante silicium deeltjes die met arsenide zijn gedoteerd, en in foto-gegenereerde roosters in een continue laag van gallium-arsenide. De 2D roosters zijn gekozen in plaats van 1D kettingen vanwege de grotere vulfractie van de deeltjes, die leidt tot een grotere uitdoving in de metingen. Meetresultaten van de silicium roosters worden ondersteund met gekoppelde dipool model berekeningen en simulaties die gebruik maken van de 'eindig verschil in het tijd-domein' (finite difference in the time-domain, FDTD) methode. Numerieke simulaties laten een lokale toename van de intensiteit in het nabije-veld zien van een orde van grootte en een gemiddelde versterking van de intensiteit in de eenheids-cel van een factor 2.5. We tonen het concept aan van actieve controle van SLRs in een continue dunne laag gallium-arsenide door middel van selectieve foto-excitatie. Met behulp van een ruimtelijke licht modulator (Spatial Light Modulator, SLM) wordt een patroon geprojecteerd op de halfgeleider. Vrije ladingsdragers worden alleen aangeslagen daar waar de halfgeleider belicht wordt. Door het patroon van de belichting te veranderen kunnen de optische eigenschappen van de halfgeleider worden gemanipuleerd en gecontroleerd. De experimentele resultaten zijn vergeleken met numerieke simulaties en met elkaar in overeenstemming.

Hoofdstuk 6 bespreekt de uitdovings spectra van een periodieke ketting van dipolen met twee dipolen per eenheids-cel. In zulke periodieke roosters worden twee SLRs aangeslagen door dezelfde RA, één voor elke dipool in de eenheids-cel. De interferentie tussen deze twee SLRs vervormt het collectieve uitdovings spectrum als een functie van de verschuiving van de twee dipolen. In dit hoofdstuk wordt het gekoppelde dipool model zoals eerder gepresenteerd uitgebreid om meerdere dipolen per eenheids-cel te kunnen bevatten. Voor een verschuiving die gelijk is aan de helft van de periode van het rooster kan het karakteristieke transparantie venster rond de RA voorwaarde

worden onderdrukt. Wanneer de dipolen ten opzichte van elkaar worden ontstemd hybridiseren er twee modes, wat resulteert in een extra maximum in de uitdoving van het verre-veld rond een frequentie iets kleiner dan de RA voorwaarde en een opgewekt transparantie venster. De berekeningen zijn vergeleken met numerieke simulaties en er bestaat een bijzonder grote mate van overeenstemming tussen beide. Het opgewekte transparantie venster bestaat zelfs wanneer de verstrooiers worden geplaatst op een interface van lucht en kwarts. Dit opent mogelijkheden voor nabije-veld experimenten en potentiële toepassingen voor sensoren.

Notation

$\mathbf{B}$	magnetic field vector
c	speed of light in vacuum
C_{ext}	extinction cross section
d	particle diameter
e	electron charge
$\mathbf{E}$	electric field vector
f	filling fraction
$G(\mathbf{r})$	dipole-dipole interaction tensor
$I(\nu)$	intensity
$\mathbf{J}$	electric current
k	wavenumber
$\mathbf{k}$	wavevector
k_b	Boltzmann's constant
L	ellipsoid form factor
m_e	effecive electron mass
$\tilde{n}$	complex refractive index
N	charge carrier concentration
n	real refractive index
$\mathbf{p}$	polarization dipole
Q_{ext}	extinction efficiency
$\mathbf{r}$	coordinate vector
r_{AB}	reflection coefficient
S	lattice sum
$\mathbf{T}$	transmittance
$\tilde{t}$	transmission
$\arg(t)$	transmission phase
t_{AB}	transmission coefficient
α	particle polarizability
Γ	lattice constant
Δ	dipole displacement

ϵ	relative permittivity
ϵ_0	vacuum permittivity
θ	angle of incidence
κ	imaginary refractive index
λ	wavelength in vacuum
μ	electron mobility
μ_0	vacuum permeability
ν	frequency
σ	scattering cross section
$\tilde{\sigma}$	complex conductivity
τ	collision time
χ	bulk polarizability
ω	angular frequency
ω_p	plasma frequency
Re(x)	real component of x
Im(x)	imaginary component of x

Matrix elements are defined as

$$\boldsymbol{M} = \begin{bmatrix} M_{11} & M_{12} \\ M_{21} & M_{22} \end{bmatrix}$$

Common used abbreviations

BCB	benzocyclobutene
CDM	coupled dipole model
EO	elecro-optic
FEM	finite element method
FDTD	finite difference in the time-domain
HWHM	half width at half maximum
LR	localized resonance
LSP	localized surface plasmon
MLWA	modified long wavelength approximation
NIR	near infrared
PBC	periodic boundary conditions
PCA	photo-conductive antenna
PEC	perfect electric conductor
PML	perfectly matched layer
RA	Rayleigh anomaly
SLM	spatial light modulator
SLR	surface lattice resonance
SPP	surface plasmon polariton
T-matrix	transfer matrix
THz-TDS	terahertz time-domain spectrometer

List of Publications

This thesis is based on the following publications:

1. *Enhanced terahertz extinction of single plasmonic antennas with conically tapered waveguides*, M.C. Schaafsma, H. Starmans, A. Berrier and J. Gómez Rivas, New J. Phys. **15**, 015006 1-14 (2013). (invited) **(Chapter 3)**

2. *Semiconductor plasmonic crystals: active control of THz extinction*, M.C. Schaafsma and J. Gómez Rivas, Semicond. Sci. Technol. **28**, 124003 1-7 (2013). (invited) **(Chapter 4)**

3. *Control of THz resonances in arrays of semiconductor antennas*, M.C. Schaafsma, G. Georgiou and J. Gómez Rivas. (in preparation) **(Chapter 5)**

4. *Surface lattice resonances in photo-generated GaAs structures*, M.C. Schaafsma, G. Georgiou and J. Gómez Rivas. (in preparation) **(Chapter 5)**

5. *Transparency windows in periodic arrays of detuned and displaced dipoles*, M.C. Schaafsma, G. Ramanandan, A. Bhattacharya and J. Gómez Rivas. (in preparation) **(Chapter 6)**

Other publications by the author:

1. *Selective detection of bacterial layers with terahertz plasmonic antennas*, A. Berrier, M.C. Schaafsma, G. Nonglaton, J. Bergquist and J. Gómez Rivas, Biomed. Opt. Express **3**, 2937-2949 (2012).

2. *Collective resonances in plasmonic crystals: Size matters*, S.R.K. Rodriguez*, M.C. Schaafsma*, A. Berrier and J. Gómez Rivas, Phys. B: Condensed Matter, **407**, 4081 (2012).

3. *Universal scaling of the figure of merit of plasmonic sensors*, P. Offermans, M.C. Schaafsma, S.R.K. Rodriguez, Y. Zhang, M. Crego-Calama, S. Brongersma and J. Gómez Rivas, ACS Nano **5**, 5151-5157 (2011).

4. *Active terahertz beam steering by photo-generated graded index gratings in thin semiconductor films*, T.P. Steinbusch, H.K. Tyagi, M.C. Schaafsma, G. Georgiou and J. Gómez Rivas, Opt. Express **22**, 26559-26571 (2014)

5. *Active loaded plasmonic antennas at THz frequencies: Optical control of their capacitive - inductive coupling*, G. Georgiou, C. Tserkezis, M.C. Schaafsma, J. Aizpurua and J. Gómez Rivas (submitted)

6. *All-electronic Terahertz Spectrometer for Deep Subwavelength Layer Detection*, A. Berrier, L. Tripodi, H. Schäfer-Eberwein, M.C. Schaafsma, M.K. Matters-Kammerer, P. Haring Bolivar and J. Gómez Rivas (submitted)

* Equal contribution

Acknowledgements

Writing the acknowledgements is one of the rewarding parts of writing this thesis. It makes me realize once more the number of people that have been involved in the process of doing research, one way or the other. While most of the work in science is still individual, on key points you depend on -or get inspired by- people that leave their mark on the final result. At the risk of forgetting to mention people, I name a few that stand out.

A special thanks goes to my first promotor Jaime Gómez Rivas. Jaime, I learned a lot from you over the past years and I am proud to have you as my promotor. You pushed me to my limits, and made sure I made the most out of myself. The past years which I spent in your group are ones that I will remember. The opportunities you provided me inspired me more than I anticipated, both at AMOLF and Philips Research. Aside from being an example as a determined physicist, I admire how you manage to always put your priorities there where it matters the most.

I had the pleasure to be part of the Surface Photonics group. You guys made the past years extra worth the while. Audrey Berrier, Said Rahimzadeh, Grzegorz Grzela, Gabriel Lozano, Giorgos Georgiou, Rik Starmans, Arkabrata Bhattacharya, Gopika Ramanandan, Tommy Barten, Alexei Halpin, Tom Steinbusch, Giuseppe Pirruccio, Silke Diedenhofen, Hemant Tyagi, Mark Aarts, Mohammad Ramezani, Shunsuke Murai, Yannik Fontana, Yichen Zhang, Christophe Arnold, it was fun working alongside all of you. Audrey: it was under your supervision that I started as an intern in the Surface Photonics group. Thank you for introducing me into the wondrous world of THz plasmonics. Said: you never fail to inspire me and I wish you the best in your career, and thank you for your friendship. It was fun having you as my neighbor in Eindhoven. Grzegorz: my cheerful officemate at the High Tech Campus, those were good times! You can run but you cannot hide, it seems that after a short break we will be colleagues again at ASML, which I look forward to. Gabriel: playing tennis with you was always a good lesson in modesty, and I cherish the one time that I actually won. Giorgos: collaborating with you has been an unforgettable experience. From your experimental skills I learned a lot, and I

have to admit that your lab is the most organized lab I have set a foot into so far. I wish you all the best in becoming a great scientist. Rik: The project we worked on culminated in what is presented in chapter 3 of this thesis, and I enjoyed being your supervisor.

For the time I spent at the High Tech Campus embedded within Philips research I want to thank Hans van Sprang. The collaborations I had on industry-oriented projects were an eye-opener. I think you gave a good example of how research on a fundamental level and industrial research can co-exist. In this respect I also want to mention Lorenzo Tripodi and Marion Matters for the collaboration on the THz-related projects. I enjoyed my time at Philips, and I want to thank all the members of the Photonic Materials and Devices group. A special mention goes to Eugene Timmering, Hans Kwinten, Dominique Bruls, Hans Cillessen, Pauline Deuning and Jurgen Rüsch, thank you all for your support and advise.

For proper experimental results one needs samples of good quality. Audrey Berrier and Hans Kwinten fabricated the Si samples which I used for chapters 2, 3 and 5. The GaAs sample that I used for the experimental results of chapter 5 was fabricated by our collaborators from Nijmegen: Peter Mulder, Gerard Bauhuis and John Schermer. Thank you all for the excellent work!

Within AMOLF I was part of the Center for Nanophotonics. I am realizing more and more the privilege it has been to work in such an inspiring environment, alongside a lot of motivated and bright physicists. You managed to help me solve a great deal of my problems by asking the right questions. From the feedback during poster sessions and colloquia to borrels and coffee-breaks, I always enjoyed spending my time in Amsterdam at the Science Park. My office-mates Abbas Mohtashami and Felipe Bernal: it was a privilege to share the office with you guys. Thank you for the relaxing atmosphere, and sustaining my incidental grumpy moments. Abbas, I enjoyed our discussions about anything but science. Felipe, your enthusiasm is very contagious which is a joy for everyone. A special mention goes to the AMOLF technical support. The quality of the services you provide is outstanding. Whether you need a piece of equipment that doesn't seem to exist, require dedicated software for your experimental setup, a fancy drawing for a publication, and many more: there is someone around to help you get things done. Thanks to the skill and expertise of Jan Versluis, Niels Commandeur, Hinco Schoenmaker, Luc Blom and many others; working in the lab was always something to look forward to. Keep up the good work! Sabine Penning, thank you for your assistance with the distribution of this thesis. To my house-mates at the Middenweg Noreen Walker, Karolina Skraskova, Andras Kiss and Roeland van Wijk: It was fun sharing the apartment with you.

In life it is important to balance work and leisure, and music is one of my more rewarding distractions. I have the privilege to play the violin in Eindhoven's finest Symphony Orchestra. Making music helps me putting things in perspective, and I

always enjoy the Thursday-evening rehearsals. I regret my absence in the past two years, but I am looking forward to make that up in the future. As a person in general, but a scientist in particular, I thrive on challenging myself through solving puzzles and asking questions. In this context I want to mention two teachers: Nico Alink and Jos Paus. Your contribution to my curiosity is something I am very grateful for. Teachers like you, that are an example to their students by showing that science is fun in the first place, are of infinite value.

In the process of preparing the manuscript of this thesis several people provided their feedback. I want to thank Paul Koenraad for being my second promotor, and the members of my doctoral committee. Cornelis de Jong, Pieter de Groot, Giorgos Georgiou: Thank you for your input and assistance in getting the manuscript in its final shape. Rietje Roex, thank you for your advise on the Dutch translation of the summary. Dirk-Jan Spaanderman drew figures 1.6, 1.7, 2.1, 2.3, 4.2 and 5.9. Anouk de Hoogh assisted in figure 3.2. The cover is co-designed by Ruud Mons, thank you for the excellent work. Pieter de Groot and Pieter van Ommeren, it is a pleasure to have you as my paranimfen.

To my family: your unconditional love and support is something that I cherish deeply.

Martijn Schaafsma
Eindhoven, March 2015

About the author

Martijn Cornelis Schaafsma was born on November the 10^{th} 1983 in the Bronovo hospital in The Hague, the Netherlands. After obtaining his high school (VWO) diploma at the Bonhoeffer college in Enschede in 2002 he went on to study applied physics at the Delft University of Technology. During his time in Delft Martijn was an active member of the student association "C.S.R.". He also sat on several committees and in 2005-2006 he sat on the board as treasurer on a full scholarschip. In 2004 he participated with a team of 3 fellow students in PION, a Dutch national Olympiad for Bachelor students in Physics, and won first place. He obtained his Master's degree in 2010. His Master's research project, during which he numerically studied the behavior of vortexes in finite arrays of Josephson junctions, was carried out in the Theoretical Physics group of prof.dr.ir. Gerrit Bauer and was supervised by dr. Jos Thijssen. A four-month internship, as part of his Master's degree, was carried out under the supervision of dr. Audrey Berrier in the research group of prof.dr. Jaime Gómez Rivas. This internship turned out to be the prelude to the project that started in November of 2010. The results of this project are presented in this thesis. Aside from his interests in science, mathematics and his research Martijn has a passion for music. He enjoys listening to classical music, preferably during a live performance. Martijn is an amateur violin player, he has had lessons since he was nine years old. Finally, Martijn also enjoys the occasional long distance walk.